Etude de l'influence de la concentration et de la température sur le temps de relaxation de spin de donneurs immergés dans un puits quantique de CdTe

Guadalupe Garcia-Arellano

Sorbonne Université

Ecole doctorale 564 : Physique en Île-de-France

Thèse de DOCTORAT

Spécialité Physique

Présentée par

Guadalupe GARCIA-ARELLANO

Pour obtenir le grade de docteur de Sorbonne Université

Titre de la thèse

Etude de l'influence de la concentration et de la température sur le temps de relaxation de spin de donneurs immergés dans un puit quantique de CdTe.

Présentée et soutenue publiquement le 29 novembre 2019.

Devant le jury composé de :

Rapporteur	Pierre GILLIOT	Institut de Physique et de Chimie des Matériaux de Strasbourg
Rapportrice	Masha VLADIMIROVA	Laboratoire Charles-Coulomb
Examinatrice	Emmanuelle DELEPORTE	Laboratoire Aimé-Cotton
Examinateur	Gabriel HETET	Laboratoire Pierre-Aigrain
Directrice de thèse	Maria CHAMARRO	Institut des Nanosciences de Paris
Co-encadrant	Frederick BERNARDOT	Institut des Nanosciences de Paris

Acknowledgments

First of all, I want to thank my supervisors Maria Chamarro, Frederick Bernardot and Christophe Testelin for their support and guidance along the PhD.

I would like to highly acknowledge Mathieu Bernard, Maxime Vabre, Florent Margaillan and Francis Breton, engineers at INSP, who respectively assisted me in the maintenance of the cryostat, laser and development of electronic programs. I also thank Loïc Becerra and Erwan Dandeu, managers of the clean room, for the collaboration.

I also want to thank my parents Maria Luisa y Jose Luis, brothers Anmi and Jose Luis, and sister Rosalia, for unfailing support and encouragement throughout my life, and to my friends: Yuvia, Tere, Jackie, Manuel, Juan, Gerardo and Pedro for becoming my Mexican family in Paris.

Finally, I want to thank the Doctoral School 564 *Physique en Île-de-France* and Sorbonne University for the doctoral contract awarded.

.

Abstract

We study the spin relaxation time of donor-bound electrons immersed in the middle of a CdTe quantum well (QW). By inserting the donors in a QW we increase the localization of the electron wave-function. In addition, the optical selection rules for circularly polarized light are purified, allowing a higher degree of optical orientation of the electron spins than in 3D crystals.

The photo-induced Faraday rotation technique is used to measure the spin relaxation time of donor-bound electrons for different doping concentrations at low temperature in the insulating regime. In order to evaluate the spin relaxation mechanisms in our system, we calculate the exchange energy of a pair of donor-bound electrons immersed in the middle of an infinite QW, for any inter-donor distance and for different thicknesses. Then, we explain the experimental behavior as an interplay of two mechanisms: hyperfine and anisotropic exchange interactions, and we determine the CdTe spin-orbit constant: α_{so} = 0.079.

We also develop an extended pump-probe experiment allowing to measure spin relaxation times at the microsecond scale. We briefly discuss the first experimental results for the spin relaxation time of donor-bound electrons as a function of the longitudinal magnetic field and the doping concentration.

Finally, we investigate the temperature evolution of the spin relaxation in the range 10-80 K. The experimental behavior is explained by invoking spin exchange between electron spins localized on donors and the spin of electrons promoted to conduction states. While the spin of localized electrons undergoes the effect of hyperfine and anisotropic exchange interactions, the D'yakonov-Perel' mechanism governs the spin relaxation of the conduction electrons.

Résumé

Nous étudions le temps de relaxation de spin d'électrons liés à des donneurs immergés au milieu d'un puits quantique (PQ) de CdTe. En insérant les donneurs dans un PQ, nous augmentons la localisation de la fonction d'onde électronique. De plus, les règles de sélection optique en lumière circulairement polarisée sont purifiées, ce qui permet d'obtenir un degré d'orientation optique plus élevé que dans les cristaux 3D.

La rotation Faraday photo-induite est utilisée pour mesurer le temps de relaxation de spin d'électrons liés aux donneurs pour différentes concentrations de dopaje, à basse température et dans le régime isolant. Afin d'évaluer les mécanismes de relaxation de spin dans notre système, on calcule l'énergie d'échange d'une paire d'électrons liés à des donneurs immergés au milieu d'un PQ infini, pour toute distance inter-donneur et différentes épaisseurs de PQ. Ensuite, on explique le comportement expérimental à l'aide de deux mécanismes: l'interaction d'échange anisotrope et l'interaction hyperfine, et on détermine la constante spin-orbite de CdTe: α_{so}= 0.079.

Nous développons également une expérience pompe-sonde étendue, permettant de mesurer des temps de relaxation de spin à l'échelle de la microseconde. On discute brièvement des premiers résultats expérimentaux sur le temps de relaxation de spin d'électrons liés aux donneurs en présence d'un champ magnétique longitudinal et pour différents dopages.

Enfin, nous étudions l'évolution de la relaxation de spin dans la plage de température de 10 à 80 K. On explique le comportement expérimental en invoquant l'échange de spin entre les spins d'électrons localisés sur des donneurs et le spin d'électrons promus dans des états de conduction. Alors que le spin des électrons localisés subit l'effet des interactions d'échange anisotrope et hyperfine, le mécanisme de D'yakonov-Perel' régit la relaxation de spin des électrons de conduction.

Contents

Chapter 3: Electron exchange energy for neutral donors inside a quantum well

Chapter 4: Doping influence on the spin relaxation time of electron bound to donors in semiconductor quantum wells

Chapter 5: Temperature dependence of the spin relaxation time of donor-bound electrons in a CdTe QW

Chapter 6

Longitudinal spin relaxation time of donor-bound electrons immersed in a CdTe QW.

Introduction

The original idea of a quantum computer was introduced by Feynman in 1959 [1]. A quantum computer would have a calculation capacity far superior to all current computers, thanks to the storage and to the manipulation of quantum bits ("qubits"). A qubit (or quantum bit) is the quantum mechanical analogue of a classical bit. In classical computing the information is encoded in bits, where each bit can have the value zero or one. In quantum computing the information would be encoded in a qubit: a two level quantum mechanical system. Numerous efforts, both theoretical and experimental, have been made to physically identify qubit candidates. Solid-state qubits are a subset of qubits which present the advantage of scalability due to the use of nanofabrication technologies, but which also present challenges to obtain a suitable protection against interactions with their environment. Nowadays, the two main qubit technologies concern superconductor and semiconductor materials.

In superconducting circuits obtained with nanotechnologies similar to those of the microelectronics, qubits based on phase, charge of flux states have reached a spectacular degree of quantum control [2,3]. One of the main requirements for qubits is to show long coherence times, and then in solid-state physics these qubits have to be protected against environmental interactions. In this sense, the spin of the low-energy electronic states in semiconductors is, in principle, an observable well protected from the environment, and constitutes a good prototype of a qubit. Moreover, to suppress the relaxation mechanism of itinerant electrons (D'yakonov-Perel' process [4]), the electron spin should be localized at a nanometer scale. The confinement can be obtained by nanofabrication as in quantum dots [5–8], or in a more natural way using the attractive potential of individual impurities [9–13].

Indeed, quantum dots are an ideal system for single spin qubits. Spin control in single quantum dots has been recently demonstrated using ultrafast optical pulses by J.

Berezovsky *et al*. [14] and D. Press *et al*. [15]. Nevertheless, they present many technical challenges, as the requirement of low-signal-detection techniques to perform measurements, or their random spatial location. In addition, ensembles of quantum dots have demonstrated large inhomogeneous effects due to the distribution of quantum dot sizes that results from the growth process. Electrons trapped by individual donors in semiconductors, on the contrary, have quasi-atomic electron wave functions, leading to much better homogeneity than electrons confined within self-assembled quantum dots.

In this framework, a large number of experimental studies have been centered on impurities in semiconductors. Phosphorus donors in silicon have recently showed long spin lifetimes [16,17], but because of an indirect band gap, these impurities cannot be optically addressed. In contrast, the direct-band-gap semiconductors exhibit efficient optical transitions. One of the most studied direct-band-gap semiconductors is GaAs. In 1977, C. Weisbuch reported experimental studies on spin relaxation of electrons localized on donors or acceptors [18]. He showed up spin relaxation times up to 30 ns in lightly doped *n*-type crystals of GaAs. Subsequent measurements made by J. M. Kikkawa and D. D. Awschalom [19] reported times around 130 ns at $n_d = 2 \times 10^{16}$ cm^{-3}. All these results motivated intensive research on the influence of doping on spin relaxation times. In bulk GaAs, a complete study of the doping concentration influence on the relaxation time of localized electrons was performed by R. I. Dzhioev *et al*. [20], and recently revisited by J. G. Lonnemann *et al.* [21] and V. V. Behlyk *et al*. [22].

The influence of the doping concentration on the spin relaxation time has been studied, at low temperature, in other zinc-blende bulk materials such as InSb [23], InAs [24], and ZnSe [25], and also in wurzite materials as ZnO [26] and GaN [27,28], for different doping values in the insulating regime and beyond the metal-insulator transition. Recently, a study in the insulating regime was performed in bulk CdTe by D. Sprinzl *et al*. [29].

From the theoretical point of view, in the insulating regime and at low temperature, in bulk GaAs it has been shown that the spin relaxation time is strongly related to the distance between two electrons localized on donors. Different mechanisms contribute to the spin relaxation: at very low concentration of donors, the coupling of an isolated electron spin with the surrounding nuclear spins is the dominant interaction; and at donor concentration near the metallic transition, the exchange interaction is the main mechanism of the spin-spin interaction between neighboring donors [20,30,31]. In the metallic regime, the spin relaxation is dominated by the D'yakonov-Perel' mechanism [4] or the Elliot-Yafet mechanism [32].

In this thesis we are interested in studying the influence of doping concentration, temperature and longitudinal magnetic field on the spin relaxation time of electrons bound to donors immersed in the middle of a CdTe quantum well (QW). We have chosen CdTe for this research because it has the same crystal structure and nearly the same energy band gap as GaAs, but rather different material parameters (e.g. effective masses, dielectric constant, and spin-orbit interaction). In addition, it has been experimentally

demonstrated that, when donors are immersed in a QW, the spin relaxation time of electrons localized on donors is enhanced by two orders of magnitude with respect to the one of free electrons in QWs [33]. Moreover, by inserting the donors in a QW, the optical selection rules for circularly polarized light are purified, allowing a higher degree of optical orientation of the electron spins than in 3D crystals.

The manuscript is organized as follows:

- In the first chapter, we introduce the basic concepts used in this work; then are presented the electronic properties of a doped CdTe QW, its band structure, and the useful optical selection rules. We also describe the spin initialization mechanism, and introduce the optical Bloch equations describing the spin dynamics under a transversal or a longitudinal magnetic field.

- In the second chapter, we describe the two experimental set-ups employed in this work. One uses a pump-probe Faraday technique, and the other a Kerr rotation technique, with a homodyne and a heterodyne detection, respectively.

- In the third chapter, we calculate the exchange energy of a pair of donor-bound electrons placed in the middle of an infinite QW, for any inter-donor distance and for different QW thicknesses. We calculate first the asymptotic form of the exchange energy, adapting to a QW the method developed in Refs. [34,35]. Inspired by the interpolation procedure proposed by I. V. Ponomarev *et al*. [36], we calculate the exchange energy of a "helium atom" inside an infinite QW. Finally, we obtained the values of the exchange energy valid for any interdonor distance and for any QW thickness. We discuss also the behavior of the exchange energy in different III-V and II-VI materials.

- In the fourth chapter, we present measurements of the transversal spin relaxation time (T_2) in our samples, for different doping concentrations spanning from the insulating regime to beyond the metal-insulator transition. By using the calculations developed in chapter 3, we explain the experimental behavior as an interplay of different mechanisms: hyperfine interaction and anisotropic exchange interaction. From the fit of the experimental results, we determine the spin-orbit constant of CdTe.

- In chapter 5, the temperature evolution of the spin relaxation time is exposed, in the range of temperature 10-80 K and for different doping concentrations. We identify the spin relaxation mechanisms undergone by the conduction electrons, and show that the interaction between the spins on localized electrons and conduction electrons explains the experimental data.

- In chapter 6, we present the new development of an extended pump-probe experiment, in order to measure spin relaxation times at the microsecond scale. We briefly discuss the first experimental results, at low temperature, for the longitudinal spin relaxation time (T_1) of donor-bound electrons immersed in a CdTe QW with different doping concentrations, as a function of a longitudinal magnetic field.

References

[1] “There's Plenty of Room at the Bottom” at an annual meeting of the American Physical Society at Caltech, December 1959.
[2] J. Clarke and F. K. Wilhelm, Nature (London) **453**, 1031 (2008).
[3] M. H. Devoret and R. J. Schoelkopf, Science **339**, 1169 (2013).
[4] M. I. D'yakonov and V. I. Perel', Zh. Eksp. Teor. Fiz. **65**, 362 (1973) [Sov. Phys. JETP **38**, 177 (1974)].
[5] R. Hanson and D. D. Awschalom, Nature (London) **453**, 1043 (2008).
[6] J. J. L. Morton and B. W. Lovet, Annu Rev. Condens. Matter, Phys. **2**, 189 (2011).
[7] D. Loss and D. P. DiVincenzo, Phys. Rev. A **57**, 120 (1998).
[8] G. Buckard, D. Loss, and D. P. DiVincenzo, Phys. Rev. B **59**, 2070 (1999).
[9] B. E. Kane, Nature (London) **393**, 133 (1998).
[10] P. M. Koenraad and M. E. Flatté, Nat. Mater. **10**, 91 (2011).
[11] F. Jelezko and J. Wrachtrup, Phys. Status Solidi A **203**, 3207 (2006).
[12] M. W. Doherty, N. B. Manson, P. Delaney, F. Jelezko, J. Wrachtrup, and L. C. L. Hollenberg, Phys. Rep. **528**, 1 (2013).
[13] W. F. Koehl, B. B. Buckley, F. J. Heremans, G. Calusine, and D. D. Awschalom, Nature (London) **479**, 84 (2011).
[14] J. Berezovsky, M. H. Mikkelsen, N. G. Stoltz, L. A. Coldren, D. D. Awschalom, Science **320**, 349 (2008).
[15] D. Press, T. D. Ladd, B. Zhang and Y. Yamamoto, Nature **456**, 218 (2008)
[16] A. M. Tyryshkin, S. A. Lyon, A. V. Astashkin, and A. M. Raitsimring, Phys. Rev. B **68**, 193207 (2003).
[17] J. J. Pla, K. Y. Tan, J. P. Dehollain, W. H. Lim, J. J. L. Morton, D. N. Jamieson, A. S. Dzurak and A. Morello, Nature **489**, 541 (2012).
[18] C. Weisbuch, Ph.D. thesis, Paris-VII University, 1977.
[19] J. M. Kikkawa and D. D. Awschalom, Phys. Rev. Lett. **80**, 4313(1998).
[20] R. I. Dzhioev, K. V. Kavokin, V. L. Korenev, M. V. Lazarev, B. Ya. Meltser, M. N. Stepanova, B. P. Zakharchenya, D. Gammon, and D. S. Katzer, Phys. Rev. B **66**, 245204 (2002).
[21] J. G. Lonnemann, E. P. Rugeramigabo, M. Oestreich, and J. Hübner, Phys. Rev. B **96**, 045201 (2017).
[22] V. V. Belykh, K. V. Kavokin, D. R. Yakovlev, and M. Bayer, Phys. Rev. B **96**, 241201(R) (2017).
[23] D. Guzun, E. A. DeCuir Jr., Vas. P. Kunets, Yu. I. Mazur, G. J. Salamo, S. Q. Murphy, P. A. R. Dilhani Jayathilaka, T. D. Mishima, and M. B. Santos, Appl. Phys. Lett. **95**, 241903 (2009).
[24] B. N. Murdin *et al.*, Phys. Rev. B **72**, 085346 (2005).
[25] A. Greilich, A. Pawlis, F. Liu, O.A. Yugov, D. R. Yakovlev, K. Lischka, Y. Yamamoto, and M. Bayer, Phys. Rev. B **85**, 121303(R) (2012).
[26] S. Ghosh, V. Sih, W. H. Lau, D. D. Awschalom, S.-Y. Bae, S. Wang, S. Vaidya, and G. Chapline, Appl. Phys. Lett. **86**, 232507 (2005).
[27] B. Beschoten, E. Johnston-Halperin, D. K. Young, M. Poggio, J. E. Grimaldi, S. Keller, S. P. DenBaars, U. K. Mishra, E. L. Hu, and D. D. Awschalom, Phys. Rev. B **63**, 121202(R) (2001).
[28] J. H. Buss, J. Rudolph, S. Shvarkov, H. Hardtdegen, A. D. Wiek, and D. Hagele, Appl. Phys. Lett. **102**, 192102 (2013).

[29] D. Sprinzl, P. Horodyská, N. Tesarová, E. Rozkotová, E. Belas, R. Grill, P. Malý, and P. Nemec, Phys. Rev. B **82**, 153201 (2010).
[30] K. V. Kavokin, Phys. Rev. B **64**, 075305 (2001).
[31] K. V. Kavokin, Semicond. Sci. Technol. **23**, 114009 (2008).
[32] R. J. Elliott, Phys. Rev. **96**, 266 (1954); Y. Yafet, *Solid State Physics* **14**, 1 (1963).
[33] J. Tribollet, E. Aubry, G. Karczewski, B. Sermage, F. Bernardot, C. Testelin, and M. Chamarro, Phys. Rev. B **75**, 205304 (2007).
[34] L. P. Gor'kov and L. P. Pitaevskii, Dokl. Akad. Nauk SSSR **151**, 822 (1963) [Sov. Phys. Doklady **8**, 788 (1964)].
[35] C. Herring and M. Flicker, Phys. Rev. **134**, A362 (1964).
[36] I. V. Ponomarev, V. V. Flambaum, and A. L. Efros, Phys. Rev. B **60**, 5485 (1999).
[37] I. V. Ponomarev, V. V. Flambaum, and A. L. Efros, Phys. Rev. B **60**, 15848 (1999).

Chapter 1

Electronic properties of a donor-doped CdTe quantum well

Content

1.1 Introduction

In this chapter, we first give an introduction to the electronic structure of direct-gap zinc-blende materials, bulk and quantum wells. We then present the principles of the optical orientation of a donor-bound electron spin, and the characterization of the loss of spin orientation.

1.2 Electronic structure of zinc-blende semiconductors

1.2.1 Bulk materials: $\vec{k}.\vec{p}$ method

In a bulk semiconductor material, the crystal lattice is seen by an electron as a periodic potential. This periodicity is at the origin of the band structure of the electronic spectrum. The energy band structure is obtained solving the Schrödinger equation [1]:

$$H\Psi_{n,\vec{k}}(\vec{r}) = \left(\frac{\vec{p}^2}{2m_0} + V_c(\vec{r})\right)\Psi_{n,\vec{k}}(\vec{r}) = E_{n,\vec{k}}\Psi_{n,\vec{k}}(\vec{r})\,, \tag{1.1}$$

where m_0 is the electron mass, n is the index that indicates the band, $\vec{k}$ is the quasi wave-vector that represents the quantum translational number, $\vec{p} = -i\hbar\vec{\nabla}$, V_c is the periodic potential due to the crystal lattice, and $\Psi_{n,\vec{k}}(\vec{r})$ is the electron wavefunction that is written, according to the Bloch theorem, as:

$$\Psi_{n,\vec{k}}(\vec{r}) = \exp\left(i\vec{k}.\vec{r}\right)u_{n,\vec{k}}(\vec{r})\,, \tag{1.2}$$

with $u_{n,\vec{k}}(\vec{r})$ a periodic function on the crystal, that contains the information about the crystal structure. The function $u_{n,\vec{k}}(\vec{r})$ satisfies the equation

$$(H_0 + H')\,u_{n,\vec{k}}(\vec{r}) = E_{n,\vec{k}}\,u_{n,\vec{k}}(\vec{r})\,, \tag{1.3}$$

where $H_0 = \frac{\vec{p}^2}{2m_0} + V_c(\vec{r})$ and $H' = \frac{\hbar\vec{k}.\vec{p}}{m_0} + \frac{\hbar^2\vec{k}^2}{2m_0}$. When $\vec{k} = 0$, $H' = 0$ and $\Psi_{n,\vec{0}}(\vec{r}) = u_{n,\vec{0}}(\vec{r})$. The functions $u_{n,\vec{0}}(\vec{r})$ are determined using the group theory. Since H_0 does not take the spin into account, the functions are doubly degenerated.

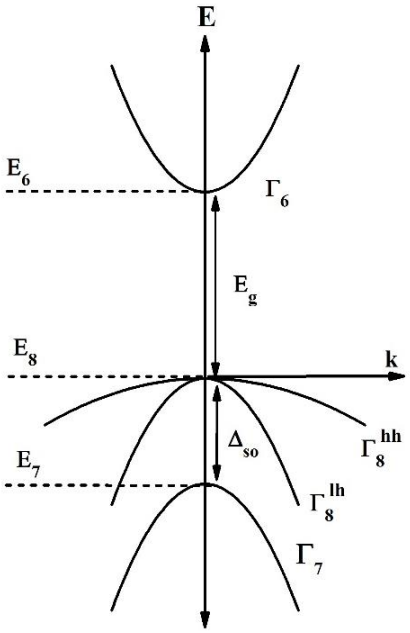

Figure 1.1 *Band structure of a zinc-blende semiconductor around* $\vec{k} = 0$.

To obtain the band structure when $\vec{k} \neq 0$, it is needed to find the eigen-functions and eigen-values of equation (1.3) with the complete Hamiltonian $H_0 + H'$. In direct-band-gap zinc-blende semiconductors, the description of the optical properties requires the electronic states around $\vec{k} = 0$. The $\vec{k}.\vec{p}$ method consists in treating the H' term as a perturbation, taking as a basis for the eigen-functions $u_{n,\vec{k}}$ the set of functions $u_{n,\vec{0}}$:

$$u_{n,\vec{k}} = \sum_m c_m(\vec{k}) u_{m,0} \,. \tag{1.4}$$

Thus, considering eigen-functions approximated to first order in $\vec{k}$, and eigen-energies to second order, one obtains

$$E_{n,\vec{k}} = E_{n,\vec{0}} + \frac{\hbar^2 \vec{k}^2}{2m_0} + \frac{\hbar^2}{m_0^2} \sum_{i \neq n} \frac{\left| \left\langle u_{n,\vec{0}} \middle| \overrightarrow{k.p} \middle| u_{i,\vec{0}} \right\rangle \right|^2}{E_{n,\vec{0}} - E_{i,\vec{0}}}, \tag{1.5}$$

$$u_{n,\vec{k}} = u_{n,\vec{0}} + \frac{\hbar}{m_0} \sum_{i \neq n} \frac{\left\langle u_{n,\vec{0}} \middle| \overrightarrow{k.p} \middle| u_{i,\vec{0}} \right\rangle}{E_{n,\vec{0}} - E_{i,\vec{0}}} u_{i,\vec{0}} \,. \tag{1.6}$$

To simplify the writing, we introduce the electron effective mass m_n^* such that:

$$E_{n,\vec{k}} = E_{n,0} + \frac{\hbar^2 \vec{k}^2}{2m_n^*}, \tag{1.7}$$

where m_n^* is the effective mass of the edge of band n. The different effective masses lead to different curvatures in the energy band diagram.

Band	Energies (at $\vec{k}=0$)	Notation $\|J,J_z\rangle$	Eigen-functions (at $\vec{k}=0$)
Γ_6	$+E_g$	$\left\|\frac{1}{2},\frac{1}{2}\right\rangle$	$u_{1,0}=\|S,\uparrow\rangle$
		$\left\|\frac{1}{2},-\frac{1}{2}\right\rangle$	$u_{2,0}=\|S,\downarrow\rangle$
Γ_8^{hh}	0	$\left\|\frac{3}{2},\frac{3}{2}\right\rangle$	$u_{5,0}=\frac{1}{\sqrt{2}}\|X+iY,\uparrow\rangle$
		$\left\|\frac{3}{2},-\frac{3}{2}\right\rangle$	$u_{6,0}=\frac{1}{\sqrt{2}}\|X-iY,\downarrow\rangle$
Γ_8^{lh}	0	$\left\|\frac{3}{2},\frac{1}{2}\right\rangle$	$u_{3,0}=\frac{1}{\sqrt{6}}\|X+iY,\downarrow\rangle-\sqrt{2/3}\|Z,\uparrow\rangle$
		$\left\|\frac{3}{2},-\frac{1}{2}\right\rangle$	$u_{4,0}=\frac{1}{\sqrt{6}}\|X-iY,\uparrow\rangle+\sqrt{2/3}\|Z,\downarrow\rangle$
Γ_7	$-\Delta_{SO}$	$\left\|\frac{1}{2},\frac{1}{2}\right\rangle$	$u_{7,0}=\frac{1}{\sqrt{3}}[\|X+iY,\downarrow\rangle+\|Z,\uparrow\rangle]$
		$\left\|\frac{1}{2},-\frac{1}{2}\right\rangle$	$u_{8,0}=\frac{1}{\sqrt{3}}[\|X-iY,\downarrow\rangle-\|Z,\uparrow\rangle]$

Table 1.1 *Bloch functions at $\vec{k}=0$ for the valence bands Γ_7 and Γ_8, and the conduction band Γ_6 of a zinc-blende semiconductor.*

Taking into account the spin-orbit interaction, a new term has to be introduced in the Hamiltonian H of eq. (1.1):

$$H_{so}=\frac{1}{2m_0^2c^2}\left(\vec{S}\times\vec{\nabla}V\right).\vec{p}\,, \tag{1.8}$$

with $\vec{S}=\frac{\hbar}{2}\vec{\sigma}$ the electronic spin operator ($\sigma_x,\sigma_y,\sigma_z$: Pauli matrices). Then H does not commute with $\vec{S}$, but it commutes with the total angular momentum:

$$\vec{J}=\vec{L}+\vec{S}. \tag{1.9}$$

The spin-orbit coupling let invariant the conduction states for which the orbital moment is zero, while for the valence band states, the degeneracy is lifted: the states with $J=1/2$ (Γ_7 band) are shifted to lower energies as compared to the ($J=\frac{3}{2}$) ones (Γ_8 band). A representation of the band structure is given in Fig. 1.1, and the eigenfunctions are given in Table 1.1. The energy splitting between the Γ_6 and Γ_8 bands, at $\vec{k}=0$, is the band gap E_g of the semiconductor; the one between the Γ_8 and Γ_7 is the spin-orbit energy Δ_{SO}. The spin-orbit coupling also gives different effective masses of the states in the heavy-hole band ($\Gamma_8, J_z=\pm 3/2$) and in the light-hole band ($\Gamma_8, J_z=\pm 1/2$).

1.2.2 Energy states in a quantum well: Envelope function method

To calculate the electronic states in a quantum well (QW), it is common to use the method of the envelope function. In this method, an electronic wavefunction in a QW (with the confinement along the z axis) is written as

$$\Psi_{n,\vec{k}_{\parallel}}(\vec{r}) = \Phi(z)\exp\left(i\vec{k}_{\parallel}.\vec{r}_{\parallel}\right)u_{n,\vec{k}_{\parallel}}(\vec{r}),$$

where $\Phi(z)$ is an envelope function that satisfies the eigenvalue equation:

$$\left(-\frac{\hbar^2}{2m_n}\frac{d^2}{dz^2}+V_{QW}\right)\phi(z)=\varepsilon\phi(z), \tag{1.10}$$

with V_{QW} the confinement potential of the QW, due to the different band gaps of the materials, and $u_{n,\vec{k}_{\parallel}}(\vec{r})$ the Bloch function; the factor $\exp(i\vec{k}_{\parallel}.\vec{r}_{\parallel})$ reveals the free motion in the plane x-y parallel to the QW. In Eq. (1.10), the effective mass m_n^* is different inside the QW ($0<z<L$) and outside (in the barriers), with L the width of the QW. The confinement energy ε is an additional contribution to the eigen-energy associated to $\Psi_{n,\vec{k}_{\parallel}}(\vec{r})$.

For degenerate bands, such as the Γ_8 band of Fig. 1.1, the calculations are more complicated and are not presented here. In the limit of the infinite confinement potential, with $V_{QW}(0<z<L)=0$, we find

$$\phi(z)=\sqrt{\frac{2}{L}}\sin(n_z\pi\frac{z}{L}) \tag{1.11}$$

and

$$\varepsilon=\frac{\hbar^2\pi^2}{2m_n^*L^2}n_z^2, \tag{1.12}$$

with $n_z=1,2,3\ldots.$; m_n^* is the effective mass in the QW. From this simple model of confinement, we keep two pieces of information, also valid in general: (i) when n_z is odd (even), $\phi(z)$ is symmetric (antisymmetric) with respect to the $z=L/2$ plane; (ii) ε is inversely proportional to the effective mass. Point (ii) has an immediate consequence: there is a lifting, by the energy Δ_{lh}, of the degeneracy of the energies of heavy and light-holes bands, since the effective mass of the heavy-hole band is greater than the effective mass of the light-hole band. The band structure of a zinc-blende QW is shown in Fig.1.2.

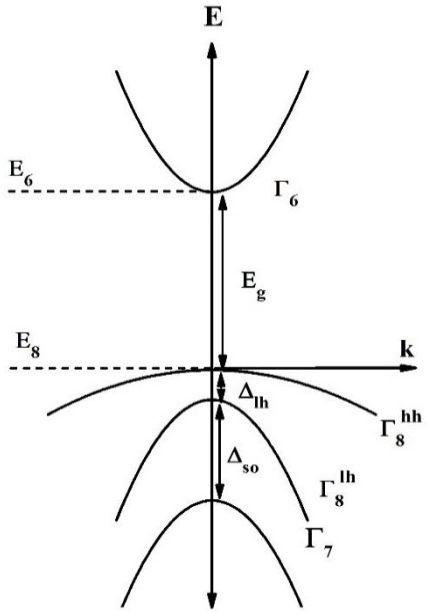

Figure 1.2 *Band structure of a zinc-blende QW. The heavy-hole band Γ_8^{hh} ($J_z = \pm 3/2$) and the light-hole one Γ_8^{lh} ($J_z = \pm 1/2$) are split (by energy Δ_{lh}). The gap (of energy E_g) is between the Γ_6 and Γ_8^{hh} band edges.*

1.3 Optical selection rules

We consider in this section the effect of a laser beam propagating along the confinement axis z of a QW. According to the Fermi golden rule, the probability per unit time that an electron makes a transition from the state $|\Psi_i\rangle$ to the state $|\Psi_f\rangle$ in presence of an optical field with vector potential $\vec{A} = A_0\hat{\varepsilon}e^{i(kz-\omega t)} + A_0^*\hat{\varepsilon}^*e^{-i(kz-\omega t)}$ ($A_0 = iE_0/2\omega$), is

$$\tilde{P}_{if} = \frac{2\pi}{\hbar}\left|\langle\Psi_f|\hat{H}_1|\Psi_i\rangle\right|^2\delta\left[\varepsilon_f - \varepsilon_i - \hbar\omega\right], \tag{1.13}$$

where $\hat{H}_1$ is the Hamiltonian representing the coupling of the electron with the optical field:

$$\hat{H}_1 = \frac{e}{m_e}\vec{p}.\vec{A}(\vec{r}) + \frac{e^2A^2(\vec{r})}{2m_e}, \tag{1.14}$$

and ε_i and ε_f are the eigenenergies of the states $|\Psi_i\rangle$ and $|\Psi_f\rangle$, respectively. The quadratic term in the expression (1.14) is generally considered small compared to the linear one; this term plays a role only for very high intensities of the order of $10^{15}\ W/\text{cm}^2$ which may be observed for very intense and tightly focused pulsed femtosecond lasers [3]. Here, only the linear term in $\vec{A}$ is considered in Eq. (1.14). In addition, under typical experimental conditions, the optical wavelength $\lambda = 2\pi/k$ is much larger than the QW width, so the spatial dependence of $\vec{A}$ can be neglected: $\lambda \to \infty$, $k \to 0$ so $e^{ikz} \approx 1$. This is known as the electric dipole approximation:

$$\hat{H}_1 \approx \hat{H}_{dip} = \frac{eE(t)}{m_0\omega}\hat{\varepsilon}.\vec{p}, \tag{1.15}$$

with $E(t) = E_0 sin(\omega t)$. In the case that the states $|\Psi_i\rangle$ and $|\Psi_f\rangle$ are partially or completely occupied, it is needed to take into account the impossibility of allowing transitions from either an empty level or towards a filled one. Thus, the probability per unit time that an electron makes a $|\Psi_i\rangle \rightarrow |\Psi_f\rangle$ transition is equal to

$$P_{if} = \tilde{P}_{if} f(\varepsilon_i)\big[1 - f(\varepsilon_f)\big], \tag{1.16}$$

where $f(\varepsilon_v)$ is the mean occupancy of a state $|\Psi_v\rangle$, $f(\varepsilon_v) = \{1 + \exp[\beta(\varepsilon_v - \mu)]\}^{-1}$ with $\beta = (k_B T)^{-1}$, T the temperature and μ the chemical potential of the electrons.

Summing over all states, one obtains the net energy loss per unit time of the electromagnetic wave when it enters into the material, which is also the power absorbed from the field by the sample:

$$P(\omega) = \frac{2\pi}{\hbar}\frac{q^2 E_0^2}{m_0^2 \omega^2}\hbar\omega \sum_{i,f} \delta\big[\varepsilon_f - \varepsilon_i - \hbar\omega\big]\big|\langle\Psi_f|\hat{\varepsilon}.\vec{p}|\Psi_i\rangle\big|^2 \big[f(\varepsilon_i) - f\big(\varepsilon_f\big)\big]. \tag{1.17}$$

A specific transition $|\Psi_i\rangle \rightarrow |\Psi_f\rangle$ is dominant when the optical frequency is $\omega = (\varepsilon_i - \varepsilon_f)/\hbar$. In our case we tune the optical frequency near the energy gap: $\omega \approx E_g/\hbar$. The matrix element $\langle\Psi_f|\hat{\varepsilon}.\vec{p}|\Psi_i\rangle$ governs the optical selection rules of the material. This term is calculated using the wavefunctions for an electron in a QW described in section 1.2.2, taking the expression

$$\langle\Psi_f|\hat{\varepsilon}.\vec{p}|\Psi_i\rangle = \langle u_f|\hat{\varepsilon}.\vec{p}|u_i\rangle\langle\Phi_f|\Phi_i\rangle \tag{1.18}$$

for interband transitions. In this work, we are interested in the optical transitions between the $\Gamma_8^{hh}(J_z = \pm 3/2)$ and Γ_6 $(J_z = \pm 1/2)$ bands of a QW (see Fig. 1.2).

The integral $\langle\Phi_f|\Phi_i\rangle = \int_\Omega \Phi_f^*(\vec{r})\,\Phi_i(\vec{r})d^3r$ in Eq. (1.18) dictates the allowed subband indices for a transition, while the matrix element $\langle u_f|\hat{\varepsilon}.\vec{p}|u_i\rangle$ governs the optical selection rules for the polarization of the light. For a type-I symmetrical QW, the envelope functions have a defined parity with respect to the center plane of the QW (cf. 1.2.2); thus the integral $\int_\Omega \Phi_f^*(\vec{r})\,\Phi_i(\vec{r})d^3r$ is non-zero only if the initial and final envelope functions have the same parity. Thus only the transitions $S_v \leftrightarrow S_c$, $P_v \leftrightarrow P_c$ are allowed, as shown in Fig. 1.3.

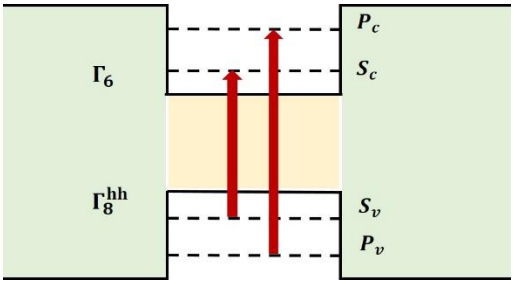

Figure 1.3 *Inter-band optical transitions allowed in a quantum well.*

The factor $\langle u_i|\hat{\varepsilon}.\vec{p}|u_f\rangle$ being evaluated for circularly polarized light, $\sigma+$ or $\sigma-$, one obtains that this kind of polarization induces transitions with $\Delta J_z = +1$ or $\Delta J_z = -1$; these transitions are shown in Fig. 1.4. Because of the light-hole/heavy-hole splitting, only transitions between the Γ_8^{hh} and Γ_6 band edges are possible. In comparison with bulk materials (where the heavy-hole and light-hole bands are degenerated), the level scheme of the valence band in a QW purifies the optical selection rules: the light-hole states do not come into play.

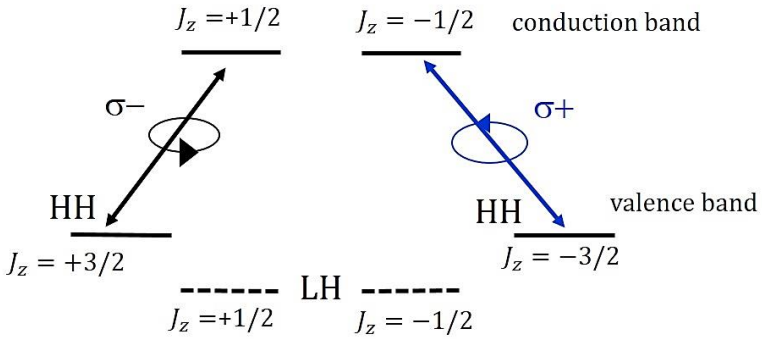

Figure 1.4 *Optical selection rules for a circularly polarized beam propagating along the confinement axis of a QW, and whose energy is resonant at the energy gap. Only $\Delta J_z = +1$ or $\Delta J_z = -1$ transitions are possible between the Γ_8^{hh} and Γ_6 bands, operated by $\sigma+$ or $\sigma-$ optical polarizations, respectively.*

1.4 Excitons, donors and donor-bound excitons

1.4.1 Excitons

When an electron is promoted to the conduction band, the missing electron in the ensemble of full valence states is considered as a particle called hole. The system that results due to the Coulomb interaction between the conduction electron and the hole is called exciton (X). This hydrogen-like bound system is characterized by a Bohr radius and a binding energy that are obtained by replacing in the hydrogen atom formulas the electron mass m_0 and the vacuum permittivity ϵ_0, by the reduced mass μ^* of the electron-hole pair and by the product $\epsilon_0\epsilon_r$, with ϵ_r the dielectric constant of the material:

$$\mu^* = \frac{m_e^* m_h^*}{m_e^* + m_h^*} \tag{1.19}$$

$$E_X^{*3D} = \frac{\mu}{2\epsilon_r^2} E_h \tag{1.20}$$

$$a_X^{*3D} = \frac{\epsilon_r}{\mu} a_0, \tag{1.21}$$

with $\mu = \mu^*/m_0$, $a_0 = \frac{4\pi\epsilon_0\hbar^2}{m_e e^2} \approx 0.52918$ Å, $E_h = \frac{e^2}{4\pi\epsilon_0 a_0} \approx 27.211$ eV the Bohr radius and Hartree energy of the atomic units, and m_e^* (m_h^*) the effective electron (hole) mass.

For bulk CdTe, equations (1.20) and (1.21) give $a_X^{*3D} = 5.66$ nm and $E_X^{*3D} = 12.4$ meV considering the values $m_e^* = 0.11\, m_0$[3], $m_{hh}^* = 0.72\, m_0$ [4] and $\epsilon_r = 10.2$ [5].

In QWs, the confinement affects the binding energy of the exciton. The calculation of the confined exciton energy is generally accomplished by applying the variational principle [6].

1.4.2 Donors

An atom with one electron more than it is necessary to form the covalent bonds with neighboring atoms being introduced into a lattice, it is called a donor impurity. For II-VI semiconductors like CdTe, an atom of tellurium with six valence band electrons is replaced by an atom with seven valence band electrons, like iodine, to introduce a donor impurity.

The binding energy E_B^{*3D} and Bohr radius a_B^{*3D} of a donor-bound electron in a bulk material can be calculated by replacing the electron mass m_0 and the vacuum permittivity ϵ_0 by the electron effective mass m_e^* and the product of $\epsilon_0\epsilon_r$, respectively, in the hydrogen atom formulas:

$$E_B^{*3D} = \frac{m_e^*}{m_0\epsilon_r^2}\frac{E_h}{2}, \tag{1.22}$$

$$a_B^{*3D} = \frac{m_0}{m_e^*}a_0\epsilon_r. \tag{1.23}$$

For CdTe we obtain: $E_B^{*3D} = 14.4$ meV and $a_B^{*3D} = 4.91$ nm.

The binding energy of an electron bound to a donor in a CdTe QW has been calculated in Ref. [7]. The procedure is presented here below.

The Hamiltonian describing a donor-bound electron inside a QW of thickness L writes

$$H(z) = -\frac{\hbar^2}{2m_e^*}\Delta - \frac{e^2}{4\pi\varepsilon_0\varepsilon_r}\frac{1}{r} + V(z)\,, \tag{1.24}$$

where $V(z)$ is the QW confinement potential defined by $V(z) = 0$ for $|z| \leq L/2$ and $V(z) = V_0$ for $|z| > L/2$, Δ is the Laplacian operator and r the distance of the electron to the origin of the coordinates (where the impurity is located). The electron binding energy $E_B(L)$ and the Bohr radius $a_B(L)$ are determined by means of the variational method. The trial wave-function is taken in the following form:

$$\Psi(\vec{r}) = \chi(z)e^{-\frac{\sqrt{\rho^2+\alpha^2 z^2}}{a_B}}\,, \tag{1.25}$$

where $\chi(z)$ is an envelope function, and a_B and α are the variational parameters.

The equation associated to the envelope wavefunction in the QW:

$$H_z\chi(z) = E_0\chi(z), \tag{1.26}$$

is solved with $H_z = -\frac{\hbar^2}{2m}\frac{d^2}{dz^2} + V(z)$ and E_0 the QW lowest energy confinement. Then the mean energy $\langle\Psi|H|\Psi\rangle$ is minimized to obtain the binding energy defined by $E_B = E_0 - \langle\Psi|H|\Psi\rangle$ and the effective Bohr radius a_B, for a given QW of thickness L.

Figure 1.5 (a) shows the L-dependence of the parameters α and a_B, for a barrier height $V_0 = 125$ meV. For a CdMgTe/CdTe/CdMgTe QW, this corresponds to a conduction band offset of 70 % and a barrier Mg concentration of 11 %. At large QW width, the 3D limit is reached, with $\alpha = 1$ and $a_B = a_B^{*3D} = 4.91$ nm. When L decreases both parameters decrease, then increase when L crosses a value close to the 3D Bohr radius. It is well known that for a finite barrier, when the QW width decreases, the wavefunction starts to get more confined, before spreading in the barrier for L smaller than the 3D Bohr radius. The α and a_B behaviors are the signature of this effect, as can be seen for L < 5 nm in Fig. 1.5(a).

Using the equation (1.25) for the wavefunction, the coefficient $\langle k_z^2\rangle = \left\langle\Psi\left|\left(-i\frac{d}{dz}\right)^2\right|\Psi\right\rangle$ is also calculated (which will be useful in chapter 4). Figure 1.5(b) shows this coefficient $\langle k_z^2\rangle$ and the binding energy E_B versus the QW width L. Starting from the bulk binding energy, for large L values, one observes a maximum binding energy $E_B \approx 2E_B^{*3D}$ for $L \approx a_B^{*3D}$.

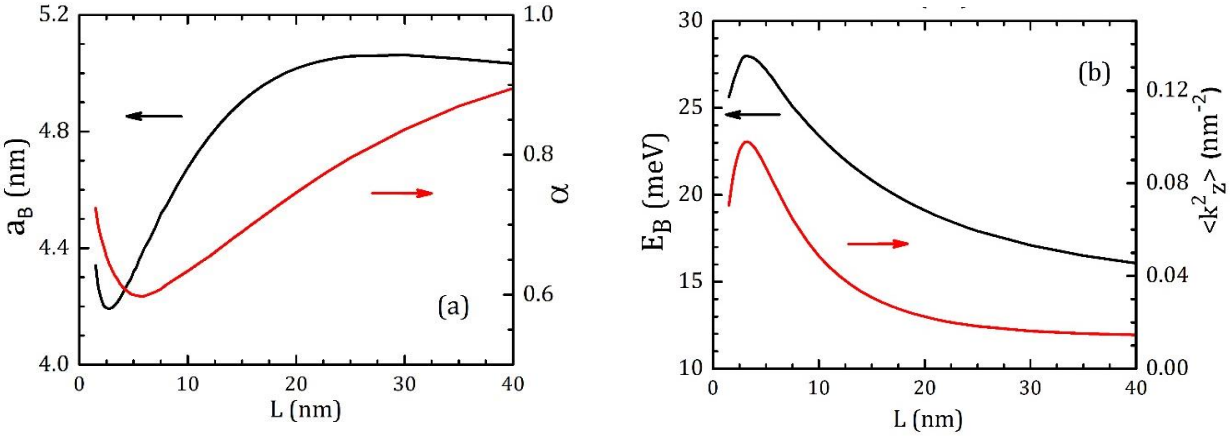

Figure 1.5 *(a) Bohr radius a_B (left axis) and parameter α (right axis) of an electron bound to a donor in the middle of a CdTe QW of thickness L (barrier height: $V_0 = 125$ meV). (b) Binding energy E_B (left axis) and $\langle k_z^2\rangle$ (right axis) for different thicknesses L of this QW.*

1.4.3 Donor-bound excitons

A neutral donor impurity can serve as an attractive potential for carriers in a semiconductor lattice through the van der Waals interaction. Excitons can be attracted to these impurities and form a complex known as a donor-bound exciton (D^0X). D^0X is composed of a positive nucleus, two electrons (one photo-created and the other associated to the donor) in the lowest energy state of zero spin, and a hole (see Fig. 1.6). As a consequence, the spin of a D^0X complex is the spin of the photo-created hole.

The binding energy of a D^0X complex is defined as the energy required to remove the exciton from the impurity.

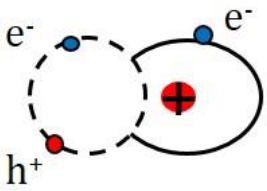

Figure 1.6 *Schematic diagram of a donor-bound exciton.*

1.5 Spin initialization of a donor-bound electron

The spin polarization of donors (difference of populations of resident electrons with spins up and down) can be built via the optical orientation of D^0X complexes. Figure 1.7 gives a diagram of the different optical transitions and relaxation times involved in the formation and evolution of a D^0X complex in a QW. In this method of polarization of donors, a $\sigma^+(\sigma^-)$ circularly-polarized pump pulse photo-creates D^0X complexes with $+3/2$ $(-3/2)$ holes, from spin up (down) electrons bound to donors. The corresponding localized D^0X complexes are denoted $D^0X_{+3/2}$ $(D^0X_{-3/2})$ in the diagram. Immediately after the pump pulse, the sample contains more donor-bound electrons with spin down (up) than with up (down) electrons, and also $D^0X_{+3/2}$ $(D^0X_{-3/2})$ complexes.

If the condition $T_h \ll T_R$ is satisfied, with T_h the spin relaxation time of holes and T_R the recombination time of D^0X complexes, then the populations of $D^0X_{+3/2}$ and $D^0X_{-3/2}$ balance before recombination. After the D^0X recombination, the number of resident electrons with spin down (up) has then been increased, to the detriment of the spin up (down) ones. In brief, $\sigma^+(\sigma^-)$ pulses create a spin-down (spin up) polarization of donors. The D^0 spin polarization relaxes with the T_1 characteristic time.

In a CdTe QW of width L = 8 nm, with a residual concentration of donors, the recombination time T_R has been measured to be $T_R = 175$ ps [8]. Measuring the decay rate $1/\tau$ of the difference between the D^0X spin populations, the relaxation time of the hole spin has been extracted $(1/\tau = 1/T_h + 1/T_R)$: T_h= 83 ps.

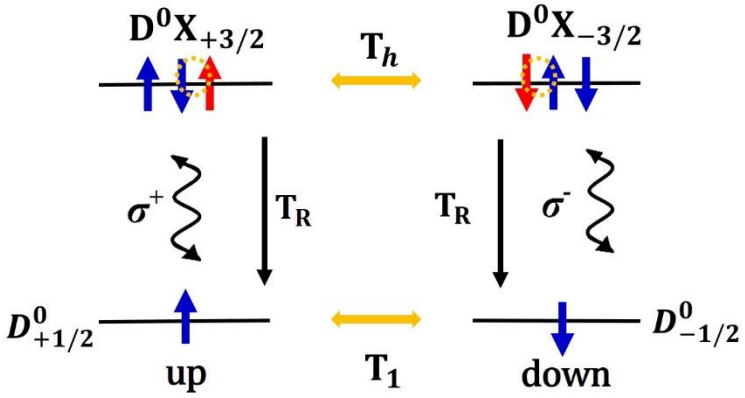

Figure 1.7 *Diagram of the different optical transitions and relaxation times involved in the formation and evolution of a D^0X complex in absence of a magnetic field. State $D^0_{\pm 1/2}$ is coupled to the $D^0X_{\pm 3/2}$ state by a $\sigma \pm$ optical transition. T_R: recombination time; T_1 and T_h: spin relaxation times of the D^0 and D^0X states, respectively.*

1.6 Spin dynamics

In this section, we present the equations that we will use (cf. chapter 4) to describe the evolution of the D^0 electron spin polarization under the application of a transverse or longitudinal magnetic field, with respect to the growth direction of the QW.

1.6.1 Transverse magnetic field

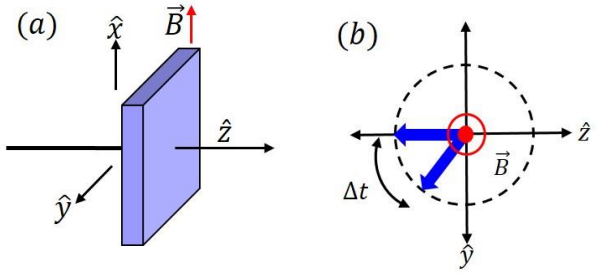

Figure 1.8 *(a) Definition of axes relative to sample growth direction and magnetic field direction (Voigt configuration: $\vec{B} \perp \vec{k}$, $\vec{k} \parallel \hat{z}$). (b) Precession of the spin polarization in the z-y plane.*

A transverse magnetic field $\vec{B}$ induces a precession of the D^0 spin polarization in the z-y plane (see Fig. 1.8). The equation that describes the evolution of the spin polarization in a QW with a magnetic field applied in the Voigt configuration is

$$\frac{d\vec{S}_\perp}{dt} = \vec{\Omega}_e \times \vec{S}_\perp - \frac{\vec{S}_\perp}{T_2^*} + \frac{J(t)}{T_R}\hat{z}, \tag{1.27}$$

where $\vec{S}_\perp$ is the component of the spin polarization in the z-y plane, $\vec{\Omega}_e = \Omega_e \vec{e}_x$ is the Larmor precession frequency of the ensemble of electrons, and T_2^* is (classically interpreted) the characteristic time that the ensemble of electrons takes to lose their

phase; T_2^* is dominated by the inhomogeneity of the electron Landé $g_e^\perp$ factors in the sample (which lead to different precession frequencies). T_2^* is usually called spin dephasing time. The source term J/T_R of eq. (1.27) involves the D^0X complexes recombining with rate $1/T_R$ and producing donor-bound electrons aligned with the $\hat{z}$ axis; $J(t) = J_0 e^{-t/\tau}$ with $1/\tau$ the D^0X spin relaxation rate.

The solution of eq. (1.27) (up to a proportionality constant), for times larger than the recombination time T_R, writes:

$$S_z(t) = e^{-\frac{t}{T_2^*}} \cos(\Omega_e t). \tag{1.28}$$

For a single electron bound to donor in a transverse magnetic field of magnitude B, we have:

$$s_0(t) = e^{-\frac{t}{T_2}} \cos(\frac{g_e^\perp \mu_B B}{\hbar} t), \tag{1.29}$$

where $g_e^\perp$ is the electron Landé factor, μ_B is the Bohr magneton, and T_2 the spin decoherence time. Thus, for an ensemble of electron spins:

$$S(t) = \int dg_e^\perp \, \mathcal{D}(g_e^\perp) \, s_0(t), \tag{1.30}$$

where $\mathcal{D}(g_e^\perp)$ is the distribution of the electron Landé factors. Assuming a Lorentzian distribution with mean value $\bar{g}_e^\perp$ and half-width at half-maximum $\Delta g_e^\perp$:

$$\mathcal{D}(g_e) = \frac{1}{\Delta g_e^\perp \pi} \frac{1}{1+\left(\frac{g_e^\perp - \bar{g}_e^\perp}{\Delta g_e}\right)^2}, \tag{1.31}$$

we get, substituting (1.31) in (1.30):

$$S(t) = e^{-\frac{t}{T_2}} e^{-\frac{\Delta g_e^\perp \mu_B B}{\hbar} t} \cos\left(\frac{\bar{g}_e^\perp \mu_B B}{\hbar} t\right). \tag{1.32}$$

Comparing (1.32) with (1.28), we obtain a relation between T_2^* and T_2, and a relation between the Larmor precession frequency and the mean value $\bar{g}_e^\perp$ of the electron Landé factors:

$$\frac{1}{T_2^*} = \frac{1}{T_2} + \frac{\Delta g_e^\perp \mu_B B}{\hbar}, \tag{1.33}$$

$$\Omega_e = \frac{\bar{g}_e^\perp \mu_B B}{\hbar}. \tag{1.34}$$

Under the described conditions, Eq. (1.33) shows that $1/T_2^*$ depends linearly on the magnetic field. In chapter 4, we will measure the spin dephasing time T_2^* at different magnetic fields; using eq. (1.33), we will find by extrapolation to zero magnetic field, the spin relaxation time of a single electron T_2.

1.6.2 Longitudinal magnetic field

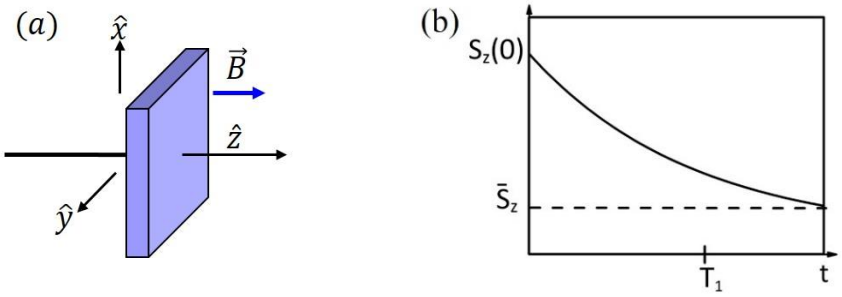

Figure 1.9 *(a) Definition of axes relative to sample growth direction and magnetic field direction (Faraday geometry). (b) Qualitative interpretation of the Bloch equation (1.35). Relaxation of $S_z(t)$ towards the value $\bar{S}_z$ is controlled by T_1.*

The Bloch equation that describes the dynamics of the spin polarization component along the magnetic field is

$$\frac{dS_z}{dt} = \frac{\bar{S}_z - S_z}{T_1}, \tag{1.35}$$

where $\bar{S}_z$ is the equilibrium spin polarization, and T_1 is the characteristic time that the system takes to reach it. The solution of eq. (1.35) is

$$S_z(t) = (C - \bar{S}_z)\exp\left(-\frac{t}{T_1}\right) + \bar{S}_z, \tag{1.36}$$

with C a constant of integration, $C = S_z(0)$.

The relaxation time T_1 is associated to an energy transfer from the spin system (Zeeman energy) to the lattice. Spin-lattice interaction includes all the processes in which energy is exchanged between the spin system and its surroundings. A transfer of energy of the spin system to the lattice is associated with transitions from the upper to the lower spin state, and causes the population number of the two spin states (and therefore the polarization in the z axis) to change.

Under the formalism of the density matrix for a two-level system, T_1 describes the relaxation of a non-equilibrium spin population (diagonal elements of the spin density matrix) towards equilibrium, while $1/T_2$ is the decay rate of the off-diagonal elements of the spin-density matrix. In the appendix A it is shown, using this formalism, that the longitudinal spin relaxation time T_1 is equal to the transversal spin relaxation time T_2 ($T_1 = T_2$) for a vanishing magnetic field. The spin relaxation time, denoted τ_s from now on, will be measured in our samples using an extrapolation to zero magnetic field, see chapters 4 and 5.

1.7 Bibliography of chapter 1

[1] C. Kittel, *Introduction to Solid State Physics,* 8th edition (Springer-Verlag, Berlin Heidelberg, 2009).
[2] G. Bastard, *Wave mechanics applied to semiconductor heterostructures* (Les Editions de Physique, 1988), chapter III.
[3] I. Hernández-Calderón, in II-VI Semiconductor Materials and their Applications, edited by M. C. Tamargo (Taylor and Francis, New York, 2002).
[4] K. A. Jackson, W. Schroter, *Handbook of Semiconductor Technology* (Wiley-VCH Verlag, Germany, 2000).
[5] I. Strzalkowski, S. Joshi, and C. R. Crowell, Appl. Phys. Lett. **28**, 350 (1976).
[6] P. Harrison, *Quantum wells, wires and dots,* 2nd ed. (Wiley, New York, 2005).
[7] G. Garcia-Arellano, F. Bernardot, C. Testelin, and M. Chamarro, Phys. Rev. B **98**, 195308 (2018).
[8] P. Grinberg, F. Bernardot, B. Eble, G. Karczewski, C. Testelin, and M. Chamarro, Journal of Applied Physics **119**, 123906 (2016).
[9] P. Harrison, S. J. Weston, T. Piorek, T. Stirner, W. E. Hagston, J. E. Nicholls, and M. O'Neill, Superlattices Microstruct. **14**, 249 (1993).
[10] J. Tribollet, F. Bernardot, M. Menant, G. Karczewski, C. Testelin, and M. Chamarro Phys. Rev. B **68**, (2003).
[11] K. Blum, *Density Matrix Theory and Applications,* 3rd edition (Springer-Verlag, Berlin, 2012).

Chapter 2

Measure of the photo-induced Faraday-Kerr rotation

Content

2.1 Introduction

One of the oldest methods to measure the spin relaxation time in semiconductors is based on the Hanle effect [1]. The Hanle effect is the decreasing of the degree of circular polarization of the photoluminescence (DCP), when a transverse magnetic field $\vec{B}$ is applied (Voigt configuration). The DCP is defined as $P = (I_{\sigma+} - I_{\sigma-})/(I_{\sigma+} + I_{\sigma-})$, where $I_{\sigma+}(I_{\sigma-})$ is the intensity of the $\sigma + (\sigma -)$ circularly polarized component of the emitted light.

The Hanle effect, first observed by Wood and Ellet in 1924 [3], occurs due to the precession of the optically oriented electronic spins around the magnetic field $\vec{B}$. The plot of the degree of polarization P, as a function of the magnetic field (Hanle curve), follows a Lorentzian curve:

$$P(B) = \frac{P(0)}{1 + (\Omega_e \tau^*)^2}, \tag{2.1}$$

where $P(0)$ is the degree of polarization in absence of magnetic field, $\Omega_e = g_e^{\perp}\mu_B B/\hbar$, the Larmor precession frequency, and τ^* is a time composed of the spin relaxation time τ_s and the recombination time τ_R: $1/\tau^* = 1/\tau_s + 1/\tau_R$. To determine τ_s by this method, it is necessary to know the Landé factor $g_e^{\perp}$ and the recombination time.

A recently developed technique to measure spin relaxation time of donor-bound electrons in semiconductors, is spin noise spectroscopy (SNS) [4,5]. SNS is a technique that extracts the spin information of an ensemble of electrons in a non-perturbative way, mapping the stochastic spin polarization in the ensemble via the Faraday effect. Its experimental realization is straightforward, in its principles: a linearly polarized beam, below the band-gap energy, is transmitted through the investigated sample, which is mounted in a cryostat. A small external magnetic field $\vec{B}$ perpendicular to the beam propagation is used to increase the sensitivity of the method, and makes the stochastic spin polarization to precess. After transmission through the sample, the rotated beam is spectrally analyzed via fast Fourier transform (FFT).

Figure 2.1 shows a typical noise spectrum for an external magnetic field of 30 mT in Voigt geometry, at low temperature. The maximum of the spin noise signal is centered at the Larmor precession frequency Ω_e of the stochastic electron spin polarization. The full width at half maximum Δ_f of the Lorentzian shape gives the spin relaxation time by the relation $\tau_s = (\pi\Delta_f)^{-1}$.

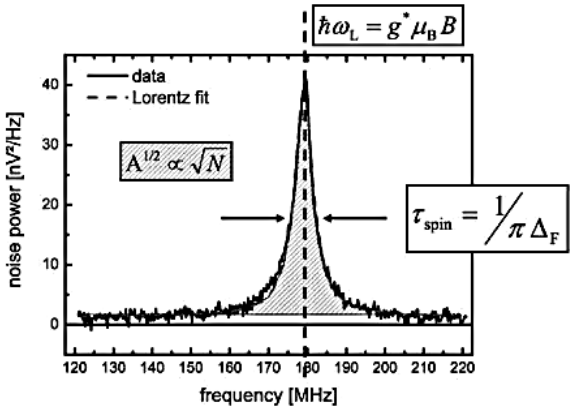

Figure 2.1 *(taken from [4]). A typical spin noise spectrum. The noise power is plotted against the frequency. The studied system is bulk GaAs, at low temperature; B = 30 mT.*

In the 80's, the invention of the ultra-fast lasers allowed significant progresses in the study of relaxation phenomena of photo-excited systems. Many experimental methods based on the use of ultra-short light pulses allowed to reach the needed temporal resolution for the study of the spin dynamics in doped semiconductors. Some of these techniques are: time-resolved photoluminescence (TRPL) and photo-induced Faraday/Kerr rotation (PFR /PKR) techniques.

In the TRPL technique, the spin polarization is detected by measuring the DCP as a function of magnetic field [6]. This technique is one of the most sensitive techniques for the study of the spin dynamics; nevertheless, it only allows an access to the excited states of the studied system: the information obtained is then restricted over a time interval of the order of the lifetime of the observed radiative species. Recently, the TRPL technique has been adapted to measure longer spin relaxation times [7], by including pump and probe pulses for the excitation and collection of light. This adaptation will be described in chapter 6.

The standard PFR and PKR techniques were developed respectively by Awschalom's group in Saint Barbara, and by Harley's group in Southampton [8,9]. In these techniques, an electron spin polarization is created by a circularly polarized pulse (pump pulse), and detected on a linearly polarized pulse (probe pulse), delayed in time, via the Faraday or Kerr effect, respectively. The delay between the arrival of the pump and probe pulses on the sample varies mechanically; therefore the maximum temporal window is given by the largest difference in optical path between the pump and probe beams: ~ 1m gives a temporal range of the order of several ns. Recently, V. V. Behlyk *et al*. [10] developed an extended PFR technique, able to measure spin relaxation times in the microsecond regime, by electronic variation of the pump-probe delay. This technique will be described in Chapter 6.

In this work, we have chosen to use the standard PFR and PKR techniques, since they are well adapted to measure the spin relaxation time in doped semiconductors.

In this chapter, we describe first the principles of the standard PFR and PKR techniques that allow to study the dynamics of an electron spin polarization in the range 10 ps -2 ns. Then we introduce the physical principles of the equipment used for the detection of the photo-induced Faraday/Kerr angle; finally, we present the experimental set-ups.

2.2 Magneto-optic and photo-induced Faraday effect

2.2.1 Magneto-optic Faraday effect

The Faraday effect is a magneto-optic phenomenon in which the linear polarization of a beam is rotated upon propagation in a dielectric medium under a magnetic field applied parallel to the beam [11,12]. The observed rotation of the plane of polarization is due to a circular birefringence of the medium, and is proportional to the intensity of the component of the magnetic field in the direction of the beam of light.

A simple way to understand the Faraday effect is now described. Let us consider a beam linearly polarized along the x axis and propagating in z direction through a material with refractive indices n_+, n_- for left and right polarized light respectively. A linearly polarized beam can be decomposed into the sum of left and right circular polarized components, so the beam propagating in the sample can be written as [12]:

$$\vec{E} = \frac{1}{2}E_0\left(\vec{e}_x + i\vec{e}_y\right)e^{i\left(\frac{2\pi n_+}{\lambda_0}z-\omega t\right)} + \frac{1}{2}E_0\left(\vec{e}_x - i\vec{e}_y\right)e^{i\left(\frac{2\pi n_-}{\lambda_0}z-\omega t\right)}, \tag{2.2}$$

with λ_0 the wavelength in the vacuum. Equation (2.2) can be also written as [12]:

$$\vec{E} = E_0 e^{i\left(\frac{2\pi \bar{n}}{\lambda_0}z-\omega t\right)}\left[\vec{e}_x \cos(\theta_F) + \vec{e}_y \sin(\theta_F)\right], \tag{2.3}$$

which reflects the fact that the polarization of the beam is rotated by an angle θ_F:

$$\theta_F = \pi\left(\frac{n_- - n_+}{\lambda_0}\right)L, \tag{2.4}$$

with L the length of the dielectric medium and $\bar{n} = \frac{n_- + n_+}{2}$.

2.2.2 Photo-induced Faraday effect

a. General description of the experiment

In a PFR experiment, a circular birefringence in the medium is created by a circularly polarized beam (pump beam) that excites the sample. Thus, when a linearly polarized beam traverses the medium after a time Δt, its plane of polarization rotates due to the Faraday effect. Figure 2.2 shows a scheme of the PFR experiment. The *photo-induced* rotation angle θ_F contains the information about the electron spin polarization inscribed by the pump beam. Measuring this angle as a function of the delay between the arrivals of the pump and probe pulses, allows to access to the spin dynamics of the system.

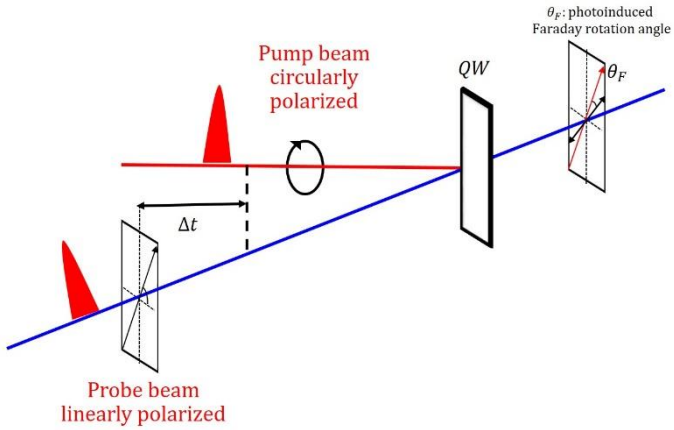

Figure 2.2 *Scheme of a PFR experiment*

In practice, the *photo-induced* Faraday angle θ_F is measured by means of an optical bridge. After interaction with the sample, the probe beam is sent to a polarizing beam splitter which divides the light into two orthogonal polarized components *x* and *y* (see Fig. 2.3) that correspond to the projections of the incident polarization (with intensity I_0) on the axes of the beam splitter. These two components, with intensities I_1 and I_2 respectively, are detected by two photodiodes from which the output signal is the difference I_1- I_2:

$$S(t) = I_1 - I_2 = I_0\left(sin^2\left(\theta_F + \frac{\pi}{4}\right) - cos^2\left(\theta_F + \frac{\pi}{4}\right)\right) = I_0 \sin(2\theta_F) \approx 2I_0\theta_F \quad (2.5)$$

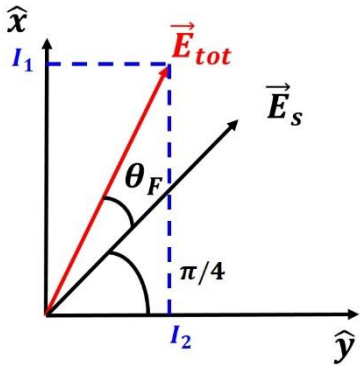

Figure 2.3 *Detection of the photo-induced Faraday angle: $\vec{E}_s$ ($\vec{E}_{tot}$) denotes the electric field of the probe beam before (after) interaction with the sample.*

b. Description of the measured signal

We describe now the signal measured during the PFR experiment, and show it contains the information about the electron spin polarization.

As described in chapter 1, $\sigma^+(\sigma^-)$ circularly polarized pump pulses photo-create D^0X complexes with $+3/2$ $(-3/2)$ holes, from spin up (down) electrons bound to donors. Just after interaction of a pump pulse with a donor, the state of the system can be described by the density matrix ρ in the basis of states $\{|e+\rangle, |e-\rangle, |D^0+\rangle, |D^0-\rangle\}$, where $|e+\rangle, |e-\rangle$ denote the fundamental states of the system (resident electron with spin up or spin down) and $|D^0+\rangle, |D^0-\rangle$ denote the excited states (exciton bound to donor D^0X with the hole spin up or down). Figure 2.4 presents the used scheme of the levels. The temporal evolution of the density matrix under the influence of the probe, is denoted $\sigma(t)$ in the following.

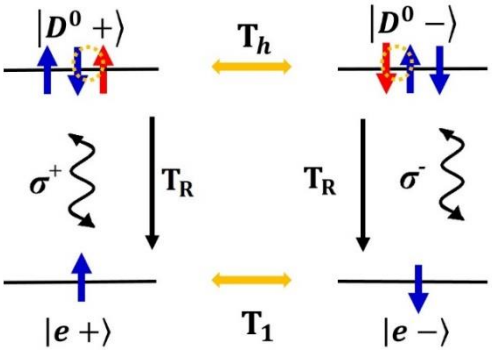

Figure 2.4 *After interaction with a pump pulse, the system is modeled as a 4-level system. State $|e+\rangle$ ($|e-\rangle$) is coupled to the $|D^0+\rangle$ ($|D^0-\rangle$) state through a $\sigma+$ ($\sigma-$) optical transition. T_R: recombination time; $T_1(T_h)$: spin relaxation time of the donor-bound electron (exciton).*

- **Interaction of the system with the probe beam**

The electric field $\vec{E}_s$ of the probe beam (linearly polarized) before interaction with the system can be expressed as

$$\begin{aligned} \vec{E}_s = & \quad \sqrt{2}E_0 n(t)e^{-i\omega t}\vec{e}_x + c.c. \\ = & \quad (E_0\vec{e}_+ + E_0\vec{e}_-)n(t)e^{-i\omega t} + c.c., \end{aligned} \tag{2.6}$$

where $\vec{e}_{+,-} = \frac{\vec{e}_x \pm i\vec{e}_y}{\sqrt{2}}$, $n(t)$ is the temporal envelope of the pulse near $t = 0$ $[n(0) = 1]$, and E_0 is the amplitude of the electric field. The Hamiltonian that describes the interaction of the probe beam with the system is given by

$$\hat{H}_I = -E_+\hat{d}_+ - E_-\hat{d}_- + c.c., \tag{2.7}$$

with $\hat{d}_+$ and $\hat{d}_-$ the dipolar operators $\hat{d}_+ = d|D^0+\rangle\langle e+|$ and $\hat{d}_- = d|D^0-\rangle\langle e-|$. Introducing the Rabi pulsation $\Omega_s = \frac{dE_0}{\hbar}$, $\hat{H}_I$ can be written as

$$\widehat{H}_I = -\hbar\Omega_s n(t) e^{-i\omega t} |D^0 +\rangle\langle e +| - \hbar\Omega_s n(t) e^{-i\omega t} |D^0 -\rangle\langle e -| + c.c. \quad (2.8)$$

The temporal evolution of the system under the interaction with the probe beam is given by the Liouville equation:

$$i\hbar \frac{d\sigma}{dt} = [H_0 + H_I, \sigma(t)\,], \quad (2.9)$$

where $\sigma(t)$ satisfies $\sigma(t=0) = \rho$. The damping processes are neglected during the ps-duration of the probe pulse. We calculate now the evolution of the diagonal terms of the density matrix σ. First we calculate for example σ_{D^0+,D^0+}:

$$\begin{aligned} \dot{\sigma}_{D^0+,D^0+} &= \langle D^0 + |H_I\sigma(t) - \sigma(t)H_I| D^0 +\rangle \\ &= i\Omega_s n(t) e^{-i\omega t}\sigma_{e+,D^0+} - i\Omega_s n(t) e^{-i\omega t}\sigma_{D^0+,e+}, \end{aligned} \quad (2.10)$$

where σ_{e+,D^0+} and $\sigma_{D^0+,e+}$ denote the matrix elements:

$$\begin{aligned} \sigma_{e+,D^0+}(t) &= \langle e + |\sigma(t)| D^0 +\rangle \\ \sigma_{D^0+,e+}(t) &= \langle D^0 + |\sigma(t)| e +\rangle. \end{aligned} \quad (2.11)$$

The solution of this equation, keeping only the first order in E_0 is

$$\sigma_{D^0+,D^0+}(t) = \rho_{D^0+,D^0+} + \left(i\Omega_s \rho_{e+,D^0+} e^{-i\omega t} \int_{-\infty}^{t} n(t')dt' + c.c.\right), \quad (2.12)$$

with $\rho_{D^0+,D^0+} = \langle D^0 + |\rho|\, D^0 +\rangle$ and $\rho_{e+,D^0+} = \langle e + |\rho|\, D^0 +\rangle$. The second term appearing in equation (2.12) represents a correction of the undisturbed population ρ_{D^0+,D^0+}. This term, proportional to Ω_s and to the coherence ρ_{e+,D^0+}, can be neglected, since the non-diagonal terms of the density matrix ρ have rapidly decreased after the pump pulse has crossed the sample.

A similar result is obtained for the other diagonal term of the density matrix σ, confirming that the probe beam weakly modifies the populations of the states of the system.

Now we calculate the evolution of the inter-band terms of the density matrix σ:

$$i\hbar\dot{\sigma}_{D^0+,e+}(t) = \hbar\omega_0\sigma_{D^0+,e+}(t) - \hbar\Omega_s n(t) e^{-i\omega t}\sigma_{e+,e+} + \hbar\Omega_s n(t) e^{-i\omega t}\sigma_{D^0+,D^0+}. \quad (2.13)$$

The integration of this equation, keeping only the first term in Ω_s, yields

$$\sigma_{D^0+,e+}(t) = \rho_{D^0+,e+} e^{-i\omega t} + i\Omega_s[\rho_{e+} - \rho_{D^0+}] e^{-i\omega t} \int_{-\infty}^{t} n(t')dt'. \quad (2.14)$$

Similarly: $$\sigma_{D^0-,e-}(t) = \rho_{D^0-,e-} e^{-i\omega t} + i\Omega_s[\rho_{e-} - \rho_{D^0-}] e^{-i\omega t} \int_{-\infty}^{t} n(t')dt'. \quad (2.15)$$

The first terms in both expressions can be neglected. It then appears that the coherences $\sigma_{D^0\pm,e\pm}(t)$ are proportional to the probe field and to the population changes created by the $\sigma \pm$ components of the pump pulse.

- **Measured signal**

The total transmitted field after the sample is the sum of the incident probe field $\vec{E}_s$ and the field $\vec{E}_R$ radiated by the doped sample [13]:

$$\vec{E}_{tot} = \vec{E}_s + \vec{E}_R.$$

The signal *S* measured during the experiment is

$$S \propto |E_{tot}^{+}|^2 - |E_{tot}^{-}|^2 = |E_s^{+} + E_R^{+}|^2 - |E_s^{+} + E_R^{+}|^2, \tag{2.16}$$

where $E_{tot}^{\pm}$ are the components of the total transmitted field with the $\vec{e}_{\pm}$ polarization. Neglecting the quadratic terms in the $\vec{E}_R$ field, the measured signal can be written as

$$S \propto E_0(Re[E_R^{+}] - Re[E_R^{-}]). \tag{2.17}$$

The field $\vec{E}_R$ is expressed as the sum of the dipolar scatterings of the donor-bound electrons, each defined in terms of the classical dipoles $D_{\pm}(t) = \langle \hat{d}_{\pm}(t) \rangle = Tr[\sigma(t)\hat{d}_{\pm}]$. Using the expressions (2.14) and (2.15) of the pertinent $\sigma(t)$ elements, one obtains

$$E_R^{+} = A[\rho_{e-} - \rho_{D^0-}] + c.c. \tag{2.18}$$

$$E_R^{-} = A[\rho_{e+} - \rho_{D^0+}] + c.c., \tag{2.19}$$

with A a coefficient of proportionality. Thus, the signal experimentally detected can be finally written in a simple form:

$$S \propto \Delta\rho_e - \Delta\rho_{D^0}, \tag{2.20}$$

with $\Delta\rho_e = \rho_{e+} - \rho_{e-}$ and $\Delta\rho_{D^0} = \rho_{D^0+} - \rho_{D^0-}$. The detected signal is proportional to the difference of the spin populations of resident electrons and donor-bound excitons. This signal varies with the pump-probe delay; hence the damping processes of Fig. 2.4 are exhibited.

2.3 Modulation equipment

To experimentally detect the Faraday rotation angle (usually of the order of 1 millidegree), it is needed to optimize the signal-to-noise ratio. For this purpose, it is common to use a modulation technique. This consists in transposing the signal of interest to high frequencies; which eliminates different sources of noise existing at low frequencies. In practice, a synchronous detection is employed to filter the measured signal over a sufficiently narrow spectral band around the modulation frequency [14].

Precisely, we used technique consists in a double modulation technique wherein the pump and probe beams are modulated at a different frequencies f_{pump} and f_{probe}. The modulation in polarization of the pump beam is done with an electro-optic modulator working at a frequency of $f_{pump} = 500$ kHz. The intensity modulation of the probe beam is realized by an acousto-optic modulator working at a frequency of $f_{probe} = 3$ kHz. The

demodulations are made by a double-stage lock-in (Zurich Instrument). We present below the operating principles of each modulator and the demodulation process.

2.3.1 Electro-optic modulator

When a beam, propagating in the z direction, enters into an electro-optics modulator, it is polarized at 45° of the principal axes of a birefringent material with optical indices n_1, n_2. By applying a voltage between two metal plates (distant of e) with an amplified supply, an electric field E_s perpendicular to the direction of propagation of the light is applied to the material, modifying its optical indices as [15]:

$$n_1(E) = n_1 - \frac{r_1 n_1^3 E_s}{2},\ n_2(E) = n_2 - \frac{r_2 n_2^3 E_s}{2}, \tag{2.21}$$

where r_1 and r_2 are Pockels coefficients of the birefringent material. Thus, after traversing the birefringent material of thickness d, the difference of phase between the two propagation modes along the axis is

$$\Delta\varphi(E_s) = [n_1(E_s) - n_2(E_s)]k_0 d = \Delta\varphi_0 - \frac{k_0 d}{2}(r_1 n_1^3 - r_2 n_2^3)E_s, \tag{2.22}$$

where $k_0 = \frac{2\pi}{\lambda_0}$ and $\Delta\varphi_0 = (n_1 - n_2)k_0 d$ is the difference of phase in the absence of electric field. The change in the refractive indices is typically very small; however, if the wave propagates a greater distance than the wavelength, this effect becomes significant. The expression (2.22) can be written in terms of the voltage U applied to generate the electric field $E_s = U/e$:

$$\Delta\varphi(E_s) = \Delta\varphi_0 - \pi\frac{U}{U_\pi}, \tag{2.23}$$

where $U_\pi = \frac{\lambda_0}{r_1 n_1^3 - r_2 n_2^3}\frac{e}{d}$ is the half-wave voltage needed to shift $\Delta\varphi$ by π radians; this corresponds to an additional optical path of $\lambda_0/2$ between the two modes of propagation. If the material is neutral at $U = 0$, a voltage equal to $U = \pm U_\pi/2$ allows to polarize the beam circularly. In our experiment a voltage of 600 mV (before amplification) is needed to obtain a circularly polarized pump beam at λ_0 =770 nm. The voltage supply allows to alternate the polarization of the pump beam between right (σ_+) and left (σ_-) circular polarizations. During this work, the frequency modulation for the pump beam has been chosen $f_{pump} = 500$ kHz, knowing that the higher the σ_+/σ_- modulation frequency of the pump beam, the better the final signal-to-noise ratio.

2.3.2 Photo-elastic modulator

The principle of the operation of a photo-elastic modulator (PEM) is based on the photo-elastic effect, in which a mechanically stressed material exhibits a birefringence proportional to the resulting strain. When a linearly polarized beam at 45° enters into a PEM, the birefringence of the material retards one of its components (the horizontal or vertical one) more than the other. The PEM acts then as a dynamical wave plate. In our experimental set-up, the PEM is adjusted so that, at the working wavelength, one

component is alternately retarded and advanced by $\pi/2$ radians relative to the other, so that the exiting beam is alternately right-hand and left-hand circularly polarized.

2.3.3 Acousto-optic modulator

The probe beam is sent to an acousto-optic modulator. An acousto-optic modulator uses the acousto-optic effect to change the direction of a beam and shift its frequency by means of an acoustic wave [16]. The principle of operation is the following. A piezoelectric transducer is attached to an optical crystal, and an oscillating electrical signal makes the transducer vibrate, which creates an acoustic wave traveling at the speed of sound in the material. This acoustic wave creates a periodical disturbance in the crystal so that it forms a medium with a stratified refractive index. So, when the beam interacts with the acoustic wave it is then diffracted in several orders. In our experimental set-up, the frequency of the acoustic wave is of the order of 100 MHz, and the angle of the first-order diffraction of the order of 1°.

The two functions for which an acousto-optic modulator will be used here, are for intensity modulation and for frequency shifting (heterodyne detection, see 2.5.2). The amount of laser light diffracted to the first-order output beam depends on the amplitude of the acoustic wave; by switching on and off the power level of the acoustic wave source, the intensity of the output beam is chopped. In this way, the probe beam in our experimental set-up is modulated at the frequency $f_{probe} = 3$ kHz. Besides, the intensity of the 1st-order output beam is maximized using the Bragg incidence for the probe beam on the acousto-optic modulator.

The optical frequency of the first-order output beam is shifted by an amount equal to the frequency of the acoustic wave, Ω. If ω is the frequency of the incident beam, the frequency of the first-order beam is up-shifted to $\omega + \Omega$ (in the case that the acoustic wave planes have a component of motion toward the incident light beam; the output frequency is downshifted to $\omega - \Omega$ when the acoustic wave planes have a component of motion away from the incident light beam). This property will be use in the heterodyne set-up.

2.3.4 Synchronous detection: demodulation process

The operating principle and interest of a synchronous detection is explained below. The voltage provided by the optical bridge contains three contributions [17]: the signal S_0 that contains the information about the Faraday rotation angle (modulated at two frequencies $f_1 = f_{pump}$ and $f_2 = f_{probe}$); the signal A coming from the scattering of the pump beam on the sample (modulated at the frequency f_{pump}); and a random noise $N(t)$ coming from multiple sources, such as parasite light or electrical noise:

$$V(t) = S_0 \cos(2\pi f_1 t)\cos(2\pi f_2 t) + A\cos(2\pi f_1 t) + N(t). \qquad (2.24)$$

In the double demodulation process, the signal of interest is recovered in two stages. At the first stage, the output voltage is multiplied by a reference harmonic signal $R_1\cos(2\pi f_1 t)$ at the fast frequency $f_{ref\,1} = f_1 = 500$ kHz:

$$V(t)R_1\cos(2\pi f_1 t) = S_0 R_1\cos(2\pi f_2 t)\cos^2(2\pi f_1 t) + AR_1\cos^2(2\pi f_1 t) + B(t)R_1\cos(2\pi f_1 t). \quad (2.25)$$

This product is averaged during a time τ_I, which is very short with respect to the period $1/f_{probe}$ (to not filter the signal at frequency f_{probe}) but greater than the period $1/f_{pump}$ ($1/f_1 \ll \tau_I \ll 1/f_2$) to reject the noise near the pump frequency which gives $S_1(t)$:

$$S_1(t) = \frac{S_0 R_1}{2}\cos(2\pi f_2 t) + \frac{AR_1}{2}. \quad (2.26)$$

At the second stage of demodulation, the signal $S_1(t)$ coming from the first stage is multiplied by a reference harmonic signal at frequency $f_{ref\,2} = 3$ kHz:

$$S_1(t)R_2\cos(2\pi f_2 t) = \frac{S_0 R_1 R_2}{2}\cos^2(2\pi f_2 t) + \frac{AR_1 R_2}{2}\cos(2\pi f_2 t), \quad (2.27)$$

and the product is averaged during a time τ_2 longer than the period $1/f_{probe}$ ($\tau_2 \gg 1/f_{probe}$) to reject the noise near the probe frequency, to finally obtain:

$$S_2(t) = \frac{S_0 R_1 R_2}{4}. \quad (2.28)$$

Here the signal S_2 coming from the second stage provides, within a constant factor, the voltage S_0 of interest which carries the measurement of the photo-induced Faraday angle.

2.4 Photo-induced Faraday rotation technique using a homodyne detection

The experimental set-up of our PFR experiment is shown in Figure 2.5. The light source is a Ti: Sapphire laser (*Coherent Mira*) optically pumped with a continuous laser *Verdi* (532 nm, 15 W), synchronized to produce a pulse of 2 ps each 13.1 ns. The spectral width is 0.8 meV and the laser is tunable between 690-980 nm.

The principal beam is first spatially filtered with a system designed to correct the divergence of the laser; the beam is focused with a 2-mm focal lens on a pinhole of 50 micrometers of diameter and then collimated by a 40-mm focal lens. This system keeps the diameter of the beam almost constant throughout the optical path, downstream.

Then, a beam splitter (70/30) divides the beam into pump and probe. The pump beam is sent to a delay line that contains a corner reflector positioned parallel to the displacement axis. In order to enlarge the time delay, the reflected parallel beam is sent for a second time to the delay line. At the end of the path, the pump beam has undergone

two round trips; thus for each mm that the reflector moves, a time delay of 13.33 ps is incremented.

As explained in Chapter 1, spin orientation in QWs requires circularly polarized light as excitation. The pump beam is then sent to an electro-optic modulator to be circularly polarized. As presented in section 2.3.1, the polarization of the pump beam is alternated between σ_+ and σ_- at the frequency f_{pump}= 500 kHz, avoiding in this way nuclear spin polarization. Indeed, when the sample is excited with a fixed circular polarization, the electron spins are oriented permanently in the same direction, which orientates nuclear spins due to the hyperfine interaction (see Chapter 4). Thus alternating the spin orientation of the electrons each 2 μs allows to neglect nuclear field effects on the electronic spin relaxation dynamics [18,19]. Meanwhile, the probe beam is sent to an

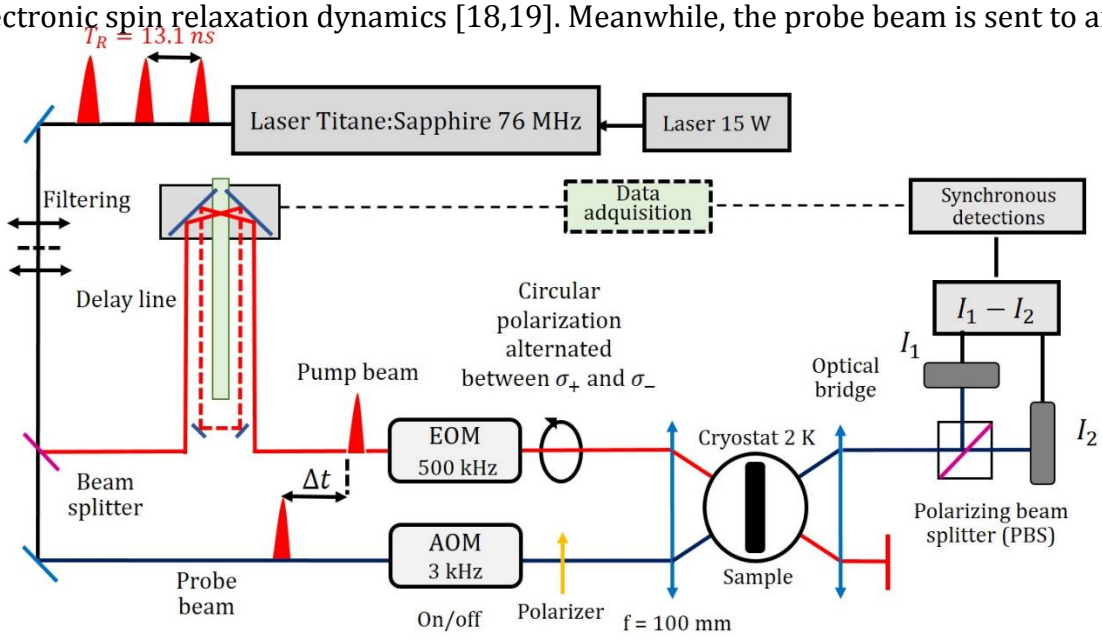

Figure 2.5 *Scheme of the PFR experiment, with homodyne detection*

acousto-optic modulator working at a frequency f_{probe} = 3 kHz, used as an on/off switch. After crossing the acousto-optic modulator, the beam crosses a linear polarizer.

A 100-mm focal lens is used to focus the pump and probe beams on the sample placed in a cryostat. Both beams must arrive parallel to the optical axis in order to ensure that their focal points overlap. The waist diameter d_0 of each beam at the focal plane can be estimated using the relation $d_0 = \frac{2\lambda f}{\pi d}$, where f is the focal length of the lens, d the diameter of the beam at the entrance of the cryostat, and λ the wavelength (around 770 nm for our studies). We estimate d_0 = 30 µm for the pump and 15 µm for the probe beams.

After transmission through the sample, the probe beam is collimated with a 100-mm focal lens, and the pump beam is blocked. The probe beam is then sent to a polarizing beam splitter placed at the entrance of an optical bridge (see section 2.2.2.a). The output

of the bridge is then demodulated by a synchronous detection (see section 2.3.4). A LabVIEW program controls the delay line, and performs the signal acquisition. So the spin dynamics of the sample can be studied as a function of the delay between the pump and probe pulses.

The studied samples are immersed inside of a cryostat that contains liquid helium pumped to a pressure of approximately 5 mbar. At this pressure, the liquid helium is superfluid, guaranteeing a temperature of 2 K of the immersed sample, and a clear transparency of the liquid (with no bubbles). With superconducting coils, we can apply a magnetic field between 0 and 2 T in Voigt configuration, or between 0 and 4 T in Faraday configuration.

2.5 Photo-induced Kerr rotation technique using a heterodyne detection

2.5.1 Experimental set-up

The pump-probe experiment using a heterodyne detection is based on the same principle as the homodyne experiment: polarized pump and probe pulses are focused on the sample delayed in time, except that here, the polarization of the probe beam is analyzed by reflection (Kerr effect) and its intensity is amplified due to the interference with a third beam called reference beam [20].

The experimental set-up of this second pump-probe experiment is shown in Fig. 2.6. The light source is a Titanium: Sapphire laser *Spectra Physics (Tsunami)* optically pumped with a 532 nm continuous laser of 8.5 W. The laser operates in the same spectral range as the Mira, and produces pulses with a similar duration of 2 ps. The principal beam is separated in three beams: pump, probe and reference beams.

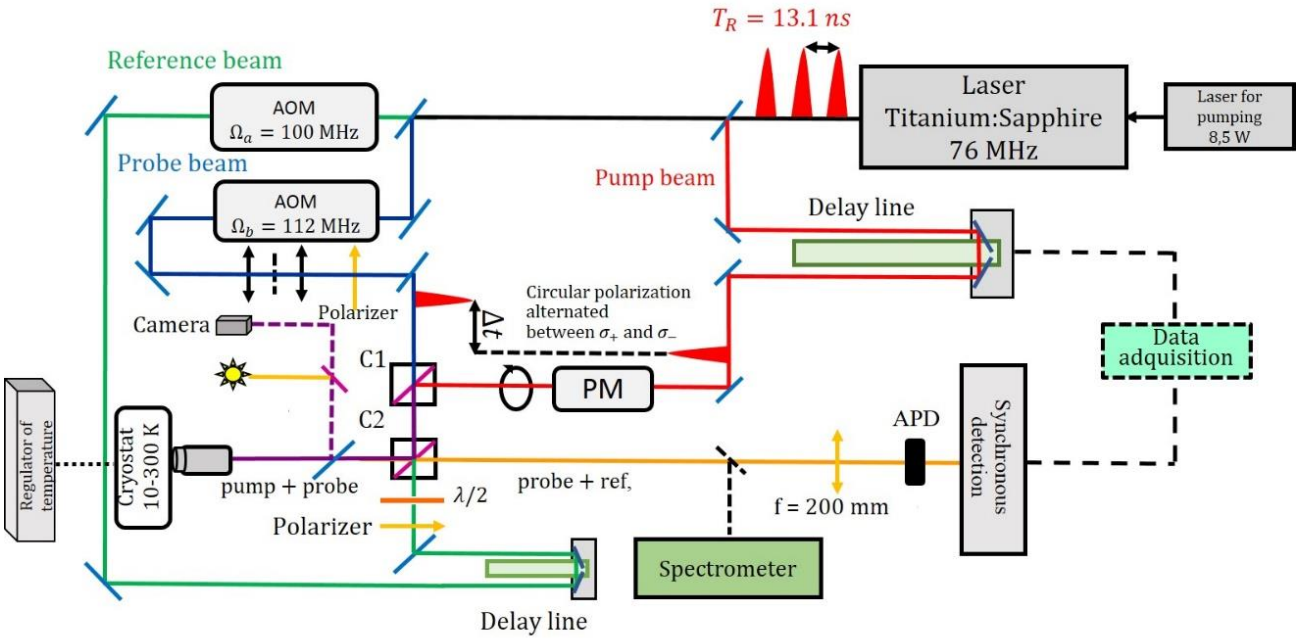

Figure 2.6 *Scheme of the PKR experiment, with heterodyne detection.*

The probe beam is focused on an acousto-optic modulator that selects the first order of diffraction and shifts up its frequency ω to $\omega + \Omega_a$, with Ω_a the frequency of the acoustic wave inside the modulator. Afterwards it is collimated with a pair of lenses, in order to reduce the divergence along the optical path, and linearly polarized in a perpendicular or parallel direction to the optical table. Then, it traverses a non-polarizing cube (C1) (that overlaps it with the pump beam) before arriving to a second cube (C2) that reflects it towards a microscope objective placed at the entrance of the cryostat.

The diameter of the focused pump beam is approximately 3 μm onto the sample, so this experimental arrangement allows to excite a low density of electrons bound to donors in comparison with the homodyne detection experiment. The spot given by the probe beam has a diameter of 1 μm on the sample surface.

In order to introduce a delay time between the pump and probe pulses, the pump beam is sent to a delay line of 250 mm, that contains a corner reflector positioned parallel to the displacement axis. In this experiment the pump beam only makes one round trip along of the delay line, so the maximum delay between the pump and probe pulses is 2 ns. Afterwards, the pump beam is sent to a photo-elastic modulator, working at a fixed frequency of f_{pump}= 50 kHz, to be circularly polarized (alternately between σ_+ and σ_- to avoid nuclear spin polarization) and arrives to the first cube (C1), in which it is superposed with the probe beam to follow the same path until the microscope objective, and ultimately until the sample surface.

The third beam, called reference beam, is also focused on an acousto-optic modulator, from which we recover the first diffracted order with an optical frequency ω shifted to $\omega + \Omega_b$(with Ω_b the frequency of the acoustic wave in the second acousto-optic modulator). For the heterodyne detection (at frequency $\Omega_b - \Omega_a = 2$ MHz), the optical path of the reference beam must be identical to that of the probe after the cube C_2 and until the APD photodiode. We use a delay line of approximately 25 mm to adjust in coincidence the probe and reference pulses at their arrival on the APD photodiode. After this delay line, the reference beam traverses a Glan Laser polarizer and a half-wave plate. Probe and reference beams are superposed at the cube C2 and both are focalized with a 200-mm focal lens at the same point on the avalanche photodiode.

The signal measured by the APD, that contains the information about the spin polarization created by the pump beam, is sent to a synchronous detection that first demodulates the signal at the high frequency, the heterodyne frequency $\Omega_b - \Omega_a =$ 2 MHz and then at the low frequency (50 kHz) of the photo-elastic modulator.

In this heterodyne experiment, the studied sample is placed in a cryostat with a circulation of liquid helium (Oxford High Res II). These types of cryostats allow to obtain temperatures between 4 K-400 K [21]; however, in practice the lowest temperature that can be reached is 5 K. A temperature regulator connected to the cryostat allows to vary the temperature of the sample holder between 5 K and 200 K. This allows us to study the evolution in temperature of the electron spin relaxation (Chapter 5).

The magnetic field is here applied using a pair of permanent magnets placed in the plane of the sample holder, which allows to obtain a magnetic field of 0.56 T in Voigt configuration.

2.5.2 Heterodyne detection

When the probe beam interacts with the sample, a change of its plane of polarization due to the Kerr effect occurs. In order to amplify and detect a signal proportional to the spin polarization contained in the angle of rotation of polarization of the probe beam, this beam is superposed with the reference beam. The avalanche photodiode detects the interference of both beams.

In a heterodyne detection, two signals with close frequencies are mixed, giving as a result a signal posessing a component whose intensity is the product of both amplitudes, and whose frequency is equal to the difference of both frequencies [20].

In our pump-probe experiment, the optical frequencies of first orders of diffraction of the probe and reference beams are shifted by a frequency $f_1 = 112$ MHz and $f_2 = 110$ MHz respectively. The intensity of the signal that reaches the detector can be written as

$$S(t) = I_{probe} + I_{ref} + 2\,\langle \vec{E}_{donors}.\vec{E}_{ref}\rangle \cos(2\pi(f_1 - f_2)t), \qquad (2.29)$$

where $\vec{E}_{donors}$ is alternated at the frequency $f_{II} = 50$ kHz ($\vec{E}_{donors}$ is $\vec{E}_R$ of section 2.2). Fig. 2.7 describes the origin of S(t) with this form.

The signal $S(t)$, at the first stage, is demodulated at the fast frequency that is $f_I = f_1 - f_2 = 2$ MHz, thanks to a reference signal electronically generated. This first demodulation is operated over a period time τ_I such that $1/f_I < \tau_I < 1/f_{II}$, which eliminates all the terms in equation (2.29), keeping only the last one. At the second stage, the resulting signal is demodulated at the frequency of the photo-elastic modulator, $f_{II} = 50$ kHz.

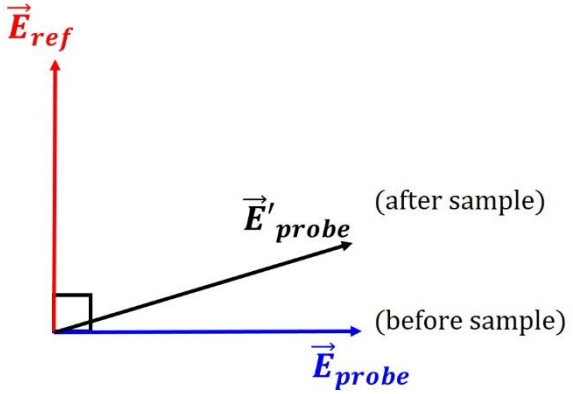

Figure 2.7 *In absence of the pump pulses, the polarization of the pump and reference beams are tuned to be orthogonal. In presence of pump pulses, the spin polarized donor-bound electrons modifies the polarization of the exiting probe beam:* $\langle \vec{E}_{donors}.\vec{E}_{ref}\rangle \propto cos(2\pi f_{II} t)$

2.6 Bibliography of Chapter 2

[1] R. R. Parsons, Phys. Rev. Lett. **23**, 1152 (1969).
[2] A. Al-Qasimi, O. Korotkova, D. James, and E. Wolf, Opt. Letters **32**, 1015 (2007).
[3] R.W. Wood and A. Ellett, Phys. Rev. **24**, 243 (1923).
[4] M. D'yakonov, *Spin Physics in Semiconductors* (Springer-Verlag, Berlin, 2008).
[5] E.B. Aleksandrov, V.S. Zapasskii, JETP **54**, 64 (1981).
[6] Y. G., Kusrayev, Semicond. Sci. Technol. **23**, 114013 (2008).
[7] J. S. Colton, T. A. Kennedy, A. S. Bracker, and D. Gammon, Phys. Rev. B **69**, 121307(R) (2004).
[8] J. Baumberg, D. D. Awschalom, and N. Samarth, J. Appl. Phys. **75**, 6199 (1994).
[9] N.I. Zheludev, M.A. Brummell, A. Malinowski, S.V. Popov, R.T. Harley, Solid State Commun. **89**, 823 (1994).
[10] V. V. Belykh, E. Evers, D. R. Yakovlev, F. Fobbe, A. Greilich, and M. Bayer, Phys. Rev. B **94**, 241202(R) (2016).
[11] M. Faraday, *On the magnetization of light and the illumination of magnetic lines force*, Philos. Trans R. Soc. London, **136** (1846).
[12] E. Hecht, *Optics* (Addison- Wesley, 2002).
[13] Y. R. Shen, The principles of Nonlinear Optics (Wiley, New York, 1984), chapter 21; E. T. Jaynes and F. W. Cummings, Proc. IEEE 51, **89** (1963).
[14] D. G. Fink, *Electronics Engineers' Handbook* (McGraw Hill, 1975).
[15] F. Bernardot, *Introduction à l'Optique électromagnétique* (Hermès Science Publication, France 2018).
[16] J. C Aguilar, PhD Thesis, National Institute of Astrophysics, Optics and Electronics, 2009.
[17] B. Siarry, PhD Thesis, Université Pierre et Marie Curie 2016.
[18] I. Merkulov, A. Efros and M. Rosen, *Electron spin relaxation by nuclei in semiconductor quantum dots*, Physical Review B **65,** 205309 (2002).
[19] P. F. Braun, X. Marie, L. Lombez, B. Urbaszek, T. Amand, P. Renucci, V. K. Kalevich, K. V. Kavokin, O. Krebs, P. Voisin, and Y. Masumoto, *Direct Observation of the Electron Spin Relaxation Induced by Nuclei in Quantum Dots,* Phys. Rev. Lett. **94**, 116601 (2005).
[20] W. J. Witteman, *Detection and Signal Processing: Technical Realization*, (Springer, 2006).
[21] Oxford instruments, *Product guide*.

Chapter 3

Electron exchange energy for neutral donors inside a quantum well

Content

3.1 Introduction

The exchange interaction between localized electrons is one of the oldest topics in quantum mechanics. In the last decade, the strong interest in controlling and manipulating localized spins in solid-state systems, has renewed this topic. Two main challenges are related with the exchange energy between spin qubits: (i) the enhancement of the relaxation and coherence times, and (ii) the mechanism of the entanglement in a pair of qubits. We are concerned here by the first point; hence it is of prime importance to evaluate the exchange energy of neighboring donors in the studied samples, and its variation with the donor concentration.

In this chapter, we calculate the exchange energy between two electrons bound to neutral donors inside an infinite quantum well. As we will see, the electron exchange appears as a result of the overlap of the wave functions of two localized states. Since this overlap increases exponentially with decreasing distance between a pair of donors, it becomes more important for larger concentrations of donors, especially near the metal-insulator transition.

The calculation of the exchange energy in the limit of large distances was first explored in the 1920's [1]. A more appropriate method to calculate it in the limit of large distances between donors was later developed by Gor'kov and Pitaevskii [2], and Herring and Flicker [3]. In this method, they calculated the exchange energy between two donor-bound electrons reducing its expression to an integral over a hyperplane in a six-dimensional space, and finally getting an analytical formula for bulk systems.

Later, Ponomarev *et al*. [4] proposed a procedure to obtain an expression valid for any interdonor distance. This procedure is based on an interpolation between the exchange energy at zero distance (i.e. the one of the helium atom) and the known asymptotic behavior. The same authors also calculated the asymptotic and interpolated exchange energies for artificial two-dimensional systems of electrons confined to the same plane as the impurities [4], and 2D electrons bound to Coulomb centers which are located outside the plane [5].

In this chapter, after a recall of the 3D calculations, we calculate the electron exchange energy of a pair of donor-bound electrons placed in the middle of an infinite QW, for large interdonor distances and for different QW thicknesses. We did this adapting to a QW the method developed by Refs. [2,3]. Then, inspired by the interpolation procedure proposed by Ponomarev *et al.* [4], we calculate the exchange energy of a "helium atom" inside an infinite quantum well, and finally obtain by interpolation the exchange energy valid for any inter-donor distance and for any QW thickness.

3.2 Calculation of the exchange energy (3D case)

This section summarizes the theoretical results of Refs. [2,3]. Let's consider two electrons, 1 and 2, localized at low temperature on two donors A and B. Both donors are located at fixed positions $x_A = -a$ and $x_B = +a$. The Hamiltonian describing the system of both donor-bound electrons is

$$\widehat{H} = -\frac{\Delta_1}{2} - \frac{\Delta_2}{2} - \frac{1}{r_{1A}} - \frac{1}{r_{2B}} - \frac{1}{r_{1B}} - \frac{1}{r_{2A}} + \frac{1}{r_{12}} + \frac{1}{2a}\,, \tag{3.1}$$

where Δ_j is the Laplacian operator acting on electron j ($j = 1$ or 2), r_{jA} and r_{jB} are the distances of electron j to donors A and B, respectively, and $r_{12} = |\vec{r}_2 - \vec{r}_1|$ is the distance between the electrons. All the distances are expressed in units of effective (bulk) Bohr radius a_B^{*3D}, and the energies in units of effective hartree E_h^{*3D}, defined by

$$a_B^{*3D} = a_0\varepsilon_r(m_0/m_e^*),\ E_h^{*3D} = E_h(m_e^*/m_0\varepsilon_r^2), \tag{3.2}$$

with $a_0 = 4\pi\varepsilon_0\hbar^2/me^2 \approx 0.52918$ Å the Bohr radius of the atomic units and $E_h = e^2/4\pi\varepsilon_0 a_0 \approx 27.211$ eV the Hartree energy of the atomic units, with m_0 the electron mass, m_e^* the effective electron mass, and ε_r the dielectric constant.

Because $\widehat{H}$ does not depend on the spin, its eigenstates are made of products of an orbital stationary state $\Psi(\vec{r}_1, \vec{r}_2)$, that satisfies the orbital Schrödinger equation:

$$\widehat{H}\Psi = E\Psi, \tag{3.3}$$

with one of the two-electron four spin states:

State	S	S_z
$\frac{1}{\sqrt{2}}(\|\uparrow\downarrow\rangle - \|\downarrow\uparrow\rangle)$	0	0
$\|\uparrow\uparrow\rangle$	1	1
$\frac{1}{\sqrt{2}}(\|\uparrow\downarrow\rangle + \|\downarrow\uparrow\rangle)$	1	0
$\|\downarrow\downarrow\rangle$	1	-1

where $\vec{S} = \vec{S}_1 + \vec{S}_2$ is the total spin of the pair of electrons, and ↑ (↓) represents the spin +1/2 (-1/2) of an electron. The spin state with $S = 0$ (singlet state) changes sign when the electrons are interchanged, while the states with $S = 1$ (triplet states) don't.

The Pauli exclusion principle requires that the total wavefunction changes sign under the interchange of both electrons. Therefore the symmetrical solutions Ψ_S [$\Psi_S(\vec{r}_2, \vec{r}_1) =$

$\Psi_S(\vec{r}_1, \vec{r}_2)$] for the orbital part describe singlet states (S = 0), and the antisymmetric solutions [$\Psi_A(\vec{r}_2, \vec{r}_1) = -\Psi_A(\vec{r}_1, \vec{r}_2)$], triplet states ($S = 1$).

As it is known [6], the ground state of a two-electron system is a singlet state, and the first-excited state a triplet. Let's denote Ψ_S and E_S the wave-function and energy of the ground state, and Ψ_A and E_A the ones of the first-excited state.

The energy difference between the first-excited and the ground levels, $E_A - E_S = 2J$, is called *exchange energy*, or *exchange splitting*, of the two-electron system. We use here, and in all the following, a positively-defined exchange energy, $2J > 0$: the Hamiltonian $\widehat{H}$ of Eq. (3.1) then corresponds to the spin Hamiltonian $\widehat{H}_{spin} = +2J\, \vec{S}_1.\vec{S}_2$.

The first calculation of the exchange energy $2J$, in the limit of large distances $R = 2a$ between donors, was done in the 1920's by Heitler and London [1]. In this method, they calculated the electron exchange energy between a pair of hydrogen atoms, taking as starting wave functions symmetrized and antisymetrized combinations of the electron wave-functions in an isolated atom $\phi_A(\vec{r}), \phi_B(\vec{r})$:

$$\Psi_{S,A}(\vec{r}_1, \vec{r}_2) = \frac{1}{\sqrt{2}}\big(\phi_A(\vec{r}_1)\phi_B(\vec{r}_2) \pm \phi_A(\vec{r}_2)\phi_B(\vec{r}_1)\big). \tag{3.4}$$

However, as Gor'kov and Pitaevskii [2] remarked later, it is necessary for a correct calculation to take into account correlations between both electrons. Their calculations have been revisited by Herring and Flicker [3].

Let's consider the functions defined by $\Psi_1 = \Psi_S + \Psi_A$ and $\Psi_2(\vec{r}_1, \vec{r}_2) = \Psi_1(\vec{r}_2, \vec{r}_1)$. The function Ψ_1 is large only when the electron 1 is near the proton A and electron 2 near proton B. We define the hyperplane Σ in the six-dimensional coordinate space $\{\vec{r}_1, \vec{r}_2\}$, with the x direction along the inter-nuclear line A-B, as

$$x_1 = x_2; \tag{3.5}$$

then the function Ψ_1 is located almost entirely on the "left side" ($x_1 < x_2$) of Σ, while the function Ψ_2 is located on the "right side" ($x_1 > x_2$), see Fig. 3.1.

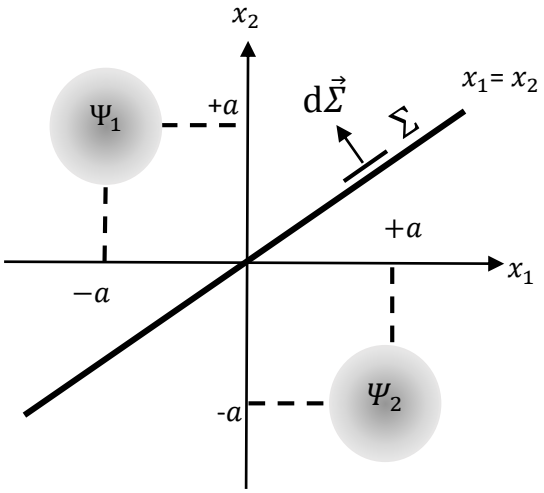

Figure 3.1 *Schematic representation of the hyperplane Σ, $x_1 = x_2$, in the six-dimensional coordinate space defined by the coordinates $\{\vec{r}_1, \vec{r}_2\}$. Because of its definition, the function Ψ_1 is located almost entirely on the "left side" of Σ, while the function Ψ_2 is located on the "right side".*

Calculating, over the "left side" of the hyperplane Σ, the integral $\iint_\Omega (\Psi_A \hat{H}\, \Psi_S - \Psi_S \hat{H}\, \Psi_A)\, d^3r_1\, d^3r_2$ and considering that Ψ_A and Ψ_S are eigenfunctions of the Hamiltonian $\hat{H}$, one obtains

$$\begin{aligned} \iint_\Omega (\Psi_A \hat{H}\, \Psi_S - \Psi_S \hat{H}\, \Psi_A)\, d^3r_1\, d^3r_2 &= (E_S - E_A) \iint_\Omega \Psi_A \Psi_S d^3r_1\, d^3r_2 \\ &= \tfrac{(E_S - E_A)}{4} \iint_\Omega (\Psi_1^2 - \Psi_2^2) d^3r_1\, d^3r_2 \\ &= E_S - E_A = -2\,J. \end{aligned} \tag{3.6}$$

The contribution of Ψ_2^2 is neglected, because the integration is over the "left side" of Σ . Turning the volume integral to a surface one, the exchange energy is expressed as

$$2J = \int_\Sigma \Psi_2\, \vec{\nabla}\Psi_1 . d\vec{\Sigma}\,, \tag{3.7}$$

with $d\vec{\Sigma}$ the surface element pointing towards the $x_2 > x_1$ region. At this stage, the function Ψ_1 can be approximated in Eq. (3.7) by the expression

$$\Psi_1(\vec{r}_1, \vec{r}_2) = \phi_A(\vec{r}_1)\phi_B(\vec{r}_2)\chi(\vec{r}_1, \vec{r}_2)\,, \tag{3.8}$$

where $\phi_A(\vec{r}) = \phi_1(\vec{r} - \vec{R}_A)$ is the one-electron ground-state wavefunction on donor A, located at $\vec{R}_A$; $\phi_B(\vec{r}) = \phi_1(\vec{r} - \vec{R}_B)$ is the one for donor B, located at $\vec{R}_B$; and $\chi(\vec{r}_1, \vec{r}_2)$ is a slowly-varying correlation function manifesting that, because of the Pauli principle, the two electrons are avoiding each other: $\chi(\vec{r}_1, \vec{r}_2) = 0$ for $\vec{r}_1 = \vec{r}_2$.

In order to determine the function $\chi(\vec{r}_1, \vec{r}_2)$ in the 3D case, $\Psi_1(\vec{r}_1, \vec{r}_2)$ is inserted in eq. (3.3) with ξ_1 the eigenvalue:

$$\hat{H}\Psi_1 = \xi_1\Psi_1. \tag{3.9}$$

Since χ is a slowly varying function, only the first derivatives of χ in equation (3.9) can be kept and also, limiting to points near the x-axis, one can consider the approximation:

$$\frac{\partial\phi_A}{\partial x_1} \cong -\phi_A(\vec{r}_1)\ ,\ \frac{\partial\phi_B}{\partial x_2} \cong \phi_B(\vec{r}_2). \tag{3.10}$$

One reaches in this way an equation on the χ function:

$$\frac{\partial\chi}{\partial x_1} - \frac{\partial\chi}{\partial x_2} + \left(\frac{1}{R} + \frac{1}{r_{12}} - \frac{1}{r_{1B}} - \frac{1}{r_{2A}}\right)\chi = 0, \tag{3.11}$$

where $R = 2a$. ξ_1 has disappeared because of the approximation $\xi_1 \approx 2\varepsilon_1$, with ε_1 the energy of the ground state for a one-electron Hamiltonian.

The solution of Eq. (3.11) is [2]

$$\chi_{3D}(\vec{r}_1, \vec{r}_2) = \frac{2a(2a + x_1 + x_2)}{(a - x_1)(a + x_2)}\ \exp\left(-\frac{a + x_1}{2a}\right)\left\{\frac{\sqrt{(x_1 - x_2)^2 + \rho_{12}^2} + x_2 - x_1}{\sqrt{(2a + x_1 + x_2)^2 + \rho_{12}^2} + 2a + x_1 + x_2}\right\}^{1/2} \tag{3.12a}$$

for $x_1 + x_2 < 0$, and

$$\chi_{3D}(\vec{r}_1, \vec{r}_2) = \frac{2a(2a - x_1 - x_2)}{(a - x_1)(a + x_2)}\ \exp\left(-\frac{a - x_2}{2a}\right)\left\{\frac{\sqrt{(x_1 - x_2)^2 + \rho_{12}^2} + x_2 - x_1}{\sqrt{(2a - x_1 - x_2)^2 + \rho_{12}^2} + 2a - x_1 - x_2}\right\}^{1/2} \tag{3.12b}$$

for $x_1 + x_2 > 0$, with $\rho_{12} = \sqrt{(y_1 - y_2)^2 + (z_1 - z_2)^2}$.

Finally, substituting this expression of χ_{3D} in the integral (3.7) for the exchange energy $2J$, we get this expression in 3D [3]:

$$2J(R \gg 1) = 4\sqrt{\pi}\, R^{\frac{5}{2}}\, e^{-2R} \int_0^1 dq\, e^{-q} q^{\frac{3}{2}} (2 - q)^{\frac{1}{2}}. \tag{3.13}$$

That can be expressed as

$$2J_{3D}(R \gg 1)\ =\ 1.6366\, R^{5/2}\, \mathrm{e}^{-2R}\ ; \tag{3.14}$$

let us recall that $2J_{3D}$ is in units of effective hartree, and $R = 2a$ in units of effective Bohr radius, see Eq. (3.2).

3.3 Calculation in an infinite quantum well (R>>1)

The case of two donors placed in the mid-plane $z = 0$ of an infinite QW, of thickness L, introduces an extrinsic confinement of the $3D$ one-electron wavefunctions. In order to calculate the exchange energy given by the expression (3.7) in a QW, we employed the one-electron ground-state wave-function $\phi_1(\vec{r})$ studied in Appendix B, with atomic number $Z = 1$:

$$\phi_1(\rho, z) = A_1 \exp(-\alpha_1 r) \cos\left(\pi \frac{z}{L}\right), \tag{3.15}$$

where $r = \sqrt{\rho^2 + z^2}$ and the factor $\cos(\pi z/L)$ is a single sinusoid arch that ensures that the wave-function $\phi_1(\rho, z)$ vanishes at the boundaries of the QW. In these expressions, the z axis is normal to the QW, the donor is at the origin of coordinates, and $\rho = \sqrt{x^2 + y^2}$.

The first step is to calculate the slowly varying correlation function $\chi(\vec{r}_1, \vec{r}_2)$. Following the steps of the method developed to reach $2J(R \gg 1)$ in $3D$ [2,3], it turns out that the function $\chi(\vec{r}_1, \vec{r}_2)$ obeys the equation:

$$\alpha_1 \left(\frac{\partial \chi}{\partial x_1} - \frac{\partial \chi}{\partial x_2}\right) + \left(\frac{1}{2a} + \frac{1}{r_{12}} - \frac{1}{a - x_1} - \frac{1}{a + x_2}\right)\chi = 0\,, \tag{3.16}$$

in which we have only kept the first derivatives of χ, and considered that both electrons are near the x axis, with $x_1 > -a$ and $x_2 < a$, so the approximations $\frac{\partial \phi_A}{\partial x_1} \approx -\alpha_1 \phi_A(\vec{r}_1)$, $\frac{\partial \phi_B}{\partial x_2} \approx +\alpha_1 \phi_B(\vec{r}_2)$ can be done.

As it can be seen, the function χ^{α_1} satisfies the equation (3.11) met in 3D. Considering the limit conditions $\chi \to 1$ when $x_1 \to -a$ or $x_2 \to a$, this means that χ^{α_1} coincides with the $3D$ correlation function χ_{3D}, see equations (3.12). We then deduce that the correlation function χ is given by

$$\chi(\vec{r}_1, \vec{r}_2) = \chi_{3D}(\vec{r}_1, \vec{r}_2)^{1/\alpha_1}. \tag{3.17}$$

Noticeably, this expression of $\chi(\vec{r}_1, \vec{r}_2)$ goes to the right $3D$ limit [2] when $\alpha_1 \to 1$ (for $L \to \infty$), and also to the right $2D$ limit [4,5] when $\alpha_1 \to 2$ (for $L \to 0$).

We are now able to express the exchange energy $2J(R \gg 1)$ in its integral form (3.7) Retaining only derivatives of ϕ_1 with respect to x_1 and x_2, and neglecting the terms containing the derivatives of χ, we obtain

$$2J = 8\alpha_1 \int_0^a dx_1 \int_{-\infty}^{+\infty} dy_1 dy_2 \int_{|z_{1,2}|<L/2} dz_1 dz_2\, \Psi_1(\vec{r}_2, \vec{r}_1)|_{x_2=x_1} \Psi_1(\vec{r}_1, \vec{r}_2)|_{x_2=x_1}, \tag{3.18}$$

which it is turned with some algebra to

$$2J(R \gg 1) \;=$$
$$4\,\alpha_1 \left(\frac{8}{\mathrm{e}}\right)^{\frac{1}{\alpha_1}} A_1^4\, R^{3-\frac{1}{2\alpha_1}}\, \mathrm{e}^{-2\alpha_1 R} \int_0^1 dX \int_{|Z_{1,2}|<\frac{L}{2\sqrt{R}}} dZ_1 dZ_2 \int_{-\infty}^{+\infty} dY_1 dY_2 \;\times \cdots$$
$$\cos^2\left(\frac{\pi\sqrt{R}Z_1}{L}\right)\cos^2\left(\frac{\pi\sqrt{R}Z_2}{L}\right)\exp\left\{-\frac{2\alpha_1(P_1^2+P_2^2)}{1-X^2}+\frac{X}{\alpha_1}\right\}\left[\frac{P_{12}}{(1+X)^2(1-X)}\right]^{\frac{1}{\alpha_1}}, \tag{3.19}$$

using $R = 2a$, the change of variables $x_1 = aX$, $y_{1,2} = Y_{1,2}\sqrt{R}$, $z_{1,2} = Z_{1,2}\sqrt{R}$, and the notations $P_j = \sqrt{Y_j^2 + Z_j^2}$ ($j = 1$ or 2) and $P_{12} = \sqrt{(Y_1 - Y_2)^2 + (Z_1 - Z_2)^2}$.

The expression (3.19) of the exchange energy $2J(R \gg 1)$ can be calculated numerically, for given values of the thickness L of the QW (for a given L, α_1 and A_1 are known, see Appendix B). In order to decrease the numerical integration time, we turned the 5-dimensional integral (3.19) to a 4-dimensional one, using the change of variables

$$S_1 = \frac{Y_1 + Y_2}{2}\,, \quad S_2 = \frac{Z_1 + Z_2}{2}\,, \quad D_1 = Y_1 - Y_2\,, \quad D_2 = Z_1 - Z_2\,; \tag{3.20}$$

the integration over variable S_1 can be performed, and we finally used the following expression (3.21) for our numerical calculations:

$$\begin{aligned} 2J(R \gg 1) \;=\; & 4\sqrt{\pi\alpha_1}\left(\frac{8}{\mathrm{e}}\right)^{\frac{1}{\alpha_1}} A_1^4\, R^{3-\frac{1}{2\alpha_1}}\, \mathrm{e}^{-2\alpha_1 R} \int_0^1 dX \sqrt{1-X^2}\left[\frac{\mathrm{e}^X}{(1+X)^2(1-X)}\right]^{\frac{1}{\alpha_1}} \times \ldots \\ & \int_0^{+\infty} dD_1 \int_0^{\frac{L}{\sqrt{R}}} dD_2\, (D_1^2 + D_2^2)^{\frac{1}{2\alpha_1}} \exp\left[-\frac{\alpha_1(D_1^2+D_2^2)}{1-X^2}\right] \times \ldots \\ & \left\{ \cos^2\left(\frac{\pi\sqrt{R}D_2}{L}\right)\int_0^{\frac{L}{2\sqrt{R}}-\frac{D_2}{2}} dS_2 \exp\left[-\frac{4\alpha_1 S_2^2}{1-X^2}\right] + \right. \\ & 2\cos\left(\frac{\pi\sqrt{R}D_2}{L}\right)\int_0^{\frac{L}{2\sqrt{R}}-\frac{D_2}{2}} dS_2 \cos\left(\frac{2\pi\sqrt{R}S_2}{L}\right)\exp\left[-\frac{4\alpha_1 S_2^2}{1-X^2}\right] + \\ & \left. \int_0^{\frac{L}{2\sqrt{R}}-\frac{D_2}{2}} dS_2 \cos^2\left(\frac{2\pi\sqrt{R}S_2}{L}\right)\exp\left[-\frac{4\alpha_1 S_2^2}{1-X^2}\right] \right\}. \end{aligned} \tag{3.21}$$

When $L \to \infty$ or $L \to 0$, Eq. (3.21) goes to the formulas known in $3D$ or $2D$, respectively (see Refs [3-5]):

$$2J_{3D}(R \gg 1) \;=\; 1.6366\, R^{5/2}\, \mathrm{e}^{-2R}\,; \tag{3.22}$$

$$2J_{2D}(R \gg 1) \;=\; 30.413\, R^{7/4}\, \mathrm{e}^{-4R}\,. \tag{3.23}$$

Figure 3.2 shows the exchange energy $2J(R \gg 1)$ as a function of the distance $R = 2a$ between the pair of donors, for several values of the QW thickness L. The $2J$ values for $R \sim 1$, and below, have *a priori* no physical significance, because we fixed $R \gg 1$ from start.

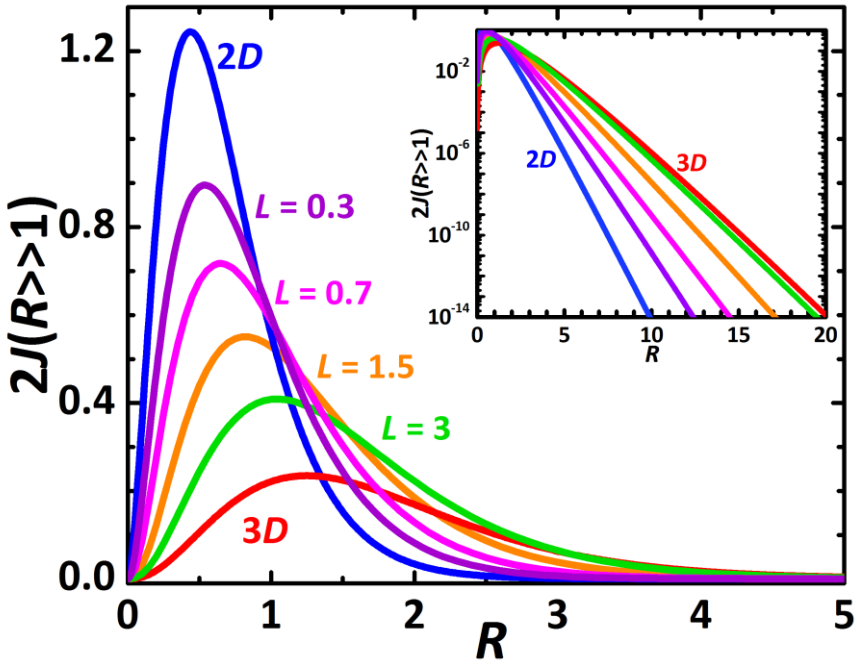

Figure 3.2. *Exchange energy* $2J(R \gg 1)$ *for several values of the QW thickness L, as a function of the distance R between two donor-bound electrons, centred inside the QW. The curves noted* $2D$ *and* $3D$ *correspond to the* $L \to 0$ *and* $L \to \infty$ *limits, respectively. Inset: semi-logarithmic representation of the same data, for a larger range of R.*

3.4 Determination of 2J(R) for any inter-donor distance

3.4.1 General procedure to obtain an interpolated formula of $2J(R)$ for the 3D and 2D cases

In Ref. [4] a procedure has been proposed to build the exchange energy $2J(R)$ for any value of the distance R between the donors, in the 3D and 2D cases. The principal idea of this method consists in matching the second derivative of the electron exchange energy between two regions or R, $R \to 0$ and $R >> 1$.

This procedure requires:

(i) an asymptotic form for the exchange energy: $2J(R \gg 1) = CR^{\beta}\mathrm{e}^{-\omega R}$;

(ii) the value of the exchange energy at $R = 0$, this means the singlet-triplet energy difference $2J_0$ of the $3D$ and $2D$ helium atom;

(iii) the assumption that at small distance between donors, $\ln[2J(R \ll 1)]$ can be expanded as $\ln(2J_0) - \gamma R - \tilde{A}R^2 \cdots$, with γ and $\tilde{A}$ both positive.

If we calculate now the second derivative of *2J* in both regions, we get

$$\frac{d^2\ln[2J(R)]}{dR^2} = \begin{cases} -\dfrac{\beta}{R^2} & (R \gg 1) \\ -2\tilde{A} & (R \ll 1). \end{cases}$$

The simplest formula that satisfies both conditions is the Lorentzian function

$$\frac{d^2\ln[2J(R)]}{dR^2} = -\frac{2\tilde{A}\beta}{\beta + 2\tilde{A}R^2}\ , \qquad (3.24)$$

supposed to be valid for any value of R.
A first integration of Eq. (3.24) gives the expression of the first derivative of $\ln[2J(R)]$:

$$\frac{d\ln(2J)}{dR}(R) = -\gamma - (\beta A)\arctan(AR), \qquad (3.25)$$

where $A = \sqrt{\frac{2\tilde{A}}{\beta}}$. This expression must be valid at large R; so matching this expression with the first derivative of the asymptotic form of the exchange energy, we obtain a relationship between γ and $\tilde{A}$:

$$A = \sqrt{2\tilde{A}/\beta} = \frac{2(\omega - \gamma)}{\pi\,\beta}\ . \qquad (3.26)$$

Finally, a second integration yields the interpolated formula for $2J(R)$ given by this procedure:

$$\ln[2J(R)] = \ln(2J_0) - \gamma R - \beta AR\arctan(AR) + \frac{\beta}{2}\ln(1 + A^2R^2)\,. \qquad (3.27)$$

This expression contains one single parameter, A (or γ), which remains to be determined. In Ref. [4], the authors have chosen the parameter A by fitting at best numerical values of $2J$ obtained for R of the order of unity or several units. They proposed in this way interpolated formulas for $2J(R)$ in the $3D$ and $2D$ cases, using a $2J_0$ value in $3D$ known at their time and, at $2D$, a value of $2J_0$ calculated by their own. The final interpolated formulas in 2D and 3D that they found are:

$$2J_{3D} = 0.770(1 + 0.23R^2)^{5/4}\exp[-0.1R - 1.210\ R\ \arctan(0.484\ R)] \quad (3.28\ a)$$
$$2J_{2D} = 3.567(1 + 1.81\ R^2)^{7/8}\exp[-0.3R - 2.355\ R\ \arctan(1.346\ R)] \quad (3.28\ b)$$

3.4.2 Interpolated $2J(R)$ in an infinite quantum well

In order to build an interpolated formula for the exchange energy between two donors located in the middle of an infinite QW, with the procedure described above, two points must be treated:

(i) the calculation of $2J_0$ in a "helium atom" centred in an infinite QW;

(ii) the creation of the interpolated $2J(R)$ starting with an asymptotic $2J(R \gg 1)$ which does *not* possess the form $2J(R \gg 1) = CR^{\beta}\mathrm{e}^{-\omega R}$.

For each point we proceeded as follows:

For the calculations that we made to obtain $2J_0$ in the middle of an infinite QW, first we noticed that, in $3D$ and in $2D$, calculating the ground energy E_S of the helium atom using the variational method, and the first-excited energy E_A perturbatively, gives a very good approximation of the exchange energy $2J_0$, which is found to be shifted from the exact numerical values by only about 1 % (see Appendix C). So we proceeded in the same way to calculate the exchange energy of a "helium atom" located in the midplane of an infinite QW; the calculations of E_S and E_A are presented in Appendix C. Figure 3.3 shows $2J_0$ as a function of the thickness L of the QW; as it is observed, $2J_0$ decreases monotonously with L, from the $2D$ value to the $3D$ one.

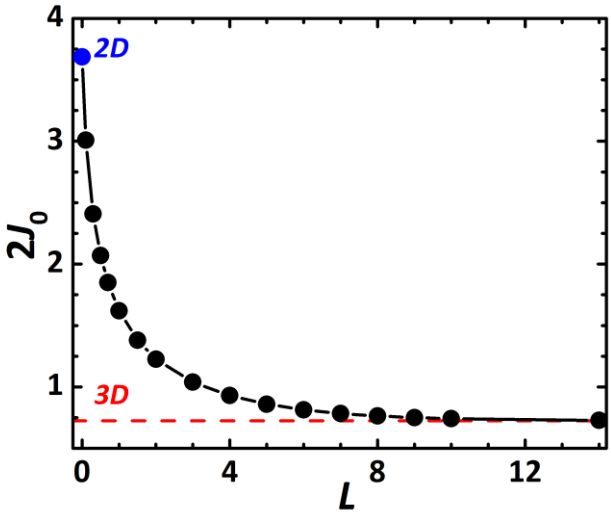

Figure 3.3 *Exchange energy $2J_0$ of a "helium atom" (full disks) centred in an infinite QW, as a function of the QW thickness L. The blue point at $L = 0$ corresponds to our calculated $2J_0$ in $2D$; the red dashed horizontal line indicates the value of our calculated $2J_0$ in $3D$ (continuous curve: guide for the eyes).*

Let us talk now about the construction of the interpolated $2J(R)$ in an infinite QW. The calculated asymptotic values of the exchange energy $2J(R \gg 1)$, see Fig. 3.2, do not possess exactly the form met in the $3D$ and $2D$ cases. Nevertheless, we realized that the fit of $2J(R \gg 1)$ with the form $CR^{\beta}\mathrm{e}^{-\omega R}$ is rather satisfactory for values of R ranging from $R = 0.1$ to 30 [see Fig. 3.4(a), red dashed line] ($R = 30$ corresponds to the distance between two donors for residual concentrations in typical semiconductors). Then the form $2J(R \gg 1) = CR^{\beta}\mathrm{e}^{-\omega R}$ can approximate very well the values found at large R. To obtain the parameters C, β and ω, we adjusted $\ln[2J(R \gg 1)]$ with $\ln C + \beta \ln R - \omega R$. Figure 3.4(b) shows these parameters for different thicknesses of the QW.

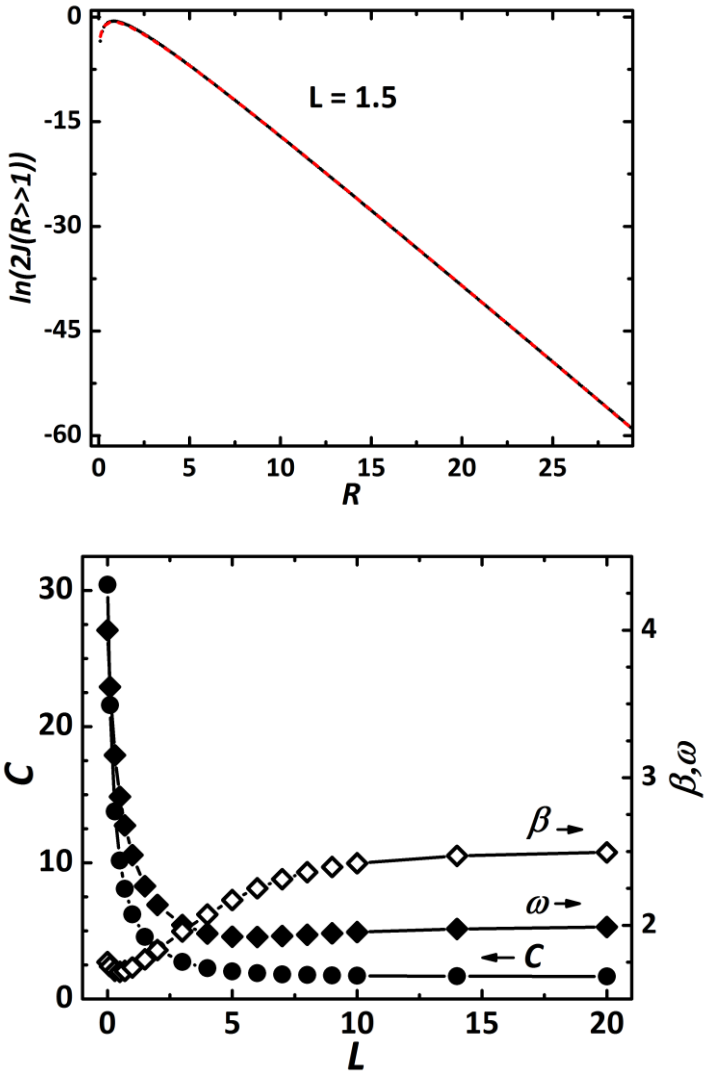

Figure 3.4 *(a) Fitting of the values 2J(R>>1) for L = 1.5 (black points) with the expression* $CR^{\beta}e^{-\omega R}$ *(red dashed line). (b) Fitting parameters C (full disks), β (open diamonds) and ω (full diamonds) of the exchange energy* $2J(R \gg 1)$ *fitted with the expression* $CR^{\beta}e^{-\omega R}$*, as a function of the QW thickness L. The values of C read on the left axis, the ones of β and ω on the right axis (continuous curves: guides for the eyes).*

Finally, we performed a fit of the values of $2J(R \gg 1)$ between $R = 20$ and 30 with Eq. (3.27), using the known values of $2J_0$ and β, with A the only fitting parameter [γ is linked to A, once β and ω are fixed, see Eq. (3.26)]. We created in this way an interpolated formula for $2J(R)$ inside an infinite QW, for any distance R of interest between the pair of donors. An example of interpolated exchange energy $2J(R)$ is given in Figure 3.5, for $L = 1.5$; its coincidence with the asymptotic form $2J(R \gg 1)$ occurs for $R \geq 2$.

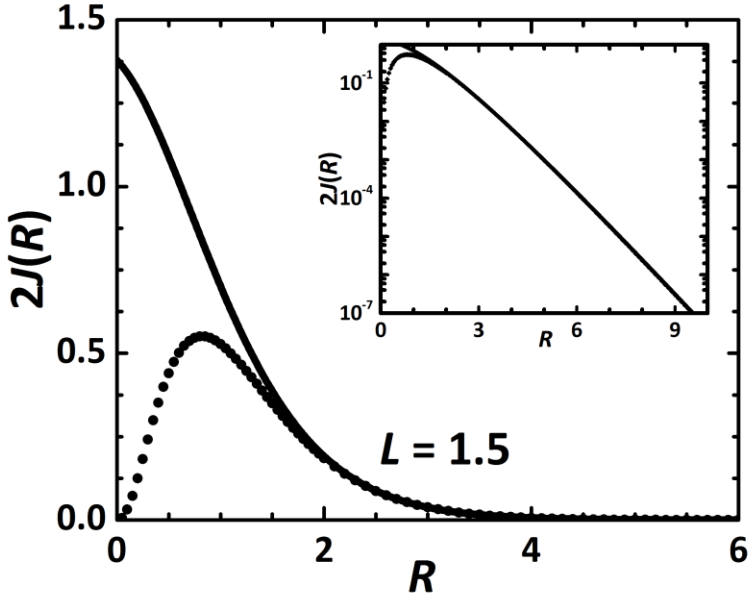

Figure 3.5. *Interpolated $2J(R)$ (continuous curve) and large-R $2J(R \gg 1)$ (dotted curve) exchange energies for the QW thickness $L = 1.5$, as a function of the distance R between two donor-bound electrons, centred inside the QW. Inset: semi-logarithmic representation of the same data, for a larger range of R.*

As special case, the interpolated formulas in $3D$ and $2D$ can be calculated following the procedure described above. We found

$$2J_{3D}(R) = 0.729\,(1 + 0.258R^2)^{\frac{5}{4}} \times \cdots \exp[-0.0005R - 1.270R \arctan(0.508R)]\,; \qquad (3.29a).$$

$$2J_{2D}(R) = 3.604\,(1 + 1.548R^2)^{\frac{7}{8}} \times \cdots \exp[-0.579R - 2.178R \arctan(1.244R)]\,. \qquad (3.29b)$$

These expressions are slightly different from the equations (3.28) coming from Ref. [4] (see Appendix D).

Figure 3.6 shows the values of the obtained parameters A and γ, as a function of the QW thickness L; monotonous evolutions of A and γ can be observed between the $2D$ ($L \to 0$) and $3D$ ($L \to \infty$) cases. For $L \geq 6$, the A and γ values are very close to the values at 3D.

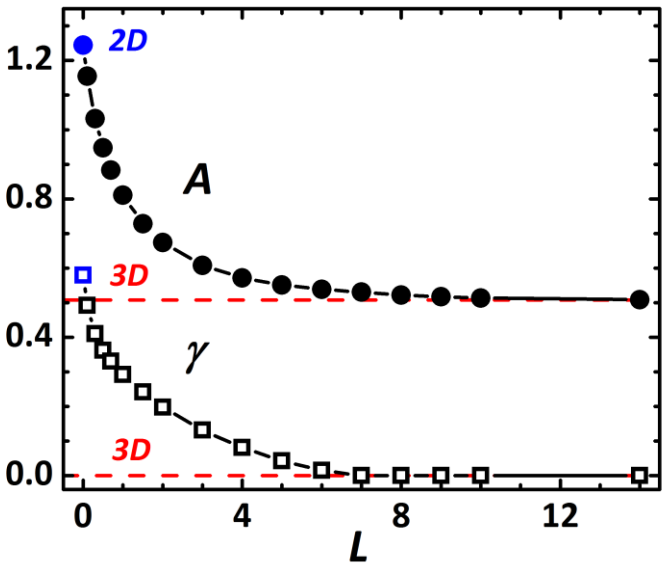

Figure 3.6. *Parameters A (full disks) and γ (open squares) entering in the expression of the interpolated* $2J(R)$ *exchange energy, see Eq. (3.27), as a function of the QW thickness L (continuous curves: guides for the eyes). The blue points at* $L = 0$ *correspond to the 2D case; the red dashed horizontal lines indicate the values in 3D.*

In Fig. 3.7, we plotted the interpolated exchange energy $2J(R)$ for several values of L, as a function of the distance R between two donor-bound electrons, centred inside the QW. Because we consider an infinite QW with a wavefunction completely confined in the QW, the calculations do not describe correctly the reality of the system for $L < 1$. Indeed, the electron wave-function of thin QWs, for which $L' = La_B^{*3D}$ is smaller than a_B^{*3D}, is in fact larger than the QW thickness, and then overflows the barrier material which does not represent an infinite barrier for electrons. Figure 3.7(b) shows with more detail $2J(R)$ for $L \geq 1$ and 3D. For $L \leq 1$ (see Fig. 3.7 (a)), the exchange energy at very small $R < 1$ shows a maximum for $2D$ and a minimum for $3D$ with intermediate values for QWs of different L; however, for $R > 2$ the situation is inverted and the $3D$ value is larger than the value obtained in a QW or in $2D$ (see inset of Fig. 3.7 (a)).

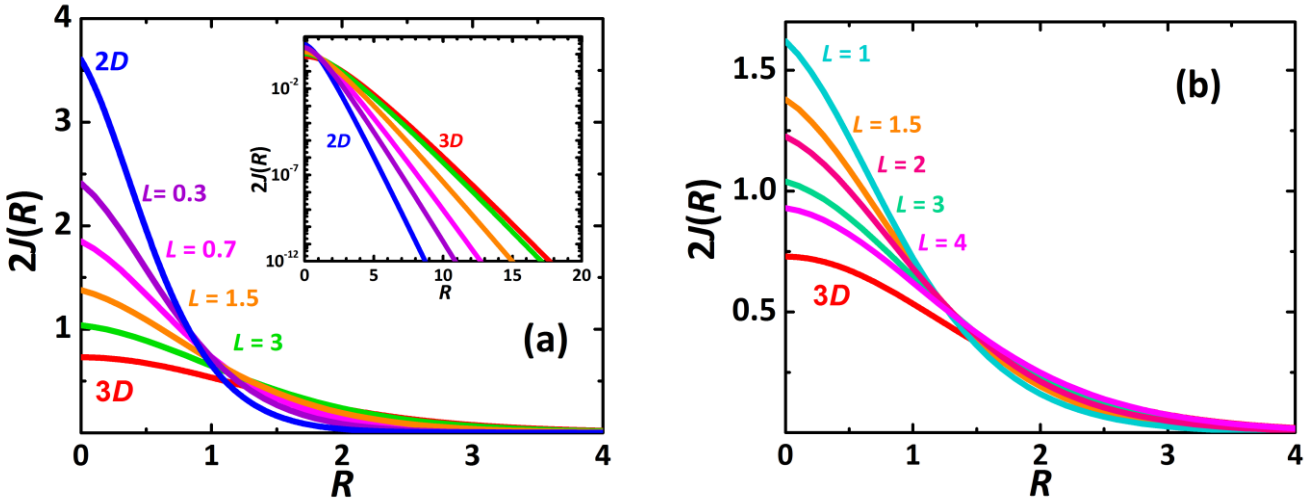

Figure 3.7. *(a) Interpolated exchange energy* $2J(R)$ *for the L values shown in Fig. 3.2, as a function of the distance R between two donor-bound electrons, centred inside the QW. The curves noted* $2D$ *and* $3D$ *correspond to the interpolated* $2J(R)$ *laws in* $2D$ *and in* $3D$*, respectively, see eqs.(3.29). Inset: semi-logarithmic representation of the same data, for a larger range of R. (b) Interpolated exchange energy* $2J(R)$ *for* $L = 1, 1.5, 2, 3, 4$ *and* $3D$.

3.5 Discussion

In Figs. 3.8(a) and 3.8(b), we have plot in common units of energy and length the exchange energy $2J'(r) = 2J(R = r/a_B^{*3D}) \times E_h^{*3D}$ between two donor-bound electrons as a function of the distance between donors $r = Ra_B^{*3D}$, fixing the width of the infinite QW at $L' = 10$ nm, for some usually studied semiconductor materials. The parameters for these compounds are indicated in Table 3.1

Material	**Effective mass** m_e^*/m_0	**Dielectric constant** ϵ_r	**Bohr radius** a_B^{*3D} **(nm)**	**Effective hartree** E_h^{*3D} **(meV)**	**Energy band gap** E_g **(eV)**	**Spin-orbit splitting** Δ_{SO} **(eV)**
ZnO	0.24[a]	7.77[b]	1.71	108	3.44[c]	0.0035[c]
ZnSe	0.145[b]	8.8[d]	3.21	51.0	2.820[e]	0.403[e]
GaN	0.13[f]	9.7[f]	3.95	37.6	3.28[f]	0.02[f]
CdSe	0.11[b]	10.16[d]	4.89	29.0	1.74[g]	0.462[h]
CdTe	0.09[i]	10.31[j]	6.1	23	1.606[e]	0.949[e]
GaAs	0.067[k]	12.35[d]	9.75	12.0	1.519[e]	0.341[e]

a: Ref. [7]; b: Ref. [8]; c: Ref. [9]; d: Ref. [10]; e: Ref. [11], f: Ref. [12]; g: Ref. [13]; h: Ref. [14], i: Ref. [15]; j: Ref. [16]; k: Ref. [17].

Table 3.1. *Values of the different parameters determining the electron exchange energy and the spin relaxation time near the insulator-metal transition, in usually studied semiconductor materials.*

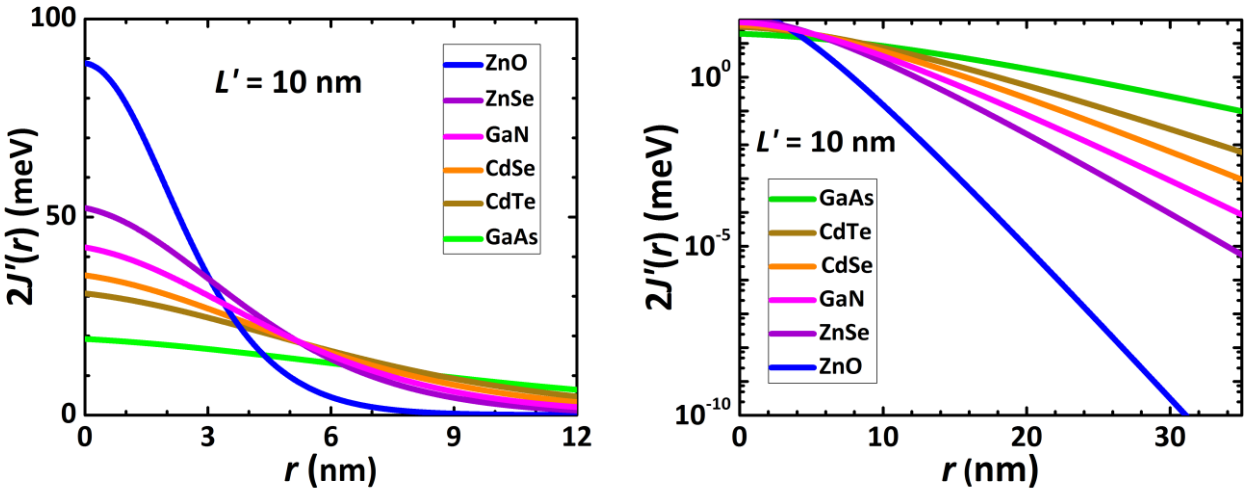

Figure 3.8 *Electron exchange energy in common unit of energy, as a function of inter-donor distance for several semiconductor materials, at a fixed value of QW thickness L' = 10 nm; (a) in linear scales and for small inter-donor distances; (b) in semi-logarithmic scales and for a larger domain of inter-donor distances.*

As we can see in Fig. 3.8(a) for small distance between donors (high doping concentrations), the $2J'(0)$ value is larger for materials with a higher effective Hartree energy. Indeed, a value close to 100 meV for ZnO is obtained, which is almost five times larger than the $2J'(0)$ value for GaAs. Figure 3.8(b) shows that, for large inter-donor distances (small doping concentrations), ZnO exhibits also the smallest value of exchange energy, meanwhile GaAs has the largest exchange energy among the materials used for comparison in this figure. We also remark that, for GaAs, the exchange energy of two electrons localized on donors decreases slightly when the inter-donor distance increases, meanwhile for ZnO the decrease is much faster. In general, the exchange energy is exponentially sensitive to the distance between donors, and this sensitivity depends also strongly on the effective Hartree energy which fixes the extension of the electron wavefunction for a given semiconductor material.

3.6 Conclusion

This chapter described the way to reach a general expression for the exchange energy of two electrons bound to donors placed in the middle of an infinite QW, valid for any inter-donor distance and for any QW thickness. In the next chapter 4, this tool will allow to calculate the spin relaxation time in QWs made of widely used II-VI and III-V direct-band-gap materials; in particular, it will be useful to interpret our experimental results on the spin relaxation time of donors inside a CdTe QW, at low temperature.

3.7 Bibliography of chapter 3

[1] W. Heitler and F. London, *Z.* Physik **44**, 455 (1927).
[2] L. P. Gor'kov and L. P. Pitaevskii, Dokl. Akad. Nauk SSSR **151**, 822 (1963) [Sov. Phys. Doklady **8**, 788 (1964)].
[3] C. Herring and M. Flicker, Phys. Rev. **134**, A362 (1964).
[4] I. V. Ponomarev, V.V. Flambaum, and A. L. Efros, Phys. Rev. B **60**, 5485 (1999).
[5] I. V. Ponomarev, V. V. Flambaum, and A. L. Efros, Phys. Rev. B **60**, 15848 (1999).
[6] N. W. Ashcroft and N. Mermin, S*olid state Physics,* (USA, Philadelphia, 1976)
[7] M. Oshikiri, Y. Imanaka, F. Aryasetiawan, and G. Kido, Physica B **298**, 472 (2001).
[8] N. Ashkenov *et al*., J. Appl. Phys. **93**, 126 (2003).
[9] W. J. Fana, J. B. Xiab, P. A. Agus, S. T. Tan, S. F. Yu, and X. W. Sun, J. Appl. Phys. **99**, 013702 (2006).
[10] R. Geick, C. H. Perry, and S. S. Mitra, J. Appl. Phys. **37**, 1994 (1966).
[11] H. Mayer and U. Rössler, Solid State Commun. **87**, 81 (1993).
[12] Bougrov et al., in *Properties of Advanced SemiconductorMaterials GaN, AlN, InN, BN, SiC, SiGe* edited by M.E. Levinshtein, S. L. Rumyantsev and M.S. Shur (John Wiley& Sons New York, 2001).
[13] S. Ninomiya and S. Adachi, J. Appl. Phys. **78**, 4681 (1995).
[14] H. Fu, L.W. Wang and A. Zunger, Phys. Rev. B **59**, 5568 (1999).
[15] I. Hernández-Calderón, in *II-VI Semiconductor Materials and their Applications*, edited by M. C. Tamargo (Taylor and Francis, New York, 2002).
[16] I. Strzalkowski, S. Joshi, and C. R. Crowell, Appl. Phys. Lett. **28**, 350 (1976).
[17] W. Nakwaski, Physica B **210**, 1 (1995).
[18] X. Linpeng, M. L. K. Viitaniemi, A. Vishnuradhan, Y. Kozuka, C. Johnson, M. Kawasaki, K-M C. Fu., arXiv:1802.03483v3 (2018).
[19] R. I. Dzhioev, K. V. Kavokin, V. L. Korenev, M. V. Lazarev, B. Ya. Meltser, M. N. Stepanova, B. P. Zakharchenya, D. Gammon, and D. S. Katzer, Phys. Rev. B **66**, 245204 (2002)
[20] R. I. Dzhioev, V. L. Korenev, I. A. Merkulov, B. P. Zakharchenya, D. Gammon, Al. L. Efros, and D. S. Katzer, Phys. Rev. Lett. **88**, 256801 (2002).
[21] K.V. Kavokin, Semicond. Sci. Technol. **23**, 114009 (2008).
[22] K. V. Kavokin, Phys. Rev. B **69**, 075302 (2004).
[23] N. F. Mott, *Metal insulator transitions* (Taylor and Francis, London, 1990).
[24] Y. Fu and M.W. Wu, J. Appl. Phys. **104**, 093712 (2008).
[25] J. Harmon, W.O. Putikka and R. Joynt, Phys. Rev. B **79**, 115204 (2009).
[26] G. E. Pikus and A. M. Titkov, in *Optical Orientation*, edited by F. Meier and B. P. Zachachrenya (North-Holland, Amsterdam, 1984).
[27] L. C. Lew Yan Voon, M. Willatzen, M. Cardona and N.E. Christensen, Phys. Rev. B **53**, 10703 (1996).
[28] B. Beschoten, E. Johnston-Halperin, D. K. Young, M. Poggio, J. E. Grimaldi, S. Keller, S. P. DenBaars, U. K. Mishra, E. L. Hu, and D. D. Awschalom, Phys. Rev. B **63**, 121202 (2001).
[29] S. Ghosh, V. Sih, W. H. Lau, and D. D. Awschalom, Appl. Phys. Lett. **86**, 232507 (2005).

Chapter 4

Spin relaxation time of donor-bound electrons in a CdTe quantum well: Dependence on doping concentration

Content

4.1 Previous studies in bulk materials

Driven by the spin-based application perspective, the study of impurity spin relaxation has seen renewed interest in the last two decades. The influence of the doping concentration on the spin relaxation time of donor-bound electrons has been studied at low temperature in different bulk materials, either with a zinc-blende structure such as GaAs [1-4], InSb [5], InAs [6] and ZnSe [7], or wurzite structure as: GaN [8,9] and ZnO [10], for different doping values in the insulating regime and beyond the metal-insulator transition (MIT).

In the insulating regime, at low temperature, the most comprehensive study in a zinc-blende semiconductor was carried out by Dzhioev *et al*., in bulk GaAs [1] (see Fig. 4.1 (a)). In this study, the spin relaxation time at low temperature shows a non-monotonous behavior exhibiting a maximum value of the order of 200 ns at $n_d \sim 3 \times 10^{15}$ cm^{-3}. This behavior was explained as an interplay of different relaxation mechanisms: at low doping density the hyperfine nuclear interaction is the most important mechanism, while at high doping concentration, the anisotropic exchange interaction mechanism dominates. This study has been recently revisited by V. V. Belykh *et al*. [2,3] and J. G. Lonnemann *et al*. [4].

In the metallic regime at low temperature, the experimental studies carried out in GaAs [1], InSb [5] and InAs [6] reveal that for very high doping concentrations above the MIT, the D'yakonov-Perel' (DP) or the Elliot-Yafet (EY) mechanisms dominate, depending on the characteristics of the material (energy band gap and spin-orbit constant).

We have chosen CdTe for this research because it has the same crystal structure (zinc-blende) and nearly the same energy band gap as GaAs, but rather different material parameters (e.g. effective masses, dielectric constants, nuclear spin characteristics and spin-orbit interaction). Up to now, in bulk CdTe, a recent study in the insulating regime was performed by D. Sprinzl *et al.* [11] (see Fig. 4.1 (b)). They reported also a non-monotonous behavior, exhibiting a maximum value of the spin relaxation time of 2.5 ns at $n_d = 4.9 \times 10^{16}$ cm^{-3} and a minimum value of 40 ps below $n_d = 1 \times 10^{15}$ cm^{-3}.

In this chapter, we measure the electron spin dephasing time T_2^* at T = 2 K as a function of the magnetic field, applied in Voigt geometry, by using the PFR technique described in Chapter 2. The electrons localized on iodine donors are placed in the middle of a 8nm CdTe QW. The donor concentration is in the range of 1×10^9 cm^{-2} to 3.6×10^{11} donors cm^{-2}.

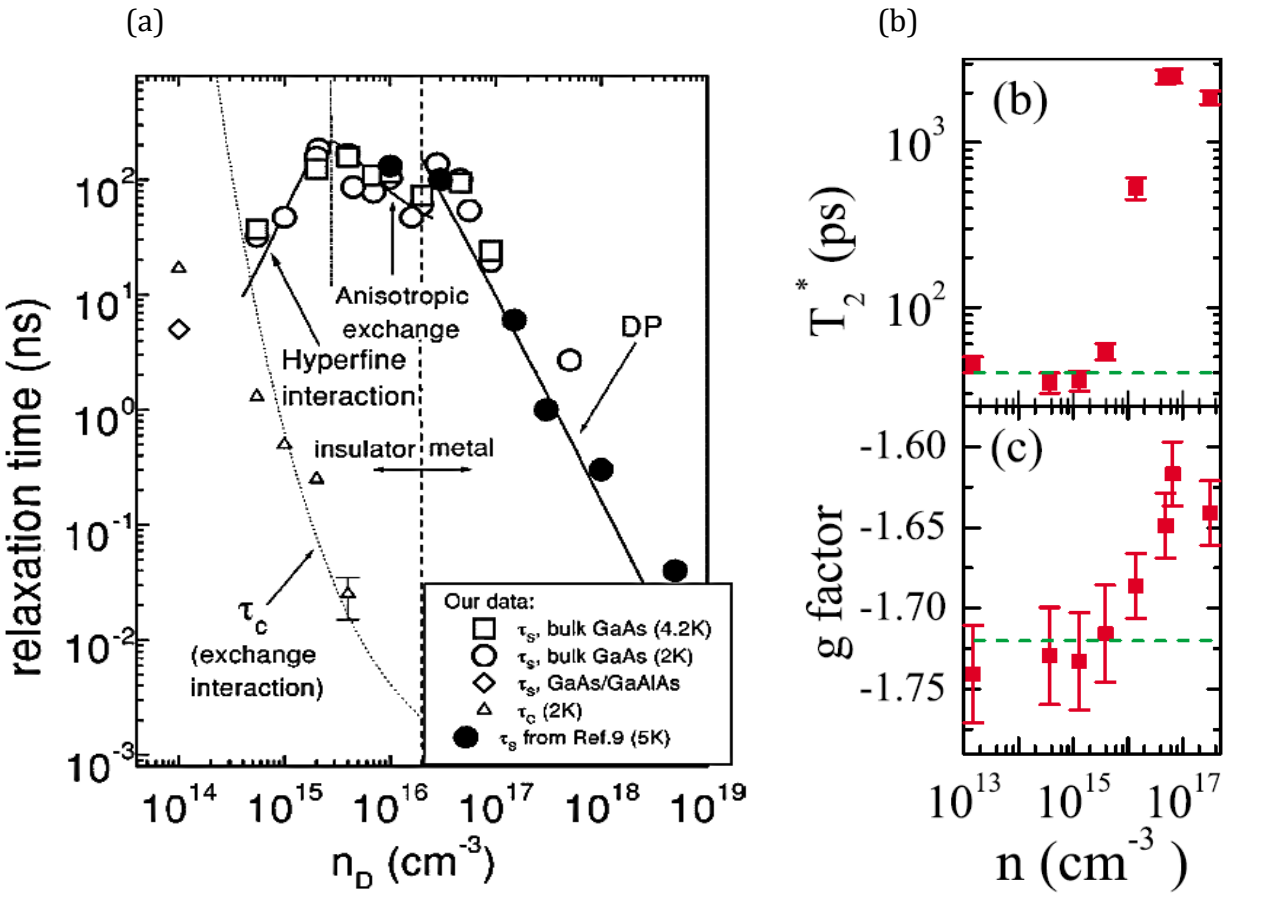

Figure 4.1 *Study of the influence of doping concentration on the spin relaxation time of donor-bound electrons in bulk (a) GaAs and (b) CdTe. The graphics were taken from Refs. [1] and [11], respectively. The longest relaxation times are those found in GaAs. Different techniques have been used to obtain the experimental values: Hanle effect (Fig. (a)) and femtosecond PFR technique (Fig. (b)).*

4.2 Experimental results

4.2.1 Samples description and characterization

The samples studied in this work consist of a 8-nm thick CdTe QW confined between CdMgTe barriers. They have been grown by G. Karczweski at the Sciences Academy of Warsaw by molecular beam epitaxy on a (100)-oriented GaAs substrate. The samples are doped with iodine donors placed in the central plane of the QW, with different nominal concentrations listed in table 4.1.

The originality of this system resides in the fact that the donors are placed in the middle of the QW, to increase the localization of the electron wave-function in comparison with bulk systems [12]. Figure 4.2 shows a scheme of the studied samples.

Sample	Name	Doping concentration (donors/cm^{-2})
A	052807C	1×10^{9}
B	030104A	3.2×10^{10}
C	022504A	9.7×10^{10}
D	022404AB	1.6×10^{11}
E	022604A	2.9×10^{11}
F	022404BB	3.6×10^{11}

Table 4.1

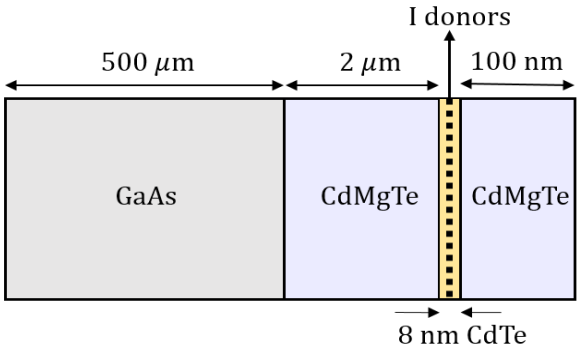

Figure 4.2 *Schematic representation of the structure of the studied samples.*

For the characterization of the samples, the experimental arrangement shown in Fig. 2.6 of Chapter 2 has been adapted to perform photoluminescence (PL) measurements: In the axis of detection, a movable mirror has been placed to send the photoluminescence emitted by the sample to a double monochromator Acton SP2750 and a Pylon camera. We used a He-Ne laser of 633 nm as excitation light, well above the energy band gap of the sample.

Figure 4.3 shows the PL spectra of the six studied samples obtained at the temperature $T = 10$ K.

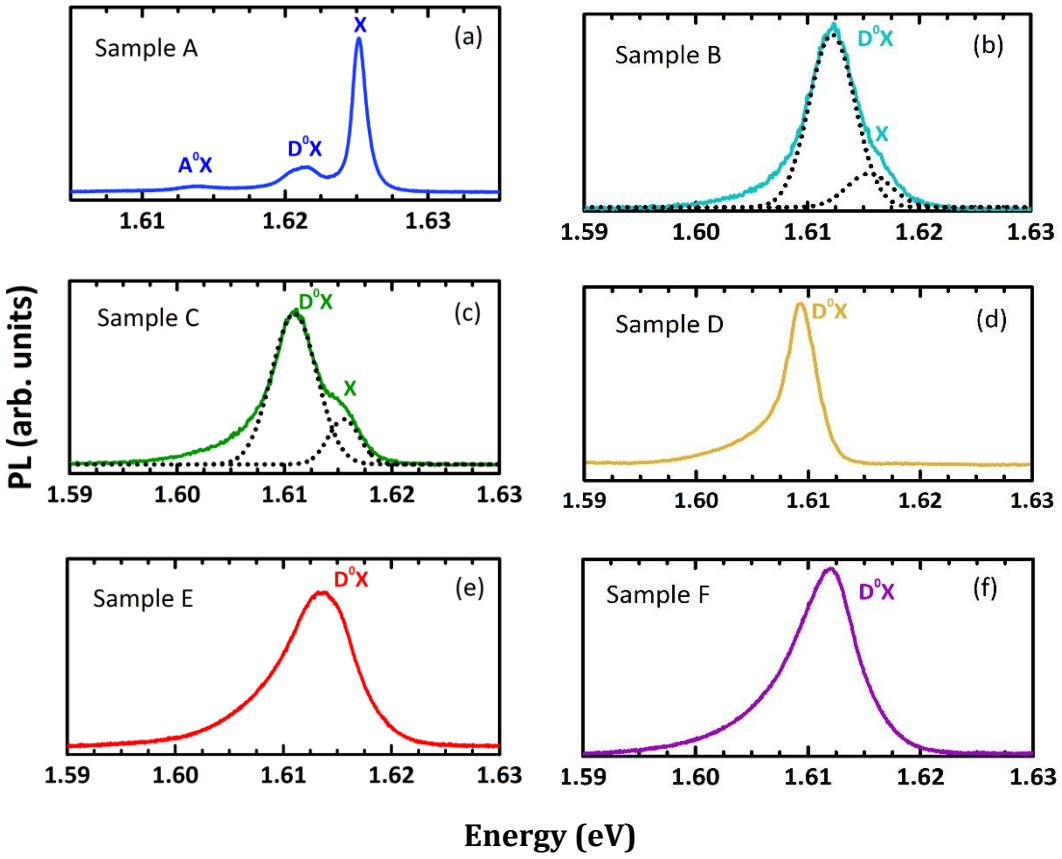

Figure 4.3 *PL spectra of the six studied samples, obtained at T = 2 K for sample D and T = 10 K for samples A, B, C, E and F.*

In a PL spectrum, it is possible to identify the luminescence of excitons, and of excitons bound to neutral impurities (donors and acceptors). For the intentionally undoped sample A, the free-exciton emission at 1.625 eV (denoted as X) dominates the PL spectrum, at it is shown in Fig. 4.3 (a). A residual concentration of donors in this sample is revealed by a second peak at 1.621 eV, associated with the donor-bound exciton transition (D^0X). The energy difference between the free-exciton peak and the D^0X one, gives the exciton binding energy ≈ 4 meV in the D^0X complex. The shoulder at lower energy is associated to the formation of excitons bound to neutral acceptors (A^0X); indeed, the introduction of donor impurities in the QW creates compensation sites, inducing the presence of acceptor sites which in our case are probably cadmium vacancies.

As we can see in Fig. 4.3, in the intentionally doped samples, the D^0X luminescence is more intense than the X one. For the intermediate doping concentrations, samples B and C (see Figs. 4.3 (b) and (c)), a shoulder associated with the exciton transition at 1.615 eV is still visible in the high-energy part of the D^0X broad band. At higher donor concentration, only a broad peak associated with the D^0X transition is visible (see Figs. 4.3 (d), (e), (f)).

When comparing Figs. 4.3 (a) and 4.3 (c), we underline that the energy of the X transition is slightly different; this is because of the Mg content in the barrier: for sample A, the Mg content is 18 %, while it is 11% for sample C (and also for the other samples).

The full width at half maximum of the D^0X PL band increases with the increasing donor concentration, from 2.6 meV for sample A to 6.2 meV for sample E. The exciton PL band

also broadens, weakens and finally vanishes when the donor concentration increases. We remark that the PL spectrum of sample D was taken at lower temperature (T = 2K) and at different intensity of excitation, which explains the different full width at half maximum of the D^0X PL band.

In order to perform transmission measurements, the GaAs substrate in the samples has been removed by chemical attack.

4.2.2 Photo-induced Faraday rotation signal at different magnetic fields

Figure 4.4 shows the PFR signal obtained at low temperature, T = 2 K, in presence of a transverse magnetic field of 0.5 T (Voigt geometry) for the six studied samples. The common pump and probe energy is always tuned to the D^0X transition in order to create mainly donor-bound exciton complexes, and to probe the D^0X optical transition, since the band-width of the used mode-locked Ti:Sapphire laser is less than 1 meV. The focus spot area is $(90\ \mu m)^2$ and the energy fluence of the pump pulses is 0.09 $\mu J\ cm^{-2}$. For all the samples, an oscillatory signal with an envelope time larger than the lifetime of the D^0X complex T_R (~ 200 ps Ref. [10]) is observed. This long-lasting signal is the signature of the spin polarization of electrons bound to neutral donors D^0. The mechanism involved in the creation of this electron polarization has been introduced in chapter 1.

.

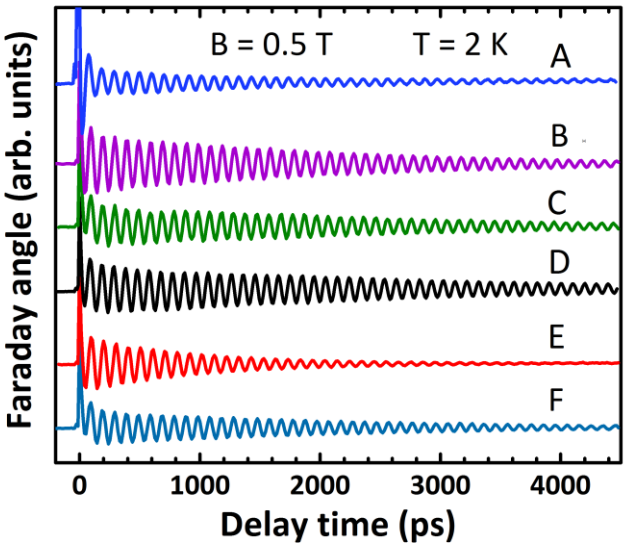

Figure 4.4 *PFR signals as a function of the pump-probe delay for samples A-F. The PFR signals were obtained at T = 2 K, B = 0.5 T, using the following optical energies: (A) 1.622 eV, (B) 1.613 eV, (C) 1.611 eV, (D) 1.615 eV, (E) 1.617 eV, and (F) 1.612 eV.*

As we have seen in chapter 1, the electronic spin dynamics of D^0 is described by the equation [13]:

$$\frac{d\vec{S}_\perp}{dt} = \vec{\Omega}_e \wedge \vec{S}_\perp - \frac{\vec{S}_\perp}{T_2^*} + \frac{J(t)}{T_R}\vec{e}_z, \qquad (4.1)$$

where $\vec{S}_\perp$ is the transverse component (to the magnetic field) of the electronic spin, $\vec{\Omega}_e$ is the Larmor precession vector of the electrons, T_2^* the spin dephasing time of the ensemble of electronic spins, and $J(t) = J_0 e^{-t/\tau}$ is one third of the average kinetic momentum of the ensemble of D^0X complexes; τ is the decay time of the difference between the $D^0X_{+3/2}$ and $D^0X_{-3/2}$ populations. For times much larger than τ, the solution of Eq. (4.1) is

$$S_z(t) = A_3 e^{-\frac{t}{T_2^*}} \cos(\Omega_e t), \tag{4.2}$$

and for times of the order of τ, the next expression fits the PFR signal:

$$PFR(t) = A_1 e^{-t/\tau} + A_2 e^{-t/T_x} \cos(\Omega_x t) + A_3 e^{-t/T_2^*} \cos(\Omega_e t), \tag{4.3}$$

with Ω_i the Larmor frequency associated to the carriers:

$$\Omega_i = \frac{g_i^\perp \mu_B}{\hbar} B, \tag{4.4}$$

where μ_B is the Bohr magneton, $\hbar$ the reduced Planck constant, and $g_i^\perp$ the transverse Landé factor of carrier i (i = e, h, x; electron, hole and exciton, respectively). For holes the Landé factor $g_h^\perp$ is almost zero in a 8-nm CdTe QW [12], so the field induces a spin precession of the resident electrons bound to the donors, but not of the D^0X complex since the D^0X complex contributes to the spin dynamics by its hole.

The first non-oscillatory term of eq. (4.3) represents the contribution of the D^0X complex to the PFR signal. It is clearly seen in Fig. 4.4, especially in samples with high concentrations of donors (see Fig. 4.4, curves C-F). When the sample contains a low concentration of donors it is possible to observe another additional oscillatory component of the PFR signal (second term of eq. 4.3), having a frequency Ω_x similar to the electron one and with a very short damping time T_x (see Fig. 4.4, curve A). This additional component corresponds to the oriented exciton spins.

Figures 4.5(a)-4.10(a) show the PFR signal at different magnetic fields obtained for each sample. For low magnetic fields, the oscillatory behavior of the PFR signal is also observed at negative delays. This means that the damping time of the oscillations is comparable to the repetition period 13.2 ns of the laser, and this damping time decreases for increasing magnetic fields.

We have fitted expression (4.3) to all the PFR curves. Figs. 4.5(b)-4.10(b) show the dependence of the Larmor frequency Ω_e on the applied magnetic field. A linear fit of the data gives the corresponding value of $g_e^\perp$ for each concentration. Figures 4.5(c)-4.10(c) show the other fitting parameter, $1/T_2^*$, as a function of the magnetic field, which is proportional to the magnetic field due to the inhomogeneities of the $g_e^\perp$ values, as it is shown below. As we have seen in chapter 1, assuming a Lorentzian distribution of $g_e^\perp$ factors, the experimentally determined T_2^* is related to the zero-field decoherence time $T_2(0)$ as follows:

$$\frac{1}{T_2^*} = \frac{1}{T_2(0)} + \Delta g_e^\perp \frac{\mu_B}{\hbar} B. \tag{4.5}$$

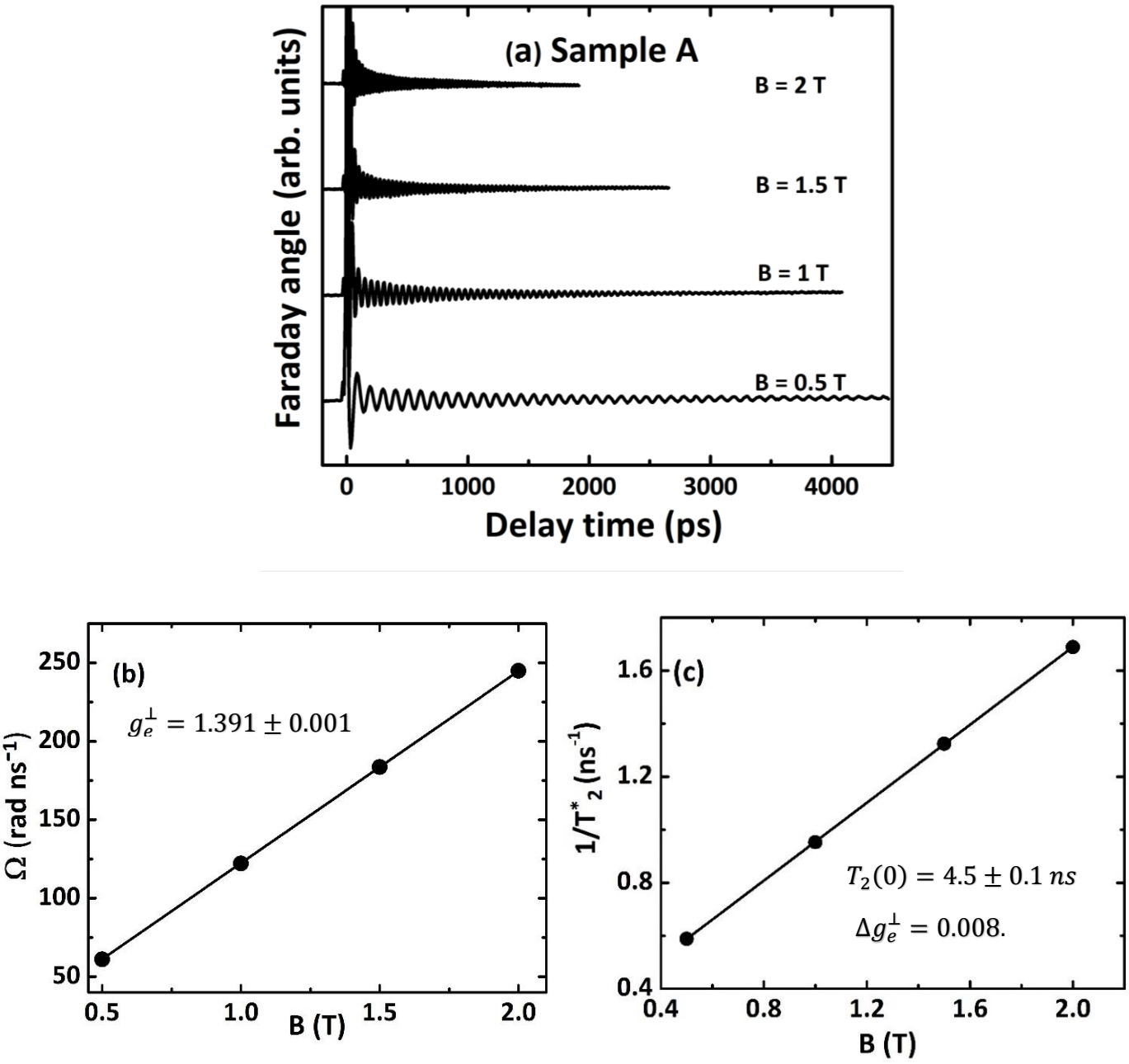

Figure 4.5 *(a) PFR signals for sample A as a function of the pump-probe delay, obtained at T = 2 K for several values of the transverse magnetic field. The PFR curves are vertically shifted for clarity. (b) Experimental data of the D^0 Larmor frequency. A linear fit to Eq.(4.4) leads to the value $g_e^{\perp} = 1.391 \pm 0.001$. (c) Inverse of the spin decoherence time T_2^*. A linear fit according to Eq. (4.5) leads to $T_2(0) = 4.5 \pm 0.1\ ns$ and $\Delta g_e^{\perp} = 0.008$.*

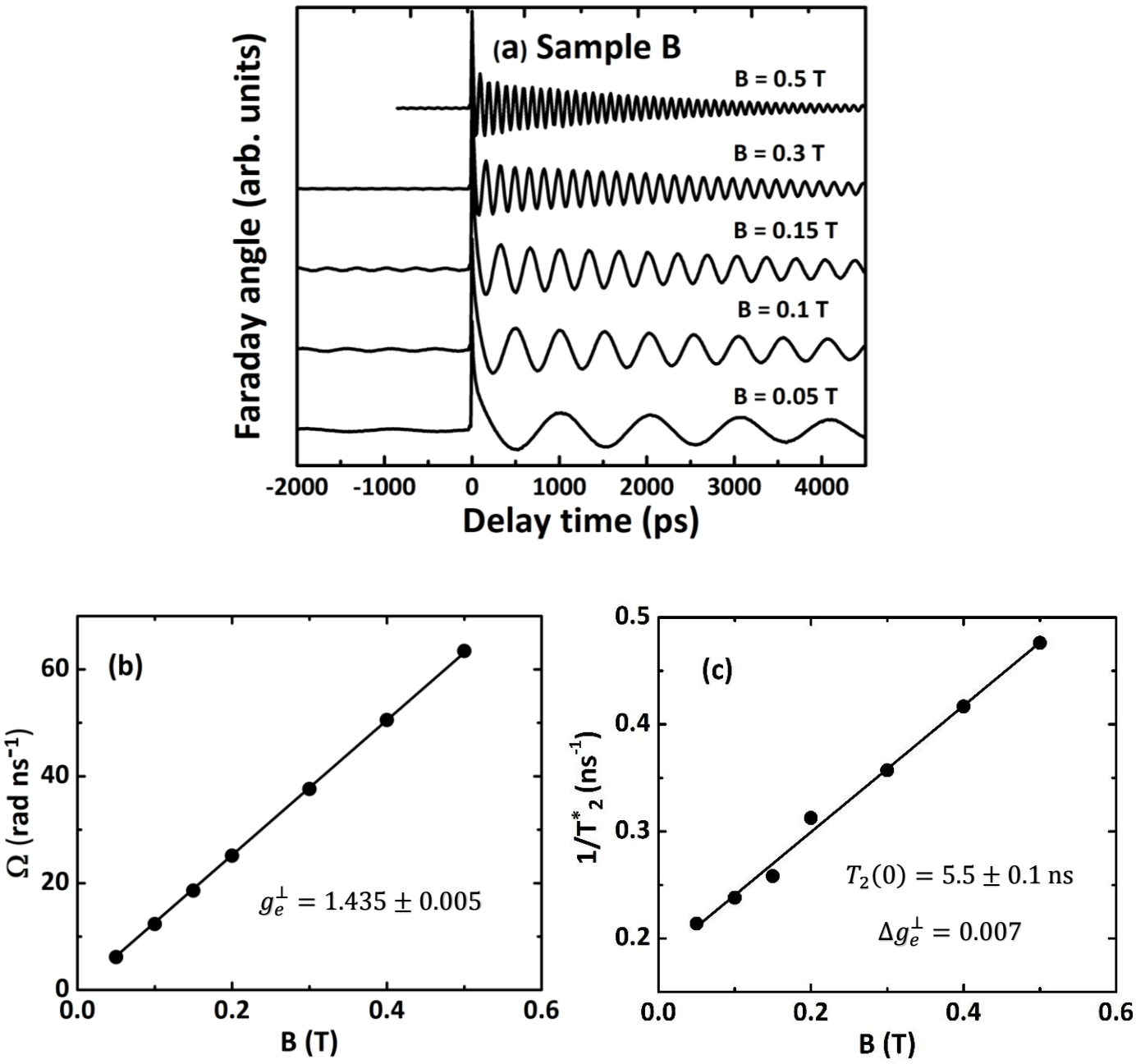

Figure 4.6 *(a) PFR signals for sample B as a function of the pump-probe delay, obtained at T = 2 K for several values of the transverse magnetic field. The PFR curves are vertically shifted for clarity. (b) Experimental data of the D^0 Larmor frequency. A linear fit to Eq.(4.4) leads to the value $g_e^{\perp} = 1.435 + 0.005$. (c) Inverse of the spin decoherence time T_2^*. A linear fit according to Eq. (4.5) leads to $T_2(0) = 5.5 \pm 0.1$ ns and $\Delta g_e^{\perp} = 0.007$*

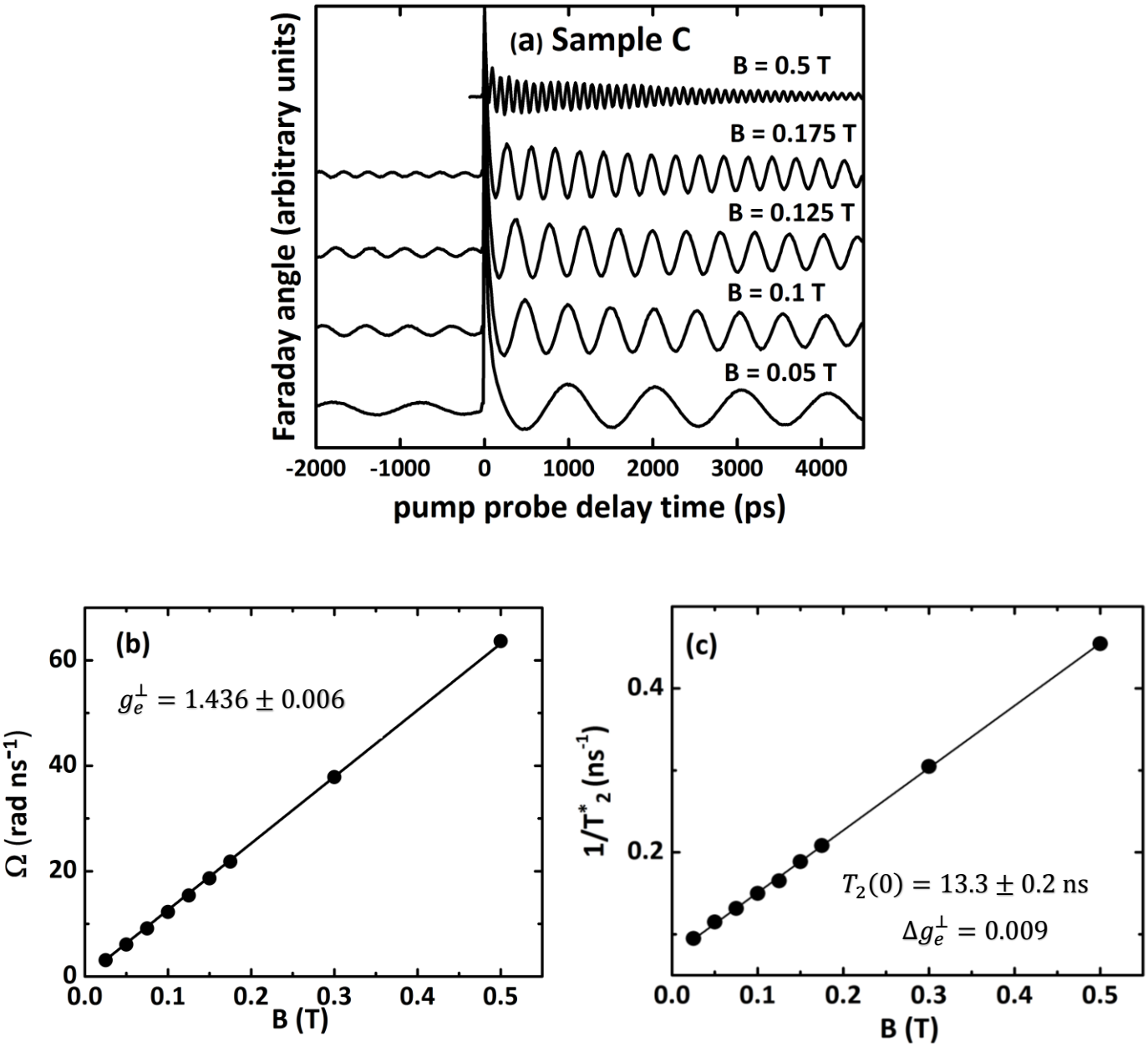

Figure 4.7 *(a) PFR signal for sample C as function of the pump-probe delay, obtained at T = 2 K for several values of the transverse magnetic field. The PFR curves are vertically shifted for clarity. (b) Experimental data of the D^0 Larmor frequency. A linear fit to Eq. (4.4) leads to the value* $g_e^{\perp} = 1.436 \pm 0.006$ *. (c) Inverse of the spin decoherence time* T_2^**. A linear fit according to eq. (4.5) leads to* $T_2(0) = 13.3 \pm 0.2$ *ns and* $\Delta g_e^{\perp} = 0.009$

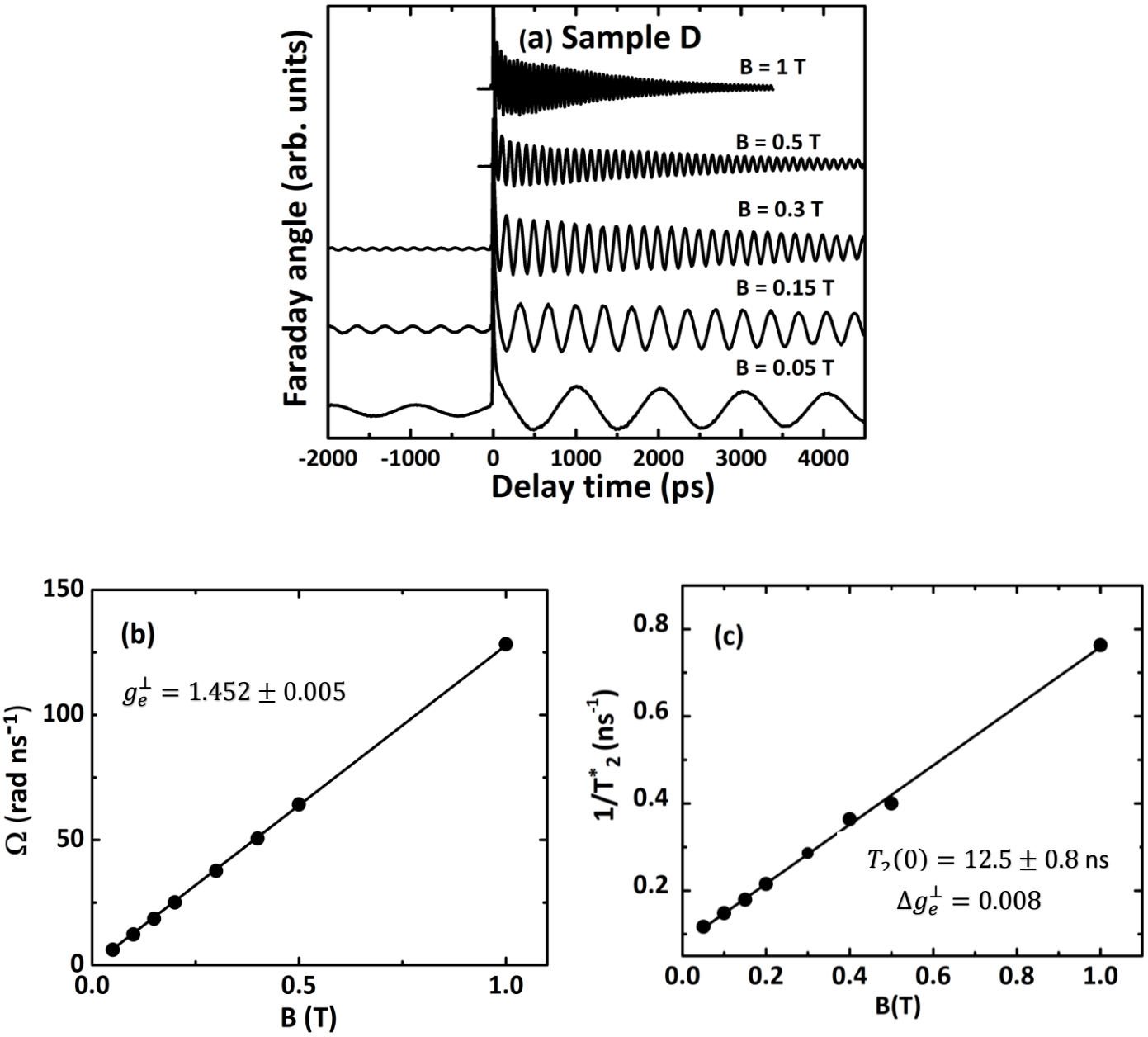

Figure 4.8 *(a) PFR signal for sample D as function of the pump-probe delay, obtained at T = 2 K for several values of the transverse magnetic field. The PFR curves are vertically shifted for clarity. (b) Experimental data of the D⁰ Larmor frequency. A linear fit to Eq. (4.4) leads to the value* $g_e^{\perp} = 1.452 \pm 0.005$*. (c) Inverse of the spin decoherence time* T_2^**. A linear fit according to eq. (4.5) leads to* $T_2(0) = 12.5 \pm 0.8$ *ns and* $\Delta g_e^{\perp} = 0.008$*.*

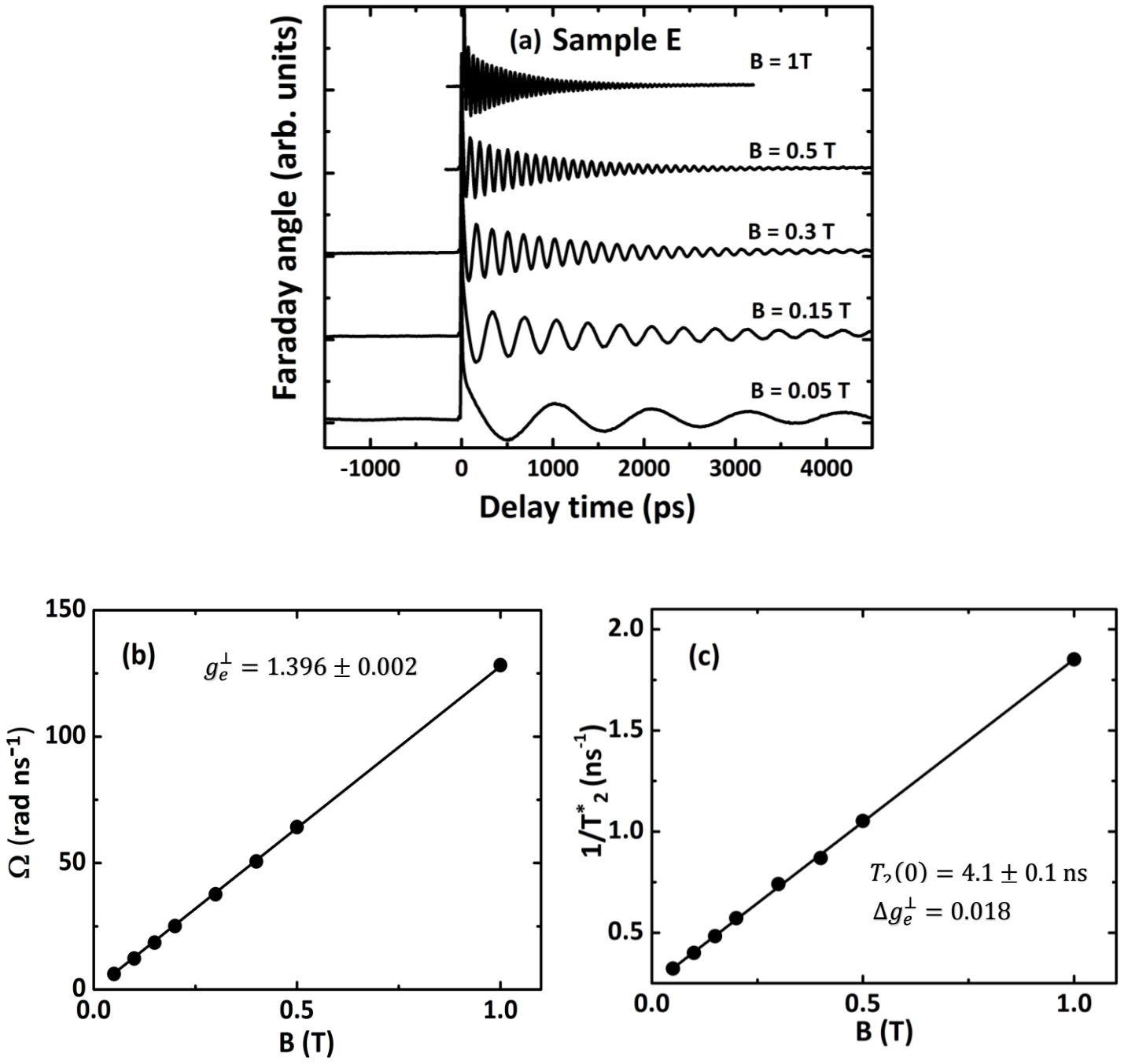

Figure 4.9 *(a) PFR signal for sample E as function of the pump-probe delay, obtained at T = 2 K for several values of the transverse magnetic field. The PFR curves are vertically shifted for clarity. (b) Experimental data of the D⁰ Larmor frequency. A linear fit to Eq. (4.4) leads to the value* $g_e^{\perp} = 1.396 \pm 0.002$*. (c) Inverse of the spin decoherence time* T_2^**. A linear fit according to eq. (4.5) leads to* $T_2(0) = 4.1 \pm 0.1$ *ns and* $\Delta g_e^{\perp} = 0.018$*.*

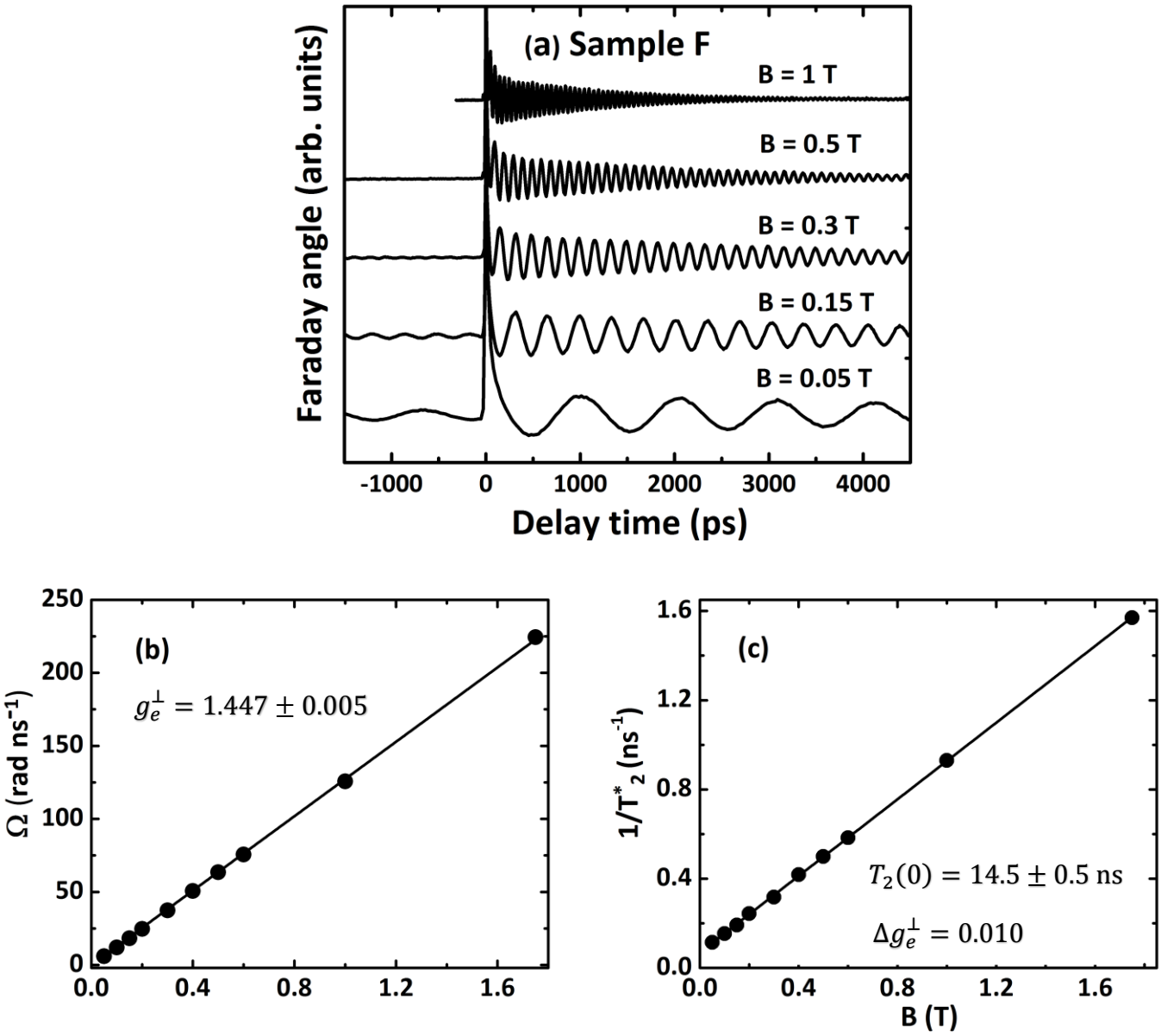

Figure 4.10 *(a) PFR signal for sample F as function of the pump-probe delay, obtained at T = 2 K for several values of the transverse magnetic field. The PFR curves are vertically shifted for clarity. (b) Experimental data of the D^0 Larmor frequency. A linear fit to Eq. (4.4) leads to the value $g_e^{\perp} = 1.447 \pm 0.005$. (c) Inverse of the spin decoherence time T_2^*. A linear fit according to eq. (4.5) leads to $T_2(0) = 14.5 \pm 0.5$ ns and $\Delta g_e^{\perp} = 0.010$.*

The linear fit of the expression (4.5) to the spin dephasing rates $1/T_2^*$, shown in Fig. 4.5 (c)-4.10 (c), are listed in Table 4.2:

Sample	$\mathbf{1/T_2^*}$ **(1/ns)**	$\boldsymbol{T_2(0)}$ **(ns)**	$\Delta g_e^{\perp}$
A	$\frac{1}{T_2^*} = 0.220 + 0.735B$	4.5 ± 0.1	0.008
B	$\frac{1}{T_2^*} = 0.181 + 0591B$	5.5 ± 0.1	0.007
C	$\frac{1}{T_2^*} = 0.075 + 0.760B$	13.3 ± 0.2	0.009
D	$\frac{1}{T_2^*} = 0.080 + 0.678B$	12.5 ± 0.8	0.008
E	$\frac{1}{T_2^*} = 0.243 + 1.6B$	4.1 ± 0.1	0.018
F	$\frac{1}{T_2^*} = 0.069 + 0.857B$	14.5 ± 0.5	0.010

Table 4.2 *Linear fit for $1/T_2^*$ according to Eq. (4.5) for each sample. (In the second column, the unit of B is the tesla.) $T_2(0)$ is also denoted τ_s in the following.*

Figure 4.11 shows an example of the fit of the equation (4.3) to the PFR signals at B = 0.5 T for each of the samples. The extracted time T_2^* is reported in each case.

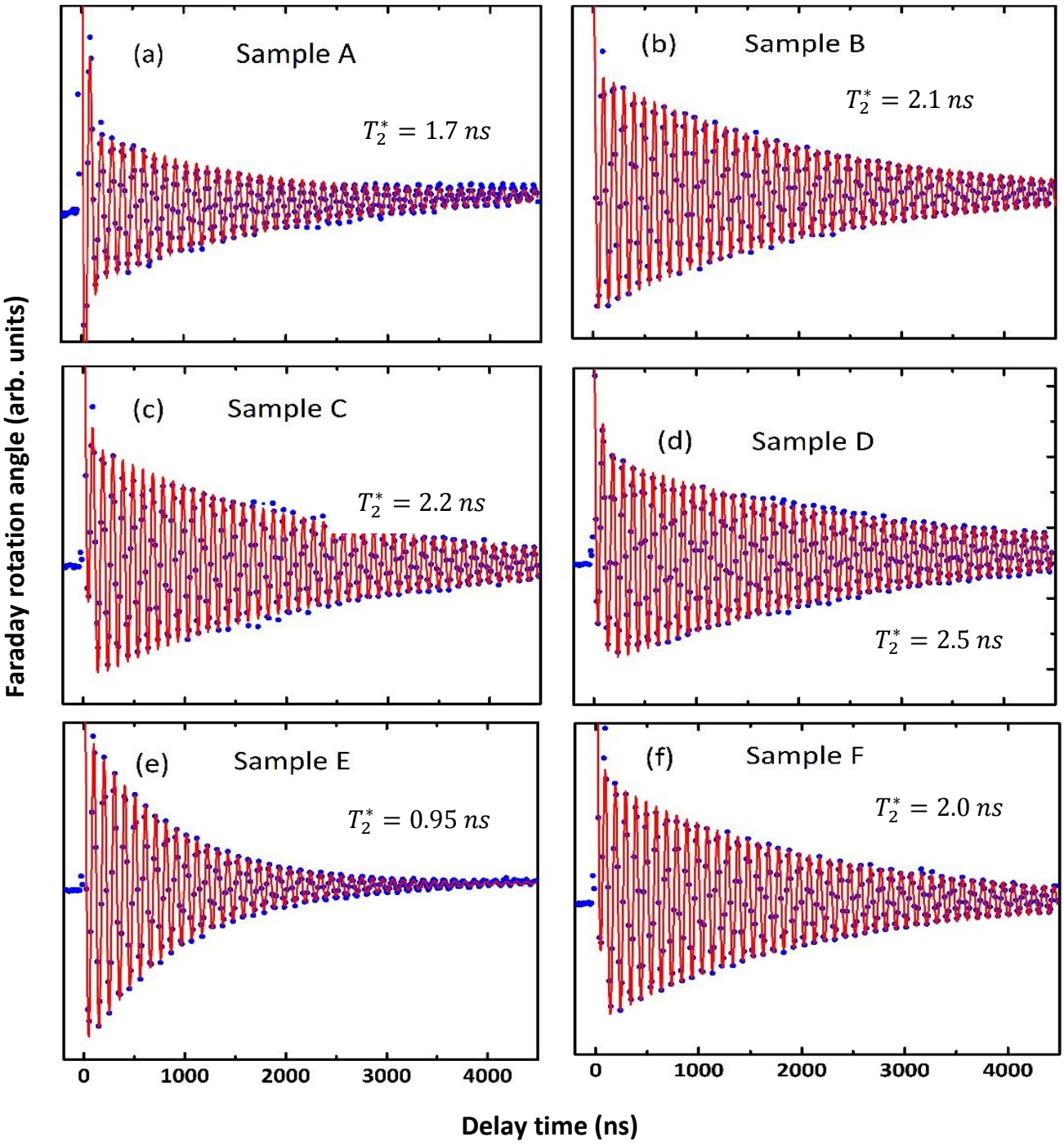

Figure 4.11 *PFR signals (blue points) obtained at B = 0.5 T and T = 2 K, for samples A to F. The red solid lines are fits of the expression (4.3) to the experimental data.*

The characteristic time τ of the D^0X complex, extracted from the fits is equal to 60 ps. and does not change very much as a function of magnetic field or doping concentration. This time contains two contributions: the recombination rate of D^0X and the hole spin flip rate in D^0X state. The lifetime of D^0X has been measured in a previous publication for a sample containing approximately 10^{11} cm^{-2} [14]. We have no information about the evolution of the D^0X lifetime with the doping concentration, and then we cannot draw a conclusion about the spin flip rate dependence on the doping concentration of the D^0X complex.

The spin dephasing time T_x, and precession frequency Ω_x of the oriented exiton spins extracted from the fit of sample A in Fig. 4.11 (a), are equal to 40 ps and 63 rad.ns^{-1}, respectively. Ω_X is close to Ω_e at the same magnetic field (see Fig. 4.5 (a)).

The metal-insulator transition in 3D materials has been calculated to appear for donor distances around 3 times the Bohr radius [15]; with this criterion, samples A-E are in the insulator regime, and sample F is in the metallic regime. We underline that the PFR signals are longer lasting for sample F than for sample E (see Figs. 4.9(a) and 4.10(a)), and as a consequence, we find a $\tau_s = T_2(0)$ much longer for sample F than for sample E. This peculiarity was also observed in bulk GaAs [1].

Figure 4.12(a) shows the spin relaxation time measured in samples A-F (full disks) and in one sample with the same characteristics and studied by using the same technique, Ref. [13], with a donor concentration of 1.2×10^{11} cm^{-2} (full diamond). The spin relaxation time versus concentration shows a non-monotonous behavior similar to the one found in bulk GaAs [1] and more recently in bulk CdTe [11]. The most remarkable feature of the dependence is a pronounced maximum of the relaxation time ($\sim$ 20 ns) at a donor concentration of about 1.2×10^{11} cm^{-2}. In bulk CdTe, there is a maximum (2.5 ns) that appears at the concentration of 5×10^{16} cm^{-3} [11], which corresponds approximately at a surface concentration of 1.4×10^{11} cm^{-2}. We also notice that for low doping concentrations in bulk CdTe, 1.5×10^{13} cm^{-3} ($\sim 1 \times 10^{9}$ cm^{-2}), Ref. [11] reported $\tau_s = 40$ ps, which is 100 times smaller than the spin relaxation time we measured in a 8-nm QW (4.5 ns). We underline that after the metal-insulator transition (see sample F, Fig. 4.12 (a)), another maximum of the spin relaxation time appears as in the studies performed in GaAs [1].

Figure 4.12(b) shows the dependence of the $g_e^{\perp}$ values on the doping concentration. We observe a correlation between the dependence of $g_e^{\perp}$ and τ_s on doping concentration. This has been already noticed in bulk CdTe [11], but the reason in not clear yet, and more studies are needed to elucidate this behavior.

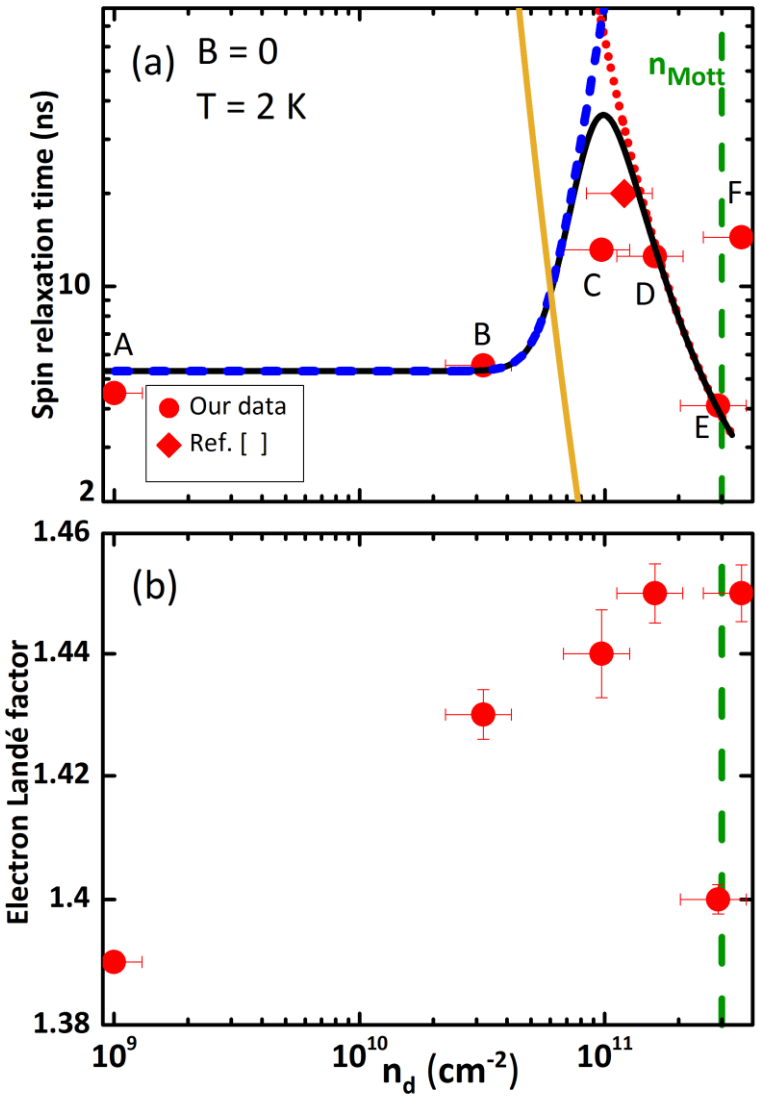

Figure 4.12 *(a)Measured spin relaxation times in samples A-F (full disks); the full diamond represents a measurement of Ref. [13]. The black solid line represents the spin relaxation time as a function of the doping concentration according to Eq. (4.17). The relaxation mechanisms for electrons bound to donors in the insulating regime and the correlation time are also represented: hyperfine interaction,* $T_{\Delta}^{e} + \tau_{sn}$ *, Eq. (4.9) and Eq. (4.11), (blue-dashed line), anisotropic exchange interaction, Eq. (4.13) (red-dotted line) and correlation time, Eq. (4.10) (solid-yellow line). (b) Transverse electron Landé factor* $g_{e}^{\perp}$ *as a function of the doping concentration (full disks).*

4.3 Spin relaxation mechanisms for donor-bound electrons in a semiconductor QW in the insulating regime at low temperature

In this section, we adapt the theory developed for bulk GaAs in Ref. [1] to a QW, in order to explain the spin relaxation time of donor-bound electrons placed in the middle of a QW at low temperature in the insulating regime. The dominant mechanisms for doping concentrations above the metal-insulator transition (sample F) will be not discussed in this chapter.

4.3.1 Hyperfine interaction

In the insulating regime at low doping concentrations, the localized electron spins relax via their interaction with the spins of the nuclei. A localized electron is coupled to many nuclear spins by the hyperfine interaction. The Hamiltonian of this interaction is given by the expression [14]

$$\widehat{H}_{hf} = \frac{v_0}{2}\sum_j A^j \left|\Psi(\vec{R}_j)\right|^2 \hat{S}_e.\hat{I}^j, \tag{4.6}$$

where v_0 is the volume of a unit cell, $\hat{S}_e$ and $\Psi(\vec{R}_j)$ are the spin and envelope wave function of the electron at the j-th nucleus, and A^j is written as

$$A^j = \left(\frac{16\pi\mu_B\mu_j}{3I_j}\right)\left|u_c(\vec{R}_j)\right|^2, \tag{4.7}$$

with μ_B the Bohr magneton, $\hat{I}^j$, μ_j and $\vec{R}_j$ the spin, magnetic moment and position of the j-th nucleus; and $u_c(\vec{R}_j)$, the Bloch function of the electron at the j-th nucleus. The sum in Eq. (4.6) goes over all the nuclei of the lattice.

The effective nuclear hyperfine magnetic field $\vec{B}_N$ acting on a localized electron spin is given by the expression

$$\vec{B}_N = \frac{v_0}{\mu_B g_e}\langle\sum_j A^j \left|\Psi(\vec{R}_j)\right|^2 \hat{I}^j \rangle_N, \tag{4.8}$$

where $\langle \dots \rangle_N$ denotes a quantum mechanical average over the ensemble of nuclear wave functions, and g_e is the electron Landé factor. For the time scale (of the order of nanoseconds) in which we are interested, we can suppose that the precession frequency of an electron in the hyperfine field of all nucleus is much greater than the precession frequency of a nucleus in the hyperfine field of the electron; thus each electron spin moves in a frozen fluctuation of the nuclear hyperfine magnetic field.

The temporal evolution of the spin polarization of an ensemble of localized electrons under this effective hyperfine nuclear magnetic field was described by Merkulov *et al*. [16]. The average spin polarization firstly drops down to 10 % of its initial value within a characteristic time $2T_\Delta^e$ and afterwards, it reaches a constant value of 1/3 of its initial value, keeping it during a time of the order of a microsecond [14]. T_Δ^e is given by the expression [14]

$$T_{\Delta}^{e} = \hbar\sqrt{\frac{3N_L}{2n\sum_i I_i(I_i+1)(A_i)^2 P_i}}, \tag{4.9}$$

where A_i are the hyperfine constants, I_i the nuclear spin quantum numbers, $\mathrm{P_i}$ the abundance of the nuclear species, n is the number of nuclei inside a unit cell, and $\mathrm{N_L}$ the number of nuclei within the wave-function envelope of an electron. The sum runs over all nuclei of the crystal basis and for each nucleus over its non-vanishing nuclear spin. For CdTe, a unit cell contains one Cd and one Te atom. The stable isotopes of cadmium and tellurium with nonzero nuclear spin are Cd^{111}, Cd^{113}, Te^{123} and Te^{125}; they all have a nuclear spin $\mathrm{I} = 1/2$. Both Cd isotopes have almost the same hyperfine constant, $\mathrm{A_{Cd}} = 31$ μeV, and they have together a natural abundance of $\mathrm{P_{Cd}} = 25$ %. The hyperfine constant of Te^{123} and Te^{125} is $\mathrm{A_{Te}} = -45$ μeV [17], and they have an abundance of $\mathrm{P_{Te}} = 8$ %. To calculate $\mathrm{N_L} = 2\mathrm{V_L}/\Omega$ with Ω the volume of a unit cell and $\mathrm{V_L}$ the effective volume defined as $[\int|\Psi(\vec{r})|^4\, d^3r]^{-1}$ [16], we take $\Psi(\vec{r})$ as a modified hydrogenic envelope wave-function for the electron in a finite QW of thickness L (see section 1.4.2 of chapter 1). We took an effective mass $m_e^* = 0.11\mathrm{m_0}$ [18] and a dielectric constant of $\varepsilon_r = 10.2$ [19]. Then, a variational calculation allows us to obtain for L = 8 nm, $T_{\Delta}^{e} =$ 5.6 ns, with a barrier Mg concentration x_{Mg} = 11 %. (Note that for sample A, x_{Mg} = 18 % , leading to a higher QW confinement and $T_{\Delta}^{e} = 5.3$ ns.) We underline that the experimental value $\tau_s = T_2(0)$ obtained in sample A is very close to this estimation: it is confirmed that the spin relaxation time for sample A is mostly limited by the hyperfine interaction.

4.3.2 Correlation time and hyperfine interaction

As the distance between the donors decreases with the increase of the doping concentration (samples B and C in Fig. 4.12 (a)), the electron wave functions begin to overlap and the electronic spin jumps between two donor sites. The exchange energy *2J* (chapter 3) allows to estimate the degree of localization of an electron on a donor site and to introduce the concept of correlation time. The correlation time τ_c is defined as the residence time of the electron spin on a fixed donor site:

$$\tau_c \approx \frac{\hbar}{\xi J(r_c)}, \tag{4.10}$$

with r_c the average characteristic distance between interacting donors: $\mathrm{r_c} = \mathrm{b}(\mathrm{n_{2D}})^{-1/2}$ or $\mathrm{r_c} = \mathrm{b}(\mathrm{n_{3D}})^{-1/3}$ in 2D and 3D respectively, and b and ξ numerical factors of the order of unity. *b* is expected to be between 0.54 and 0.8, and a value of $\xi = 0.8$ has been taken in bulk GaAs performing the fit of experimental data [1][1].

[1]In the limit of low doping concentrations, only nearest neighbors contribute to the exchange interaction: the distribution function of the distance to the nearest neighbor has a maximum at $\mathrm{r_c} = 0.54(\mathrm{n_{3D}})^{-1/3}$. At higher doping concentrations, second nearest neighbors also contribute to the interaction, $\mathrm{r_c} = 0.8(\mathrm{n_{3D}})^{-1/3}$. Therefore, one expects b between 0.54 and 0.8.

Both concepts, exchange energy and correlation time, are represented in Fig. 4.13(a): an electron spin S precesses around a nuclear magnetic field $B_{N,A}$ at the donor site A, during an average time τ_c before a jump to the donor site B.

Due to the overlapping of the electron wave-functions, the electron spin ceases to be bound to a single donor and interacts with a greater number of nuclei; as a result, the effect of nuclear-spin fluctuations becomes smaller. At each tunnel jump, the spin of the electron changes of nuclear environment, Fig 4.13 (b), and starts a precession around a new magnetic field $B_{N,B}$. The spin relaxation time τ_{sn} in this regime is given by [20]

$$\frac{1}{\tau_{sn}} = \frac{2}{3}\frac{\tau_c}{(T_\Delta^e)^2}\,. \qquad (4.11)$$

In our case, we consider the exchange energy $2J(r)$ of a pair of donors inside an infinite CdTe QW of thickness L' calculated in chapter 3 (Eq. 3.27) [21]:

$$2J(r) = 2J_0 E_{\mathrm{h}}^{*3\mathrm{D}}[1 + (AR)^2]^{\frac{\beta}{2}} \exp[-\gamma \mathrm{R} - \beta A \mathrm{R}\ \mathrm{arctg}\ (AR)],$$

with $\mathrm{R} = \mathrm{r}/\mathrm{a}_{\mathrm{B}}^{*3\mathrm{D}}$, r the distance between donors, $a_B^{*3D} = 4.91$ nm the bulk Bohr radius, $E_h^{*3D} = 29$ meV the Hartree energy, and $2J_0 = 1.34$ the splitting energy in E_h^{*3D} units between the ground state and the first excited state of a "helium atom" in a CdTe QW of thickness L' = 8 nm (see appendix C). The parameters A = 0.71, $\beta = 1.8$ and $\gamma = 0.23$ are extracted from an interpolation method between $2J_0$ and the exchange energy $2J(r \gg 1)$ at large distances between the donors in an infinite QW (see chapter 3).

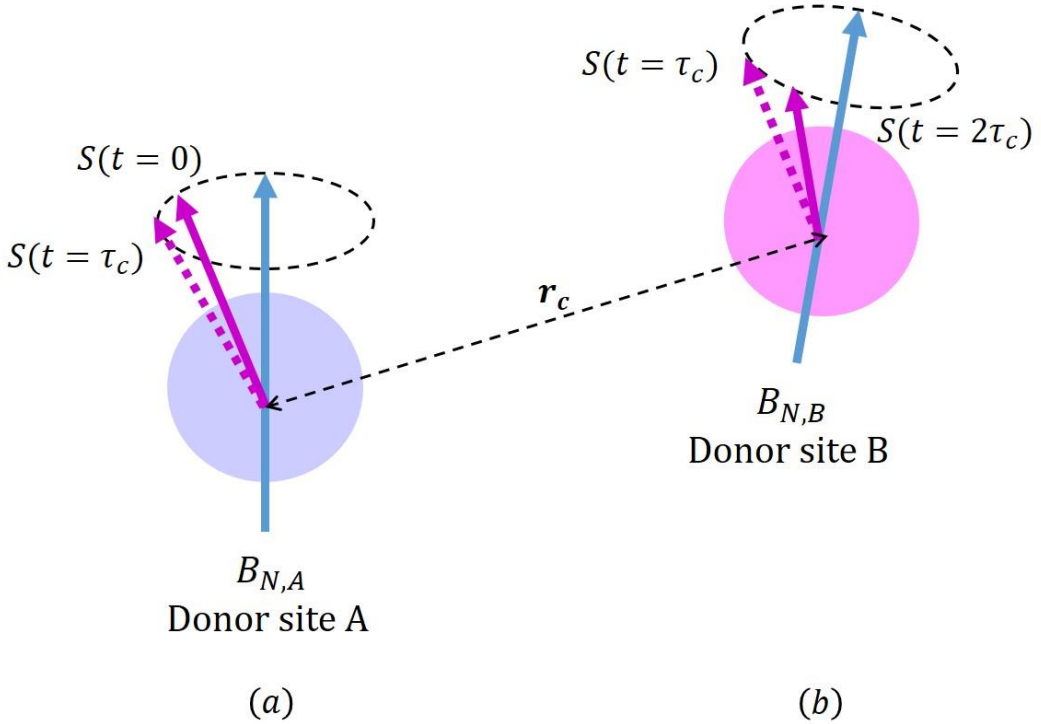

***Figure 4.13**. Schematic representation of the concepts of correlation time and exchange energy for an electron spin.*

4.3.3. Anisotropic exchange interaction

When the spin-orbit interaction in semiconductors is taken into account, it results in an anisotropic contribution into the exchange Hamiltonian of a pair of localized electrons. The anisotropic exchange interaction exists in semiconductor structures that are not symmetric with respect to spatial inversion, for instance in zinc-blende semiconductors.

This mechanism can be understood in the following way. When one of the two electron spins (S_1 and S_2) localized at centers A and B (Fig. 4.14 (a)) tunnels to the adjacent localization center, it experiences an influence of the spin-orbit field resulted from the under-barrier motion of the electron. This field causes a rotation of the electron spin through a small angle θ; at the same time, the tunneling of the second electron to the first-electron position, is accompanied by the rotation of its spin through the same angle, but in the opposite direction (Fig. 4.14 (b)). The exchange interaction couples the spins $\vec{S}'_1$, $\vec{S}'_2$ rather than the genuine spins $\vec{S}_1, \vec{S}_2$ at the centers A and B. This leads to the following expression for the exchange Hamiltonian in a semiconductor heterostructure [22]:

$$\begin{aligned}\widehat{H}_{exc} &= 2J\vec{S}_1'.\vec{S}_2' \\ &= 2J[\vec{S}_1.\vec{S}_2\cos\theta + (\vec{d}.\vec{S}_1)(\vec{d}.\vec{S}_2)(1-\cos\theta) + \vec{d}.(\vec{S}_1\times\vec{S}_2)\sin\theta],\end{aligned} \qquad (4.12)$$

where $\vec{d}$ is a unit vector depending on the crystallographic structure.

The first term in eq. (4.12) is the usual scalar interaction, the second term corresponds to the pseudo-dipole interaction, and the third one is the Dzyaloshinskii-Moriya (DM) interaction. The magnitude of θ characterizes the strength of the anisotropic part; for small θ, the anisotropic part is dominated by the DM term.

The first isotropic term of expression (4.12) preserves the total spin of the two electrons; for this reason, it does not cause spin relaxation. The spin relaxation time for localized electrons near the insulator-metal transition, in the insulating phase, is fixed by the anisotropic part of the exchange Hamiltonian. The expression for the spin relaxation time in a QW of thickness L' is then given by [1]

$$\frac{1}{\tau_{sa}} = \frac{2}{3}\frac{\theta^2}{\tau_c}. \qquad (4.13)$$

In general, for a QW, θ can be written for both zinc-blende and wurzite structures as

$$\theta = \frac{2\gamma_e b}{E_h^* a_B^{*2}}\langle k_z^2\rangle\, r, \qquad (4.14)$$

with b a parameter equal to 1 or 4 for zinc-blende or wurtzite crystals, respectively, $\langle k_z^2\rangle$ the average value of the squared z-component of the electron wave vector, and γ_e the splitting coefficient related to the Dresselhaus term of the spin-orbit Hamiltonian [23,24]. In the zinc-blende structure, this coefficient γ_e^{ZB} is proportional to the spin-orbit constant α_{so}:

$$\gamma_e^{ZB} = \frac{\alpha_{so}\hbar^3}{m_e^*\sqrt{2m_e^*E_g}}. \tag{4.15}$$

The substitution of Eq. (4.15) in Eq. (4.14) leads to the expression proposed in Ref. [25] for θ^{ZB}:

$$\theta^{ZB} = \frac{2\alpha_{so}\hbar}{\sqrt{2m_e^*E_g}}\langle k_z^2\rangle r. \tag{4.16}$$

For a wurzite crystal, the expression for γ_e^W and values for specific materials can be found in Refs. [23,26].

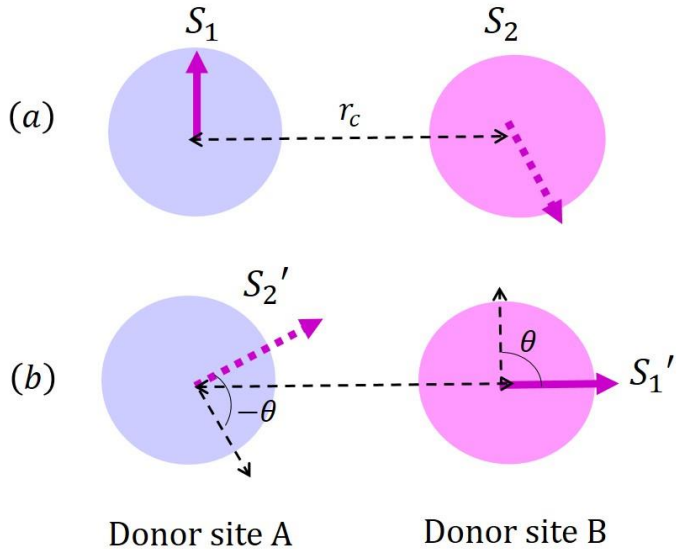

Figure 4.14 *Schematic representation of the anisotropic exchange interaction mechanism acting on spins S_1 and S_2. The black dashed arrows in (b) represent the directions that S'_1 and S'_2 spins would have after jumps due only to the isotropic exchange.*

4.4 Fitting of the experimental results and determination of the spin-orbit constant in CdTe

The solid line in Fig. 4.12(a) represents a fit of the experimental data to the theoretical relaxation time of donor-bound electrons at low temperature, in the insulating regime, taking into account the hyperfine and anisotropic exchange interactions:

$$\tau_s = \left(\frac{1}{\tau_{sn}+T_\Delta^e} + \frac{1}{\tau_{sa}}\right)^{-1}, \tag{4.17}$$

with T_Δ^e , τ_{sn} and τ_{sa} given by the expressions (4.9), (4.11) and (4.13). The model (4.17) agrees with the experimental data using reasonable values of the parameters: $T_\Delta^e =$ 5.3 ns, b $= 0.8, \xi = 0.1,$ and $\theta = (0.022 \pm 0.003)\frac{r}{a_B^{*3D}}$.

From the pre-factor found in the expression of θ, it is possible to deduce, using Eq. (4.16), a range of values for the spin-orbit constant α_{so} in CdTe. We obtain finally $\alpha_{SO} = 0.079 \pm 0.011$, taking E_g= 1.606 eV and $\langle k_z^2 \rangle = 6.1 \times 10^{-2}\text{nm}^{-2}$ calculated using a hydrogenic wave-function inside a finite QW of thickness L' = 8 nm [see section (1.4.2) of chapter 1]. This value for α_{so} is close to the one which can be extracted from the theoretical values reported in the literature for the spin splitting of the Γ_6 conduction band in CdTe: $\gamma_c = 11.75$ eV Å^3 [27] and $\gamma_c = 8.5$ eV Å^3[26]; Using the relation [27]

$$\alpha_{so} = \frac{2\gamma_c}{\hbar^3}\sqrt{2m_e^{*3}E_g}, \tag{4.18}$$

one obtains $\alpha_{so} = 0.073$ and $\alpha_{SO} = 0.053$, respectively.

4.5 Discussion of the results

4.5.1 Quantum well vs bulk

Now, we use our experimental value of the spin-orbit constant, $\alpha_{so} = 0.079,$ to plot in Fig. 4.15 the predicted spin relaxation time in bulk CdTe [solid line in Fig. 4.15], and make a comparison with the available experimental values. We have used Eq. (4.17) and the corresponding expressions for θ and J in 3D [15,26], taking b = 0.7 and $\xi = 0.8$, values that are in the range proposed by Ref. [1]. The hyperfine dephasing time T_Δ^e in bulk is calculated following Eq. (4.9) using a hydrogenic wave-function $\Psi(\vec{r}) = \frac{1}{\sqrt{\pi}a_B^{3/2}}e^{-r/a_B^{*3D}}$ for the effective volume $V_L = [\int |\Psi(\vec{r})|^4\, d\vec{r}]^{-1}$, which gives $V_L = 8\pi a_B^{*3D}$ (solid line in Fig. 4.15).

Using the volume of a sphere of radius equal to the effective bulk Bohr radius $V_L = 4\pi a_B^{*3D}/3$ (dashed line in Fig. 4.15), the predicted spin relaxation times is diminished, except near the MIT. Due to the quadratic dependence on T_Δ^e of τ_{sn}, the difference of approximately 80 % between the square of the two calculated values for T_Δ^e in GaAs and CdTe, produces a considerable difference for the maximum spin relaxation time predicted by the theory, for both bulk materials.

We note that the theoretical spin relaxation times in bulk CdTe are longer than the relaxation times measured in a 8-nm CdTe QW (Fig. 4.12 (a)). In general, in the low-doping regime (large R), T_{Δ}^{e} in a QW is slightly smaller than in bulk, since the localization of the electron wave-function is increased. Also, the electron exchange energy, 2J, is smaller (see Fig. 3.7(a) of chapter 3), therefore a shorter spin relaxation time in this regime is expected for a QW. At high doping concentrations (short R), a similar analysis leads us to conclude that the expected relaxation time is also shorter in a QW (J_{3D} and θ_{3D} are smaller than J_{QW}, θ_{QW}, therefore $1/\tau_{sa,3D} < 1/\tau_{sa,QW}$). Thus, the theoretical predicted spin relaxation time in bulk is always longer than in a QW. Nevertheless, as we have seen in chapter 1, QWs purify the optical selection rules and allow then a full spin orientation by using resonant excitation of the heavy-holes.

We underline that, in bulk, the reported experimental values shown in Fig. 4.15 are very small compared to the ones predicted by the theory. In particular, for very small doping concentrations (< 10^{15} cm^{-3}) the estimated spin relaxation time due the hyperfine interaction is of the order of 10 ns, and the measured one is more than two orders of magnitude smaller. A similar situation is observed for the maximum relaxation time, which is the result of a combination of the hyperfine interaction and anisotropic exchange interaction: the theoretical value is of the order of 100 ns and the experimental reported value is equal to 2 ns. Moreover, the maximum of the experimental curve occurs at a higher doping concentration than the calculated one. The presence of compensation sites in the sample, which reduces the nominal doping concentration could be at the origin of this last disagreement. Regarding the magnitude of the disagreements, they are likely related to the conditions of the concrete experimental measurements. Sprinzl *et al*. [11] obtained the spin relaxation time by using pump-probe experiments similar to our experiments, but they used femtosecond pulses tuned to the band gap of CdTe. Instead, in our experiments, we use picosecond pulses tuned to the D^0X transition. A femtosecond pulse tuned to the bandgap is able to create a population of delocalized electrons in the conduction band which can remains even after recombination of holes with localized electrons, and also can produce a heat-up of localized electrons. In our experiments, we have performed a resonant excitation of the D^0X transition to minimize all these effects, because they introduce additional spin relaxation mechanisms [31].

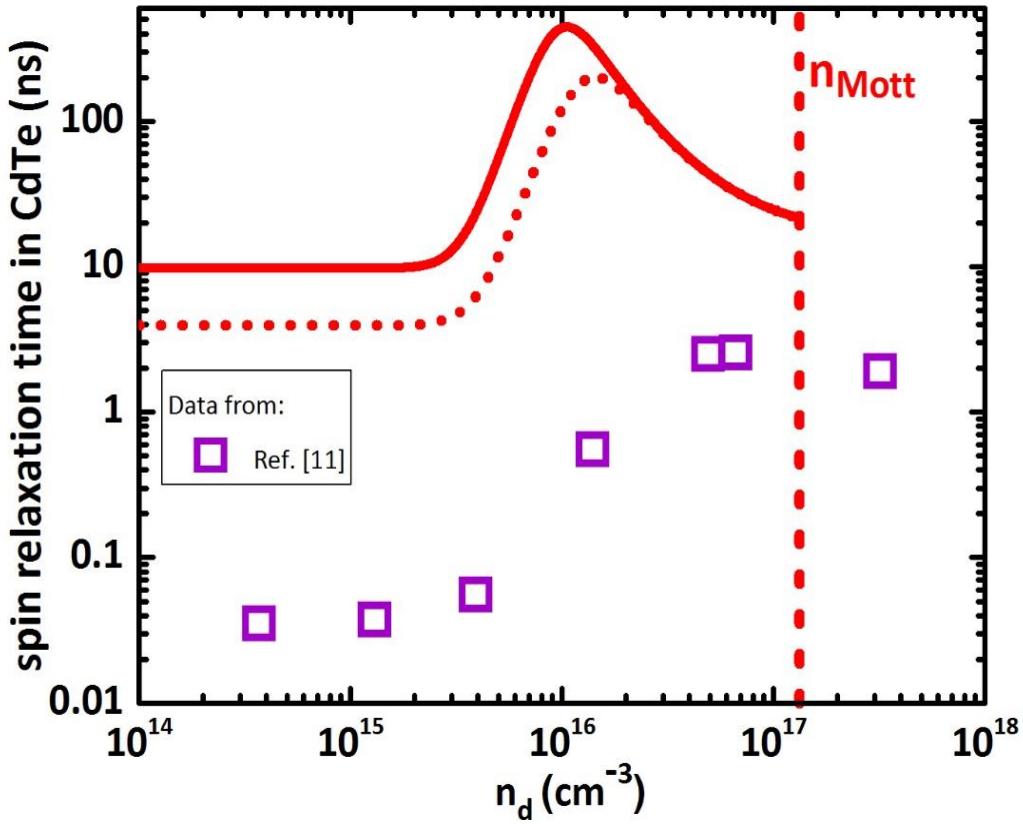

Figure 4.15 *Theoretical spin relaxation time (solid line) as a function of the doping concentration for CdTe bulk. The dotted line represents the spin relaxation time when a volume of a sphere of radius a_B^{*3D} is considered as effective volume V_L in the calculation of T_Δ^e (see section 4.3.1). We have also reported experimental results concerning spin relaxation times at low temperature for bulk CdTe.*

4.5.2 Comparison with other zinc-blende bulk semiconductor materials

Now, let us compare bulk CdTe spin relaxation times with those theoretically estimated and experimentally observed in bulk GaAs (Fig. 4.16 (a)) and ZnSe (Fig. 4.16 (b)) materials. As we have done for bulk CdTe, we have use Eq. (4.17) to calculate the spin relaxation time. The parameters involved in the calculation of T_Δ^e for each material are reported in Table 4.3. The value for the spin-orbit constant of ZnSe has been calculated using $\gamma_c = 1.62$ eV. Å^3[27] and Eq. (4.18).

In Fig. 4.16 (a) we see that, for residual doping concentrations, when the hyperfine interaction is the dominant mechanism, the spin relaxation time predicted for bulk GaAs is of the same order than bulk CdTe: T_Δ^e is equal to 8.6 ns and 9.7 ns, respectively.

In the intermediate regime, the maximum value predicted for bulk GaAs is longer than the one predicted for bulk CdTe, and appear at lower doping concentration. This is explained as follows. First, at low doping concentrations (large R), the exchange energy is smaller in CdTe than in GaAs (see Fig. 3.8(b) of chapter 3), therefore τ_{sn}, which is directly proportional to J, is smaller in CdTe. Second, for high doping concentrations (short R) (see Fig. 3.8(a) of chapter 3), J and θ are greater for CdTe than for GaAs (due to the greater value of the spin-orbit constant and smaller Bohr radius in CdTe) therefore τ_{sa}, which is inversely proportional to them, is smaller. The metal-insulator transition appears for GaAs at a lower doping concentration than for CdTe, since the Bohr radius in CdTe is smaller than in GaAs.

The experimental results for GaAs are slightly shorter than those predicted by the theory but the agreement is rather good. In bulk materials, a circularly polarized excitation creates heavy and light excitons, and then additional spin relaxation mechanisms can appear during the exciton lifetime, affecting also the spin relaxation of the localized electrons. A better agreement with the experimental results is achieved imposing the volume of a sphere of radius equal to the effective bulk Bohr radius, $V_L = 4\pi a_B^{*3}/3$, for the calculation of T_Δ^e (dashed lines in Figs. 4.16 (a) and (b)), as is done in Refs. [13,7].

Figure 4.16 (b) shows that the predicted maximum relaxation time for ZnSe is of the order of $1\mu s$. Recent studies have shown spin relaxation times around 30 ns at lower doping concentrations [7], but there are no other studies in the isolated regime. From a theoretical point of view, ZnSe appears as one possible candidate for obtaining long spin relaxation times.

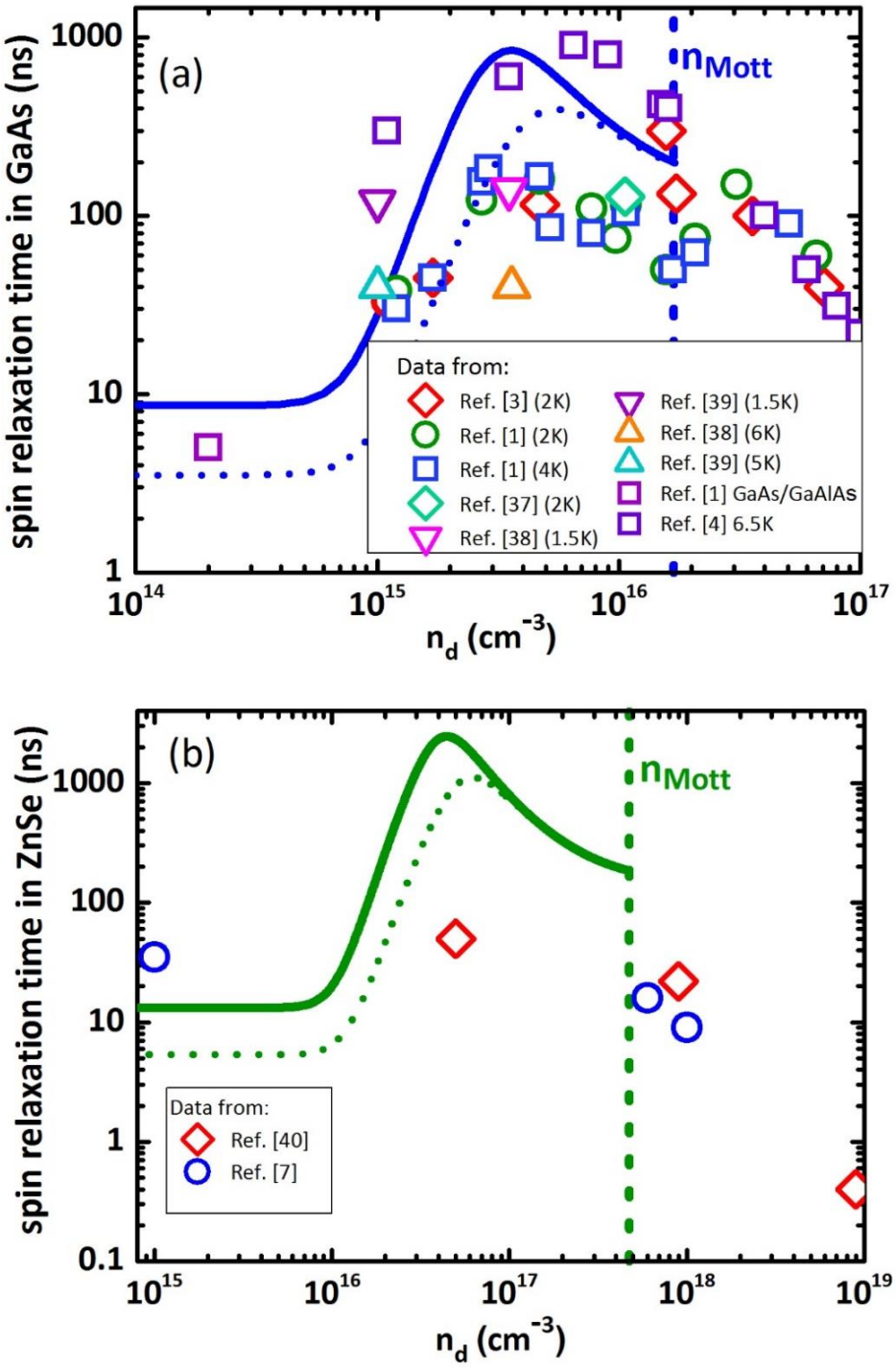

Figure 4.16 *Theoretical spin relaxation times (solid lines) as a function of the doping concentration for bulk (a) GaAs and (b) ZnSe. The dotted lines represent the spin relaxation times when a volume of a sphere of radius a_B^{*3D} is considered as effective volume V_L in the calculation of T_Δ^e (see sec. 4.3.1). We have also reported different experimental results concerning spin relaxation times at low temperature for each material.*

	Effective Mass	Dielectric constant	Isotopes with Non-zero nuclear spin	Nuclear spin	Abundance	Hyperfine constants	Spin- orbit constant	$\mathbf{T}_{\Delta}^{e}$ [29] (ns)
GaAs	0.067[a]	12.35[b]	Ga^{69} Ga^{71} As^{75}	$I_{Ga} = 3/2$ $I_{As} = 3/2$	$P_{Ga} = 100\ \%$ $P_{As} = 100\ \%$	$\sum_I (A^i)^2$ $= 1.2\ 10^{-3} meV^2$ [c]	0.067[d]	8.6
CdTe	0.11[e]	10.2[f]	Cd^{111}, Cd^{113} Te^{123} Te^{125}	$I_{Cd} = 1/2$ $I_{Te} = 1/2$	$P_{Cd} = 25\ \%$ $P_{Te} = 8\ \%$	$A^{cd} = 31\ \mu eV$ $A^{Te} = 45\ \mu eV$	0.079	9.7
ZnSe	0.145[g]	8.8[b]	Zn^{67} Se^{77}	$I_{Zn} = 5/2$ $I_{Se} = 1/2$	$P_{Zn} = 4.11\ \%$ $P_{Se} = 7.58\ \%$	$A^{Zn} = 3.7\ \mu eV$ $A^{Se} = 33.6\ \mu eV$	0.021	13.1

[a]Ref. [32], [b]Ref. [33], [c]Ref. [16], [d]Ref. [34], [e]Ref. [18], [f]Ref. [19], [g]Ref. [35].

TABLE 4.3 *Parameters required for the calculation of the spin dephasing time T_{Δ}^{e} due to the hyperfine interaction in GaAs, CdTe, and ZnSe.*

4.5.3 Comparison with wurzite semiconductor materials

Spin relaxation properties of GaN and ZnO are less known than those of GaAs. These materials with a wurzite crystal structure seem very interesting because they show very long spin relaxation and decoherence times. Indeed, Beschoten *et al*. have measured at 5 K and around 220 mT, a spin coherence time of 7 ns for a doping concentration of 3.5 x 10^{16} cm^{-3} in GaN [8]. In a n-doped ZnO epilayer with concentrations close to the metallic zone, S. Ghosh *et al.* found a spin coherence time of 2 ns at T = 30 K [10].

For wurzite semiconductor materials, the spin relaxation mechanisms described above must be adapted [36]. When the anisotropic exchange interaction is the dominant mechanism, equations (4.13) and (4.14) with $b = 4$ give the spin relaxation time in a wurzite QW. In the following, we make a comparison between the spin relaxation time for a GaAs QW and a ZnO-QW with a doping concentration near the metal-insulator transition, using the calculated *J* for a QW (chapter 3).

In ZnO, γ_e^W has been calculated to be 0.33 eV.$Å^3$ (see Refs [23,26]), two orders of magnitude smaller than for GaAs. By using the parameters given in Table 3.1 (see chapter 3), and for a doping concentration in the insulating regime near the Mott transition (r = 5nm), we are then able to estimate a relaxation time $\tau_{sa}^{ZnO} \approx 16$ ns for a QW with a thickness equal to 10 nm. This value is larger than the one obtained for a GaAs QW of the same thickness, $\tau_{sa}^{GaAs} \approx 150$ ps, and also larger than the relaxation times measured by Ghosh *et al*.[10] on ZnO epilayers close to the Mott transition (0.5 – 2 ns, for $na_B^{*3D} = 0.01 - 0.1$). Nevertheless, the cited experimental values may also depend

on spin relaxation processes not discussed here, and induced by the optical excitation conditions [31].

4.6 Conclusions

Considering the two dominant spin relaxation mechanisms for electron bound to donors, in the insulating regime and at low temperature, we have adapted the bulk theoretical description to a QW. We have then obtained the doping density dependence of the spin relaxation time in the whole insulating regime. Moreover, we estimated from our measured experimental data the value for the dimensionless spin-orbit constant in CdTe: $\alpha_{so} = 0.079 \pm 0.011$. We calculated the electronic spin relaxation time in bulk CdTe, to compare it with available experimental results [11], which are at least one order of magnitude smaller than the spin relaxation time found in our QW system, and two orders of magnitude smaller than those predicted by the theory for a bulk system. We showed that the theoretical spin relaxation times in bulk CdTe are larger than in QWs, when the same mechanisms are considered. We then discussed the possible sources of additional spin relaxation mechanisms that can be present during experimental measurements.

We also discussed and compared theoretical and experimental results in a very well-studied semiconductor, GaAs, to another less studied bulk semiconductor, ZnSe. From the theoretical calculations developed here, this II-VI material appears to be a good candidate for observation of long electron spin relaxation times, of the order of μs.

Finally, when doing the comparison with a wurzite QW made of ZnO, due to the low values of the electron exchange energy and the spin-orbit interaction in ZnO, we deduced that the spin relaxation time in ZnO near the metal-insulator transition should be larger than the one found in GaAs, and then ZnO could be a suitable material for quantum information, provided the entanglement mechanism between spin qubits be different from the electron exchange interaction.

4.7 Bibliography of chapter 4

[1] R. I. Dzhioev, K. V. Kavokin, V. L. Korenev, M. V. Lazarev, B. Ya. Meltser, M. N. Stepanova, B. P. Zakharchenya, D. Gammon, and D. S. Katzer, Phys. Rev. B **66**, 245204 (2002).

[2] V. V. Belykh, E. Evers, D. R. Yakovlev, F. Fobbe, A. Greilich and M. Bayer, Phys. Rev. B **94**, 241202(R) (2016).

[3] V. V. Belykh, K. V. Kavokin, D. R. Yakovlev, and M. Bayer, Phys. Rev. B **96**, 241201(R) (2017).

[4] J. G. Lonnemann, E. P. Rugeramigabo, M. Oestreich, and J. Hübner, Phys. Revi B **96**, 045201 (2017).

[5] D. Guzun, E. A. DeCuir Jr., Vas. P. Kunets, Yu. I. Mazur, G. J. Salamo, S. Q. Murphy, P. A. R. Dilhani Jayathilaka, T. D. Mishima, and M. B. Santos, Appl. Phys. Lett. **95**, 241903 (2009).

[6] B. N. Murdin et al., Phys. Rev. B **72**, 085346 (2005).

[7] A. Greilich, A. Pawlis, F. Liu, O.A. Yugov, D. R. Yakovlev, K. Lischka, Y. Yamamoto, and M. Bayer, Phys. Rev. B **85**, 121303(R) (2012).

[8] B. Beschoten, E. Johnston-Halperin, D. K. Young, M. Poggio, J. E. Grimaldi, S. Keller, S. P. DenBaars, U. K. Mishra, E. L. Hu, and D. D. Awschalom, Phys. Rev B **63**, 121202(R) (2001).

[9] J. H. Buss, J. Rudolph, S. Shvarkov, H. Hardtdegen, A. D. Wiek, and D. Hagele, Appl. Phys. Lett. **102**, 192102 (2013).

[10] S. Ghosh, V. Sih, W. H. Lau, and D. D. Awschalom, Appl. Phys. Lett. **86**, 232507 (2005).

[11] D. Sprinzl, P. Horodyská, N. Tesařová, E. Rozkotová, E. Belas, R. Grill, P. Malý, and P. Němec, Phys. Rev. B **82**, 153201 (2010).

[12] A. A. Syrenko, T. Ruf, M. Cardona, D. R. Yakolev, W. Ossau, A. Waag and G. Landwehr, Phys. Rev. B **56**, 2114 (1997).

[13] J. Tribollet, E. Aubry, G. Karczewski, B. Sermage, F. Bernardot, C. Testelin, and M. Chamarro, Phys. Rev. B **75**, 205304 (2007).

[14] P. Grinberg, F. Bernardot, B. Eble, G. Karczewski, C. Testelin, and M. Chamarro, J. of Appl. Phys. **119**, 123906 (2016).

[15] N. F. Mott, *Metal insulator transitions* (Taylor and Francis, London, 1990).

[16] I. A. Merkulov, Al. L. Efros, and M. Rosen, Phys. Rev. B **65**, 205309 (2002).

[17] A. Nakamura, D. Paget, C. Hermann, C. Weisbuch, G. Lampel, and B. C. Cavenett, Solid State Commun. **30**, 411 (1979).

[18] D. T. F Marple, Phys. Rev. **129,** 2466 (1963).

[19] S. Perkowitz and R. H. Thorland, Phys. Rev. B **9,** 545 (1974).

[20] M. I. D'yakonov and V. I. Perel', Zh. Eksp. Teor. Fiz. **65**, 362 (1973) [Sov. Phys. JETP **38**, 177 (1974)].

[21] G. Garcia-Arellano, F. Bernardot, C. Testelin and M. Chamarro, Phys. Rev. B **98**, 195308 (2018).

[22] K. V. Kavokin, Phys. Rev. B **64**, 075305 (2001).

[23] Y. Fu and M.W. Wu, J. Appl. Phys. **104**, 093712 (2008).

[24] N. J. Harmon, W. O. Putikka, and R. Joynt, Phys. Rev. B **79**, 115204 (2009).

[25] K. V. Kavokin, Phys. Rev. B **69**, 075302 (2004).

[26] L. C. Lew Yan Voon, M. Willatzen, M. Cardona and N.E. Christensen, Phys. Rev. B **53**, 10703 (1996).

[27] M. Cardona, N. E. Christensen, and G. Fasol, Phys. Rev. B **38**, 1806 (1988).

[28] A. N. Chantis, M. Van Schilfgaarde, and T. Kotani, Phys. Rev. Lett. **96**, 086405 (2006).

[29] G. E. Pikus and A. N. Titkov, in *Optical Orientation*, edited by F. Meier and B. P. Zakharchenya (North Holland, Amsterdam, 1984).
[30] L. P. Gor'kov and P. L. Krotkov, Phys. Rev. B **67**, 033203 (2003).
[31] K.V. Kavokin, Semicond. Sci. Technol. **23**, 114009 (2008).
[32] W. Nakwaski, Physica B **210**, 1 (1995).
[33] I. Strzalkowski, S. Joshi, and C. R. Crowell, Appl. Phys. Lett. **28**, 350 (1976).
[34] B. Jusserand, D. Richards, G. Allan, C. Priester and B. Etienne, Phys. Rev. B **51**, 4707 (1995).
[35] I. Hernández-Calderón, in *II-VI Semiconductor Materials and their Applications*, edited by M. C. Tamargo (Taylor and Francis, New York, 2002).
[36] P. I. Tamborenea, T. Wellens, D. Weinmann, and R. A. Jalabert, Phys. Rev. B **96**, 125205 (2017).
[37] J. M. Kikkawa and D. D. Awschalom, Phys. Rev. Lett. **80**, 4313 (1998).
[38] J. S. Colton, T. A. Kennedy, A. S. Bracker, and D. Gammon, Phys. Rev. B **69**, 121307(R) (2004).
[39] J. S. Colton, M. E. Heeb, P. Schroeder, A. Stokes, L. R. Wienkes, and A. S. Bracker Phys. Rev. B **75**, 205201 (2007).
[40] I. Malajovich, J. M. Kikkawa, D. D. Awschalom, J. J Berry, and N. Samarth, J. Appl. Phys. **87**, 5073 (2000).

Chapter 5

Temperature dependence of the spin relaxation time of donor-bound electrons in a CdTe quantum well

Content

5.1 Previous studies

In the previous chapter, we devoted our attention to the study of the spin relaxation time in the insulating regime at low temperature, where electrons are localized on donors. The opposite situation occurs in the metallic regime for very high doping concentrations, where all the electrons are delocalized at any temperature. In this regime, the spin relaxation time is dominated by the D'yakonov-Perel' (DP) or Elliot-Yafet (EY) mechanism, depending on the characteristics of the material [1,2].

Near the MIT, the description of the spin relaxation is less established even at low temperature, because of the co-existence of localized electrons in a band of impurities and itinerant electrons leading to filamentary electron transport [3,4]. Recently, several calculations have attempted to describe at low temperature the spin relaxation beyond the MIT [5,6], based on the model of Matsubara and Toyozawa [7]. The description of the spin relaxation at low temperature implies a fundamental understanding of the spatial dynamics of the electrons [3]. T. Wellens and R. A. Jalabert have described lately the hopping dynamics of electrons in a disordered network of impurity sites [8], but more theoretical work is needed in this direction.

In this chapter, we are interested in studying the influence of the temperature on the electron spin relaxation time of donor-bound electrons immersed in the middle of a QW. In the insulating regime, when temperature increases, electrons bound to donors delocalize, then two populations of electrons exist: localized and itinerant electrons. A recent theoretical model that takes into account the existence and interaction between these two spin populations [9,10] has succeeded to explain the evolution in temperature of the spin relaxation time of donor-bound electrons in bulk GaAs and ZnO [11,12]. Such an approach has also been extended to QWs [13]. We will use this theoretical framework to explain the evolution in temperature of the spin relaxation time for samples B, C, E and F (see section 4.2.1) at a fixed magnetic field.

5.2 Experimental results

To study the spin dynamics of the resident electrons in our samples we use the PKR technique described in chapter 2. The maximum temporal window in this experimental set-up is 1.15 ns, which is well adapted to our systems. In order to study the electron spin dynamics, a fixed magnetic field of B_0 = 0.56 T is applied in Voigt configuration. This value of the magnetic field has been determined by measuring the Larmor precession frequency in a sample with known Landé factor (see eq. (4.4), chapter 4).

The samples studied during this chapter are samples B, C, E and F of chapter 4 (see table 4.1 for their concentrations). Supported by the behavior of $T_2(0)$ with the concentration and by the Mott criterion [14], we have concluded in chapter 4 that samples B, C and E are in the insulating regime, and sample F is slightly above the Mott transition. To characterize the evolution in temperature of the D^0X transition energy, we first study the evolution in temperature of the PL for each of these samples.

5.2.1 Temperature evolution of the photoluminescence

Figure 5.1(a) shows the PL spectra recorded for sample C at different temperatures. At low temperatures, the PL is dominated by a band centered at 1.611 eV and associated to the recombination of the donor-bound exciton (D^0X). A second peak at higher energy, 1.616 eV, is also observed and is identified as the free exciton (X) contribution. As the temperature is increased, both features are shifted to lower energies and the widths of both bands increase. Figure 5.1(b) summarizes the evolution of the energy peaks appearing in the PL of sample C, as a function of the temperature. It is essentially fixed by the evolution of the CdTe QW energy bandgap. We observe that the D^0X band merges with the X one above 60 K. We partly explain this phenomenon by the thermal activation of the D^0X population. We write the variation of the D^0X population with the temperature according to the equation:

$$n_{D^0X}(T) = \frac{n_{D^0X}(0)}{1 + \exp(-\frac{E_l}{k_B T})}, \qquad (5.1)$$

where $n_{D^0X}(T)$ represents the D^0X population at temperature T, $n_{D^0X}(0)$ represents the D^0X population at T = 0 K, and E_l is the binding energy of X on D^0 in the D^0X complex. The binding energy E_l is given by the difference between the D^0X and X lines observed in the PL. Taking the average value of this energy difference, we find $E_l = 3.7$ meV; so at T = 60 K we have $n_{D^0X}(60\ K) = 0.7 n_{D^0X}\ (0)$, meaning that 30 % of the bound excitons have joined the population of free excitons. Figure 5.1(c) shows the PL spectra for sample F, which has a doping concentration slightly above the Mott transition, according to the Mott criterion [14] and the studies reported in Chapter 4. We underline that these PL spectra are broad; contrary to the sample C, we cannot distinguish separate emissions from donor-bound and free excitons.

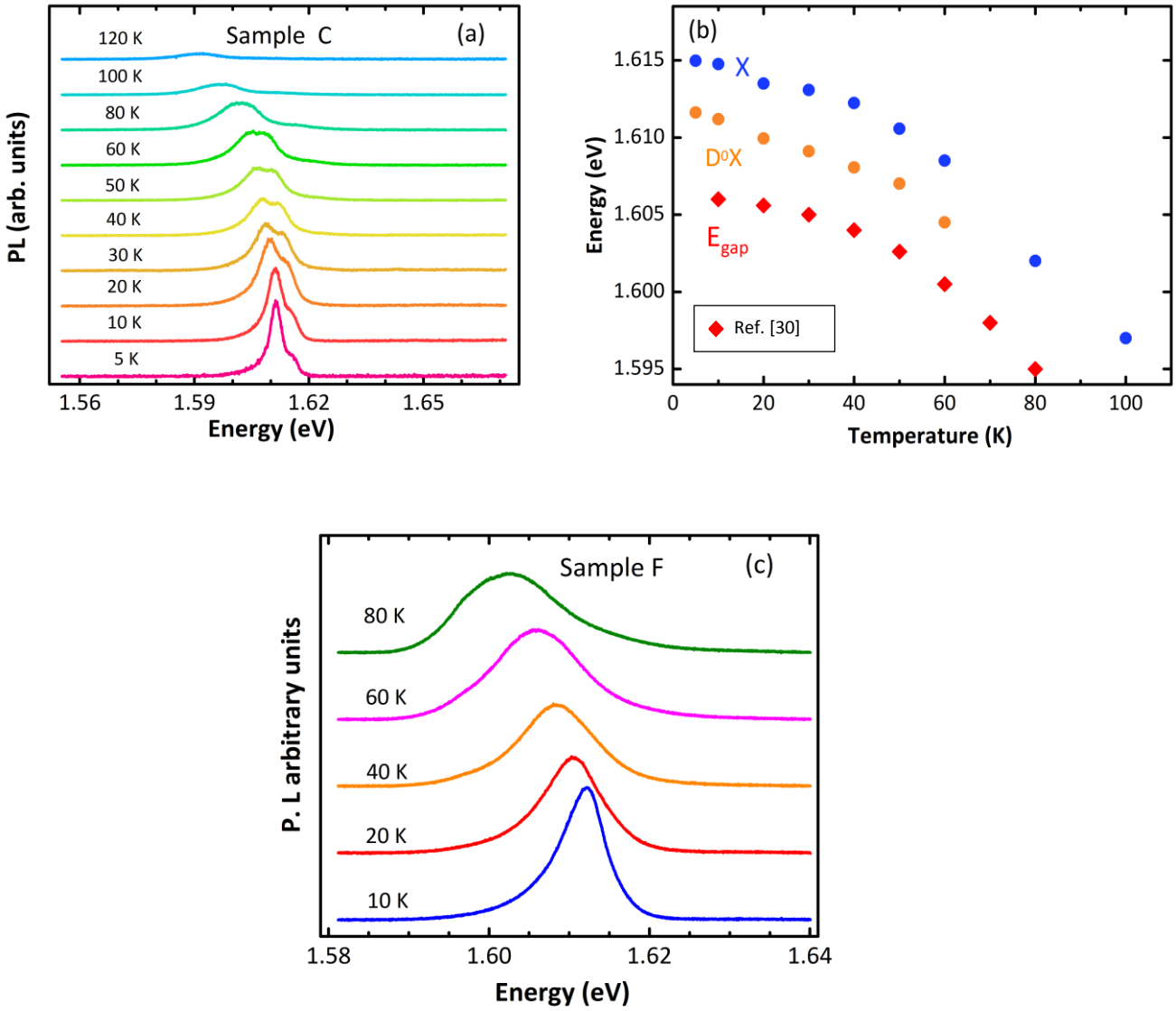

Figure 5.1 *(a) PL spectra of sample C, for temperatures ranging from 5 K to 120 K. (b) Variations with temperature of the peak energies in the PL spectra, for sample C; X: exciton line; D^0X: donor-bound exciton line; E_{gap}: gap energy. (c) PL spectra of sample F, for temperatures ranging from 10 K to 80 K.*

5.2.2 Temperature evolution of the Kerr rotation signal at a fixed magnetic field

The photo-induced Kerr rotation signal obtained on sample C at the temperature T = 50 K, under a magnetic field B_0 = 0.56 T, is shown in Figs. 5.2 (a) and (b) when the pump-probe energy is respectively at the D^0X and X transitions. In both cases, an oscillatory and long-lasting signal is observed. As we have already mentioned, this oscillatory signal, with an envelope time larger than the lifetime of the D^0X complex ($T_R \sim 200$ ps [15]), is the signature of the spin polarization of electrons bound to donors D^0 [16]. We underline that a longer long-lasting signal is observed when the excitation is done in resonance with the D^0X transition. When the excitation is done at higher energies, the spin relaxation time is shorten due to the photo-creation of other species (Ref. [17]).

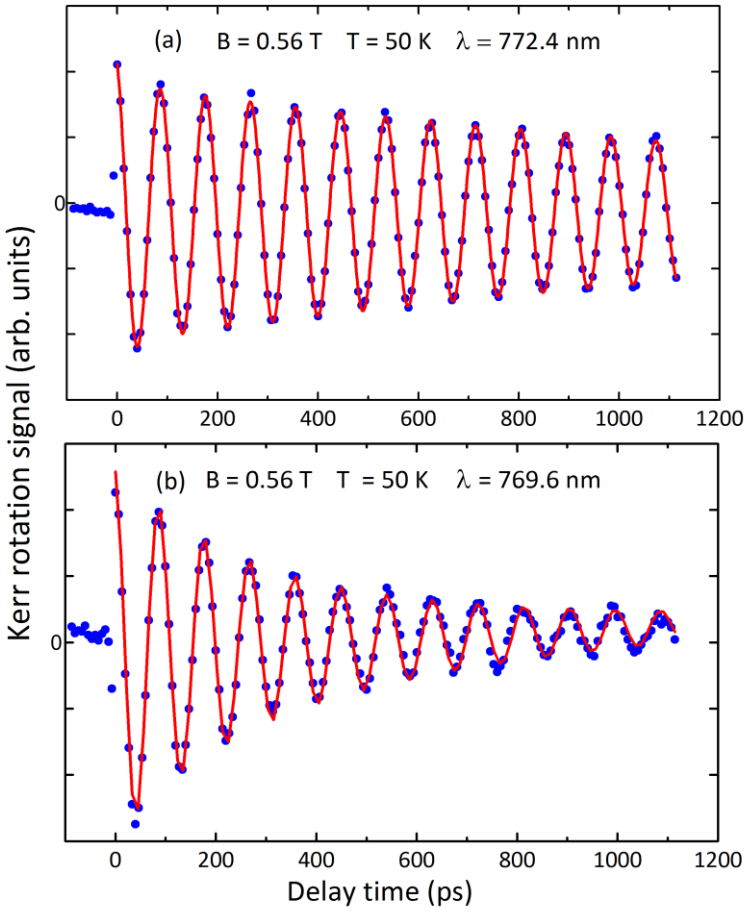

Figure 5.2 *Photo-induced Kerr rotation signals for sample C, in a magnetic field of B_0 = 0.56 T, at T = 50 K. Pump and probe energies are tuned to the wavelength (a) λ = 772.4 nm, D^0X transition; (b) λ = 769.6 nm, X transition. Blue full disks: experimental data; red continuous lines: fits with Eq. (5.2).*

We have studied the temperature evolution of the spin dynamics in samples B, C, E and F. Tuning pump and probe energies at the D^0X transition, we create mainly donor-bound excitons, since the band-width of the used mode-locked Ti:sapphire laser is less than 1 meV. Figures 5.3(a)-(d) represent the photo-induced Kerr rotation signal obtained in samples B-F respectively, in the 10 – 80 K range. The focus spot area is $(3\mu m)^2$ and the energy of the pump pulses is 0.9 μJ cm^{-2}.

Two components are visible in each curve. To extract the times and relative amplitudes of the short- and long-living components, we have fitted each curve with the equation:

$$PKR(t) = A_2 e^{-t/T_x} \cos(\Omega_x t) + A_3 e^{-t/T_2^*} \cos(\Omega_e t), \qquad (5.2)$$

where A_2 and A_3 are constants describing the amplitudes of the fast (T_x) and slow (T_2^*) components with Larmor frequencies Ω_x and Ω_e, respectively. As we have seen in chapter 4, eq. 4.3, the fast component is associated with the exciton contribution, and the second one with the D^0 contribution. The component related with the exciton contribution becomes more evident at high temperature.

In all the samples, the spin dephasing time T_2^* of electrons bound to donors becomes shorter as the temperature is increased. Sample C shows slower decays at all temperatures. In particular, at low temperatures 10-30 K, it exhibits almost no decay in the 1-ns measurement window, making the determination of the spin dephasing time less accurate.

Figure 5.4 shows the fit of expression (5.2) to the experimental data obtained for sample E at different temperatures with B_0 = 0.56 T. The Larmor precession frequency of the donor-bound electrons is $\Omega_e = 68.5$ rad ns^{-1}; the values of T_2^* at different temperatures are indicated in the figure. As can be seen T_2^* decreases as the temperature is increased

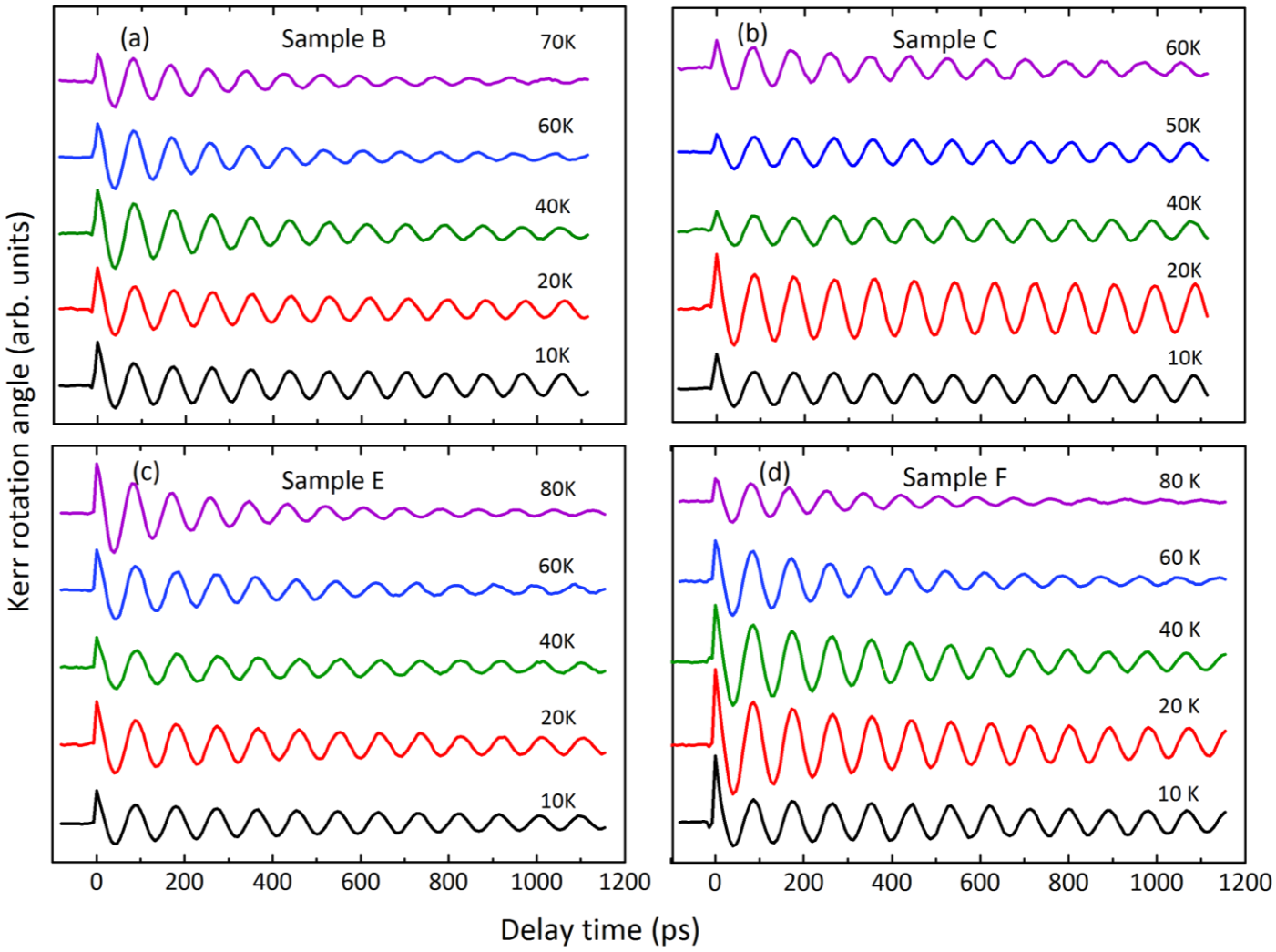

***Figure 5.3**. Photo-induced Kerr rotation signals in a magnetic field B_0 = 0.56 T, at different temperatures, in (a) sample B; (b) sample C; (c) sample E; (d) sample F. Pump and probe energies are tuned to the D^0X transitions.*

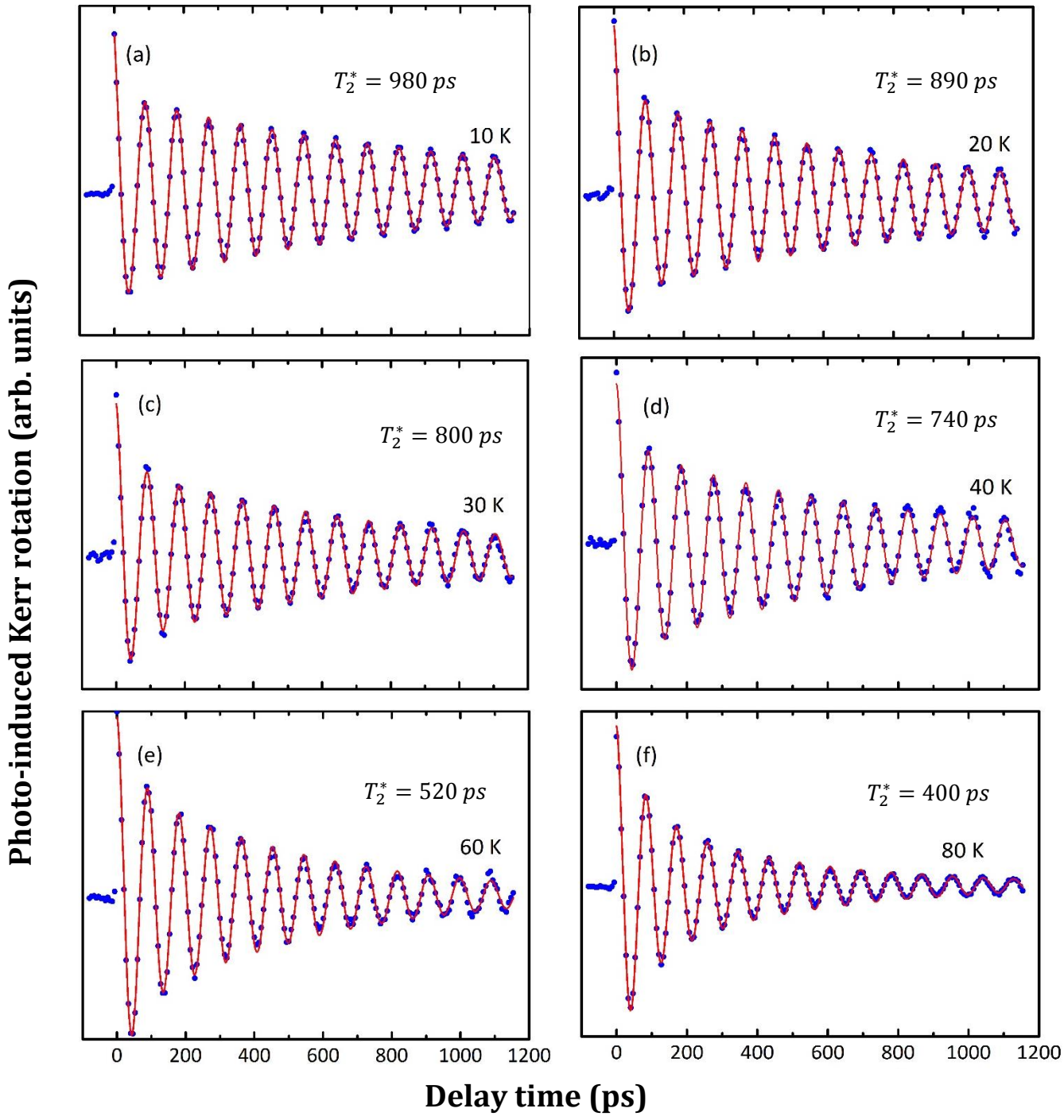

Figure 5.4 *Fit of expression (5.2) to the PKR signals at different temperatures for sample E, at* $B_0 = 0.56$ *T. (a) T = 10 K, the measured* T_2^* *is 980 ps; (b) T = 20 K,* T_2^* *= 890 ps ; (c) T = 30 K,* T_2^* *= 800 ps; (d) T = 40 K,* T_2^* *= 740 ps; (e) T = 60 K,* T_2^* *= 520 ps; (f) T = 80 K,* T_2^* *= 400 ps. At all the temperatures, the measured Larmor frequency is* $\Omega_e = 68.5$ rad ns^{-1}.

5.3 Spin relaxation mechanisms: theoretical considerations

5.3.1 Spin relaxation mechanisms for conduction electrons

In chapter 4, we have revisited the spin relaxation mechanisms for localized electrons (see section 4.3). We describe here the two principal mechanisms responsible for the spin relaxation of conduction electrons: Elliot-Yafet and D'yakonov-Perel' mechanisms.

a. D'yakonov-Perel' mechanism

An efficient mechanism due to spin-orbit coupling in systems lacking inversion symmetry was found by M. I. D'yakonov and V. I. Perel' in 1971 [18]. This mechanism can be interpreted in terms of an effective magnetic field of spin-orbit interaction, which acts upon the electron spin. The electron spin precesses in this effective magnetic field for a time τ_p until a collision occurs. The value and direction of the spin-orbit field are determined by the electron $\vec{k}$ vector and its direction with respect to the crystal axes. Thus, frequent collisions with impurities or phonons, which change the electron wave vector, make the spin-orbit field fluctuates, resulting in a dynamical suppression of spin relaxation.

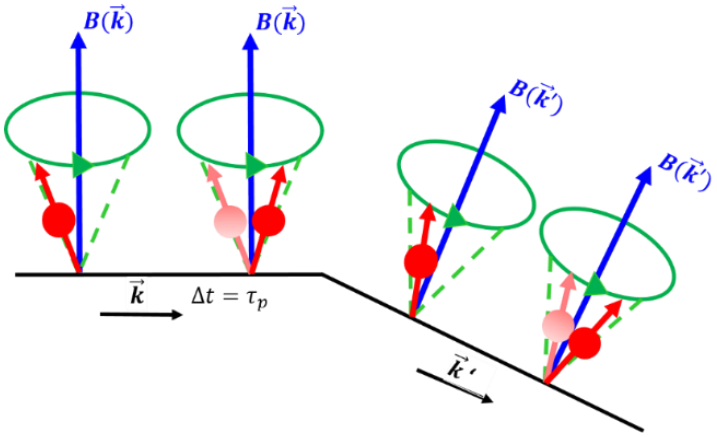

Figure 5.5 *Schematic representation of the DP mechanism. The spin of a conduction electron (red arrow) precesses around a constant spin-orbit field $\vec{B}(\vec{k})$ between each collision.*

The DP theory has been recently generalized to describe the spin relaxation time for an electron gas in a QW at any temperature [19]. The spin relaxation time τ_s^{DP} is written as a function of the temperature via the Fermi distribution function and the temperature dependence of the transport mobility:

$$\frac{1}{\tau_s^{DP}} = \frac{4}{\hbar^2}\frac{\beta E_F \tau_{tr}}{1-e^{-\beta E_F}}\left[\gamma_c^2\langle k_z^2\rangle^2\frac{\zeta}{\beta} - \frac{\gamma_c^2\langle k_z^2\rangle}{2}\left(\frac{\zeta}{\beta}\right)^2\frac{J_{\nu+2}(\beta\mu_0)}{J_{\nu+1}(\beta\mu_0)} + \left(1+\frac{\tau_3}{\tau_1}\right)\gamma_c^2\left(\frac{\zeta}{\beta}\right)^3\frac{J_{\nu+2}(\beta\mu_0)}{J_{\nu+1}(\beta\mu_0)}\right], \tag{5.3}$$

where $\mu_0 = k_B T \ln(e^{\frac{E_F}{k_B T}} - 1)$ is the chemical potential, $E_F = \frac{\hbar^2\pi}{m_e^*}n_c$ is the Fermi energy with m_e^* the effective electron mass, and n_c the concentration of conduction electrons in 2D, γ_c is the Dresselhaus coefficient, which can be determined from the spin-orbit

constant α_{so} obtained in Chapter 4 (see eq. 4.18), $\langle k_z^2 \rangle$ is the average value of the squared z component of the electron wave vector (see chapter 1), $\zeta = 2m_e^* / \hbar^2$, $\beta = 1/k_B T$, τ_3/τ_1 is a constant describing the angular scattering characteristics of the scattering mechanism, and τ_{tr} is the transport collision time (also denoted τ_p) given by:

$$\tau_{tr} = \tau_p = \frac{\Xi J_{\nu+1}(\beta\mu_0)}{\beta^{\nu+1} E_F}, \tag{5.4}$$

with $J_n(z) = \int_0^\infty \frac{x^n}{4cosh^2\left(\frac{x-z}{2}\right)} dx$ and Ξ a coefficient that varies slightly with the temperature, independent of energy, and related with the power law dependence of τ_1 on the energy. The index ν takes the values 0, 1 or 2 depending on the scattering type [19]. Each type of scattering encloses different scattering mechanisms: type I is associated to acoustic phonons, optical phonons, screened ionized impurities, neutral impurities, alloy scattering and interface roughness; type II, with acoustic and optical phonons; and type III, with weakly screened ionized impurities (Ref. [19]).

b. Elliot-Yafet mechanism

In 1954, Elliot and Yafet showed that conduction electron spins can relax via ordinary momentum scattering [2] (such as phonons or impurities). Figure 5.6 shows a scheme of the EY mechanism. The spin information is lost at each collision undergone by the electron.

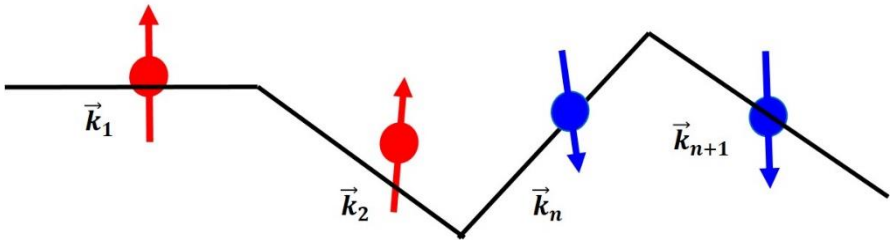

Figure 5.6 *Schematic representation of the EY mechanism.*

Fishman and Lampel [20] deduced the expression for the spin relaxation rate $1/\tau_s^{EY}(E_{\vec{k}})$ in bulk materials, by assuming that the potential due to the spin-orbit interaction varies slowly on the scale of a unit cell:

$$\frac{1}{\tau_s^{EY}(E_{\vec{k}})} \sim \left(\frac{\Delta_{so}}{E_g + \Delta_{so}}\right)^2 \left(\frac{E_{\vec{k}}}{E_g}\right)^2 \frac{1}{\tau_p(E_{\vec{k}})}, \tag{5.5}$$

with Δ_{so} the spin-orbit splitting energy, and $E_{\vec{k}}$ the electron kinetic energy which is equal to $k_B T$ for non-degenerate densities and to E_F for the degenerate ones [21].

The expression for τ_s^{EY} has been adapted to a QW's [22]:

$$\frac{1}{\tau_s^{EY}(E_{\vec{k}})} \sim A \left(\frac{\Delta_{so}}{E_g + \Delta_{so}}\right)^2 \left(1 - \frac{m_e^*}{m_0}\right)^2 \frac{E_{1e} E_{\vec{k}}}{E_g^2} \frac{1}{\tau_p(E_{\vec{k}})}, \tag{5.6}$$

with E_{1e} the first quantum confinement energy of the electron in the QW. From this expression, we can see that the EY mechanism becomes important for small-band-gap semiconductors with large spin-orbit splittings. The pre-factor A is of the order of unity, without being known more precisely.

The most important difference between the EY and DP mechanisms is their opposite dependence on τ_p. In the EY process, the electron spin changes orientation at each collision, the more collisions there are, the greater is the loss of spin memory. In the DP mechanism, the spin phases are randomized between collisions, since the electron spin precesse with different frequencies depending on their momenta.

5.3.2 Temperature evolution of the spin relaxation time in QWs

The temperature dependence of the spin relaxation time for an electron localized on donor has been explained in bulk and QWs invoking spin exchange between two spin species: spin localized on donors, and spin carried by itinerant electrons [9, 10, 13].

At low temperatures, the donors are nearly all occupied and the electron spins are localized. As the temperature is increased, the number of conduction electrons increases due to the thermal ionization of the electron bound to donors. The electronic spins localized on the donors interact with the spin of conduction electrons by isotropic exchange interaction. This interaction conserves the total spin; assuming that the cross relaxation is fast enough, the total spin is equilibrated between localized and conduction electrons by taking into account their thermal equilibrium concentrations. Taking into account the existence of these two spin systems, the spin relaxation rate of donor-bound electrons at zero magnetic field is found in the form [13]:

$$\frac{1}{\tau_s} = \frac{n_l}{n_{imp}}\frac{1}{\tau_l} + \frac{n_c}{n_{imp}}\frac{1}{\tau_s^c}, \tag{5.7}$$

where $n_l(T)$ $[n_c(T)]$ is the localized [conduction] equilibrium concentration, $n_{imp} = n_l + n_c$ is the total impurity concentration, and τ_l (τ_s^c) is the localized (conduction) spin relaxation time. $n_l(T)$ can be determined exactly in 2D, at any temperature [24]:

$$\frac{n_l(T)}{n_{imp}} = \frac{\sqrt{1+Q(T,n_{imp})}-1}{\sqrt{1+Q(T,n_{imp})}+1}, \tag{5.8}$$

with $Q\left(T, n_{imp}\right) = \frac{8n_{imp}}{N_c} e^{-\frac{E_B}{k_B T}}$, $N_c = m_e^* k_B T/\hbar^2\pi$, and E_B the binding energy of an electron bound to a donor. $n_c(T)/n_{imp}$ can be found using the constraint:

$$\frac{n_l(T)}{n_{imp}} + \frac{n_c(T)}{n_{imp}} = 1\,. \tag{5.9}$$

For vanishing temperatures, when n_{imp} is on the range of the insulating regime, $n_l(T)$ goes to n_{imp} and $n_c(T)$ goes to zero. However, as we will explain later $n_c(0) \neq 0$ when n_{imp} is above the MIT. The spin relaxation mechanisms for localized and conduction electrons that govern the times τ_l and τ_s^c appearing in Eq. (5.7) are in principle the same as at low temperature. For localized electrons, τ_l is determined by Eq.

(4.17) of chapter 4, while for conduction electrons, the DP mechanism governs the spin relaxation time, Eq. (5.3).

5.4 Analysis of the results

We have experimentally determined in our four samples, for the temperature range 10 – 80 K, the long-lasting spin dephasing time T_2^* [see Eq. (5.2)] at a fixed magnetic field of $B_0 = 0.56$ T. The experimentally measured dephasing time is affected by inhomogeneities caused by the local variations of the electron $g_e^\perp$ factors. As we have seen in chapter 4, T_2^* is related with the spin relaxation time $\tau_s = T_2(0)$ of a single electron by the expression (see eq. (4.5) of chapter 4):

$$\frac{1}{T_2^*} = \frac{1}{\tau_s} + \frac{\Delta g_e^\perp \mu_B B_0}{\hbar}. \tag{5.10}$$

The width $\Delta g_e^\perp$ of the $g_e^\perp$ distribution for each sample has been determined in chapter 4. We have fitted the measured T_2^{*-1} for samples B to F with Eq. (5.10) using τ_s^{-1} given by the model proposed by Harmon *et al.* [13] [Eq. (5.7)]:

$$\frac{1}{T_2^*} = \frac{n_l}{n_{imp}}\left(\frac{1}{\tau_l} + \frac{\Delta g_e^\perp \mu_B B_0}{\hbar}\right) + \frac{n_c}{n_{imp}}\left(\frac{1}{\tau_s^c} + \frac{\Delta g_e^\perp \mu_B B_0}{\hbar}\right), \tag{5.11}$$

In the remainder we note $\frac{1}{\tau_l} + \frac{\Delta g_e^\perp \mu_B B_0}{\hbar} = \frac{1}{\tau_l^*}$ the spin dephasing rate of the ensemble of localized electrons. We have neglected the inhomogenities of $g_e^\perp$ factors for conduction electrons, because in a previous work on a 8-nm CdTe QW containing a 2D electron gas [25], the spin relaxation time of conduction electrons showed to be negligibly sensitive to these inhomogenities.

5.4.1 Insulating regime

For samples B, C and E in the insulating regime, the spin dephasing rate T_2^{*-1} is shown in Figs. 5.7 (a)-(c). We have considered that the conduction electrons relax according to the DP mechanism ($\tau_s^c = \tau_s^{DP}$), Eq. (5.3). It will be shown *a posteriori* that the contribution of the EY mechanism is negligible. In order to identify which type of scattering is dominant, we have fitted the experimental data scanning the values $\nu = 0, 1$ and 2 in Eq. (5.3). In this regime, the Fermi energy varies with the temperature-dependent concentration $n_c(T)$, determined by Eqs. (5.8) and (5.9). For each sample, the parameters to be determined are: the binding energy E_B, the spin dephasing time τ_l^*, and the coefficient Ξ (assumed to be a constant independent on T).

In Fig. 5.7, the blue solid line shows the spin dephasing rate T_2^{*-1} as a function of the temperature, according to Eqs. (5.8) and (5.11), and using the type-I scattering ($v = 0$) in τ_s^{DP}, Eq. (5.3). Since it is impossible to fit the experimental data assuming type-II ($v = 1$) or type-III ($v = 2$) scatterings, we can firmly identify the type-I scattering as the effective one in the studied samples. Table 5.1, on page 113, gives the fitting parameters E_B, τ_l^* and Ξ for all studied samples.

At low temperatures, it has been shown that the mechanism that governs the spin relaxation in sample B (with a low-doping concentration) is the hyperfine interaction (see chapter 4). In chapter 1, the binding energy for an isolated donor has been calculated to be $E_B = 24.7$ meV in sample A. Taking this theoretical value as a starting point, we have fitted the experimental data for sample B, with only τ_l^* and Ξ as free parameters [see dashed line in Fig. 5.7(a)]. We have obtained $\tau_l^* = 1.47 \pm 0.05$ ns and $\Xi = 146$ fs. As shown in Fig. 5.7(a), a lower binding energy is needed to agree better with the experimental results; the solid line represents the spin dephasing time considering a lower binding energy, $E_B = 19$ meV. The value extracted for the spin dephasing time of the localized electrons, $\tau_l^* = 1.40$ ns, compares well with 1.97 ns calculated (from the the linear dependence of $T_2^*(B)^{-1}$ found in chapter 4, see table 4.2) in the same magnetic field B_0 = 0.56 T, at 2 K [black diamond in Fig. 5.7(a)].

In Eq. (5.8), the concentrations $n_l(T)$ [and $n_c(T)$] of localized and [conduction electrons] have a strong dependence on the binding energy. The smaller the binding energy, the lower the temperature at which a donor is ionized. In QWs, there is no theory that predicts a value for the binding energy at any doping concentration. Nonetheless, in bulk systems, it has been generally shown, theoretically and experimentally, that the binding energy of a donor-bound electron decreases when the doping concentration increases [26-29]

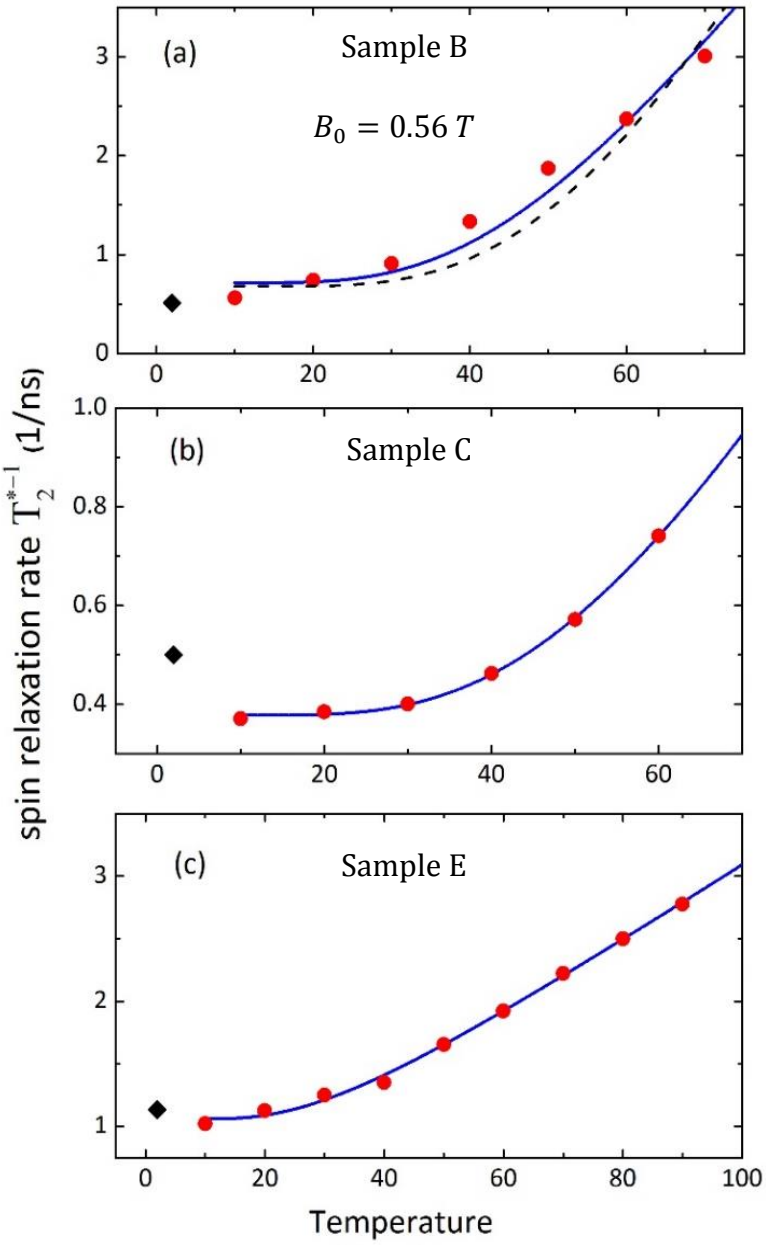

Figure 5.7 *Measurements of the spin dephasing rates at different temperatures (red full disks) in (a) sample B; (b) sample C; (c) sample E. The blue continuous lines are theoretical fits according to Eqs. (5.3), (5.8) and (5.11), for the type-I scattering ($\nu = 0$). The fitting parameters are given in Table 5.1. The dashed line in Fig. (a) is a theoretical fit forcing E_B = 24.7 meV. The black full diamonds are data points calculated using the dependence of $T_2^{*\,-1}$on the magnetic field for each sample (see chapter 4, Table 4.1).*

As can be seen in Fig. 5.8 (a), right axis, the density of conduction electrons in sample B starts to increase at a temperature around 25 K, and at T = 100 K, almost one half of the donors has been ionized. In Fig. 5.8 (a), the conduction spin relaxation time is also plotted as a function of the temperature, with E_B = 19 meV and $\Xi = 97$ fs, known from the theoretical fit of Fig. 5.7(a). As the density of conduction electrons increases with the temperature, the spin relaxation time decreases.

Sample C contains an intermediate doping concentration, and the mechanism that governs the spin relaxation time of the localized electrons is an interplay between the hyperfine and the anisotropic exchange interaction (see Fig. 4.12, chapter 4). Since there is no theory that predicts a value of the binding energy for this doping concentration, we took it as a free parameter to fit the data of Fig. 5.7(b). The values extracted from the theoretical fit are: $E_B = 20$ meV, $\tau_l^* = 2.65$ ns, and $\Xi = 36$ fs. The value of the localized spin dephasing time τ_l^* is of the same order as the one calculated from the data of chapter 4, at 2 K, in the magnetic field $B_0 = 0.56\ T$ [black diamond in Fig. 5.7 (b)]. The difference between the values may come from slightly different experimental conditions, in particular, the density of excitation.

Finally, sample E contains a doping concentration that is close to the metal-insulator transition while keeping in the insulating regime. The principal spin relaxation mechanism for localized electrons in this region is the anisotropic exchange interaction (Fig. 4.12, chapter 4). The values extracted from the theoretical fit in Fig. 5.7(c) are: $E_B = 8$ meV, $\tau_l^* = 0.95 \pm 0.05$ ns, $\Xi = 47$ fs. The value for the localized spin dephasing time agrees well with the calculated value of 0.9 ns found, at 2 K, in the magnetic field $B_0 = 0.56$ T, following the study of chapter 4.

For this sample E, due to the small binding energy $E_B = 8$ meV, the localized electrons start to ionize at low temperature, see Fig. 5.8(c). At high temperature, T ~ 100 K, the conduction spin relaxation time is of the order of 100 ps. This value compares well to the one observed in 2D electron gas of n-doped CdTe QW with a similar concentration at low temperature [25].

We suspect that, due to the kind of the studied system (donors inside a QW) and the range of temperatures 10-80 K, scatterings with neutral impurities and with screened ionized impurities (at the highest temperature) are the more probable scattering mechanisms. But we cannot exclude other mechanisms, as for example the one related to the interface roughness. Because we worked at relatively low temperature, we exclude however the scattering due to acoustic phonons.

We underline that Fig. 5.8, right axis, shows the calculated density of conduction electrons as a function of the temperature, which is equal to the density of ionized impurities. Then for samples B, C and E at the middle of the explored temperature domain, the density of ionized impurities becomes only 10 % or 20 % of the total amount of donors in the sample. At 80 K, the density of ionized impurities becomes larger and, in particular for sample E, can reach a value of 35 % of the total amount of donors in the sample. This shows that, in the explored domain of temperatures, the donors are mostly in their neutral state. Moreover, the ionized donors are likely to be screened by conduction electrons which are confined inside the QW.

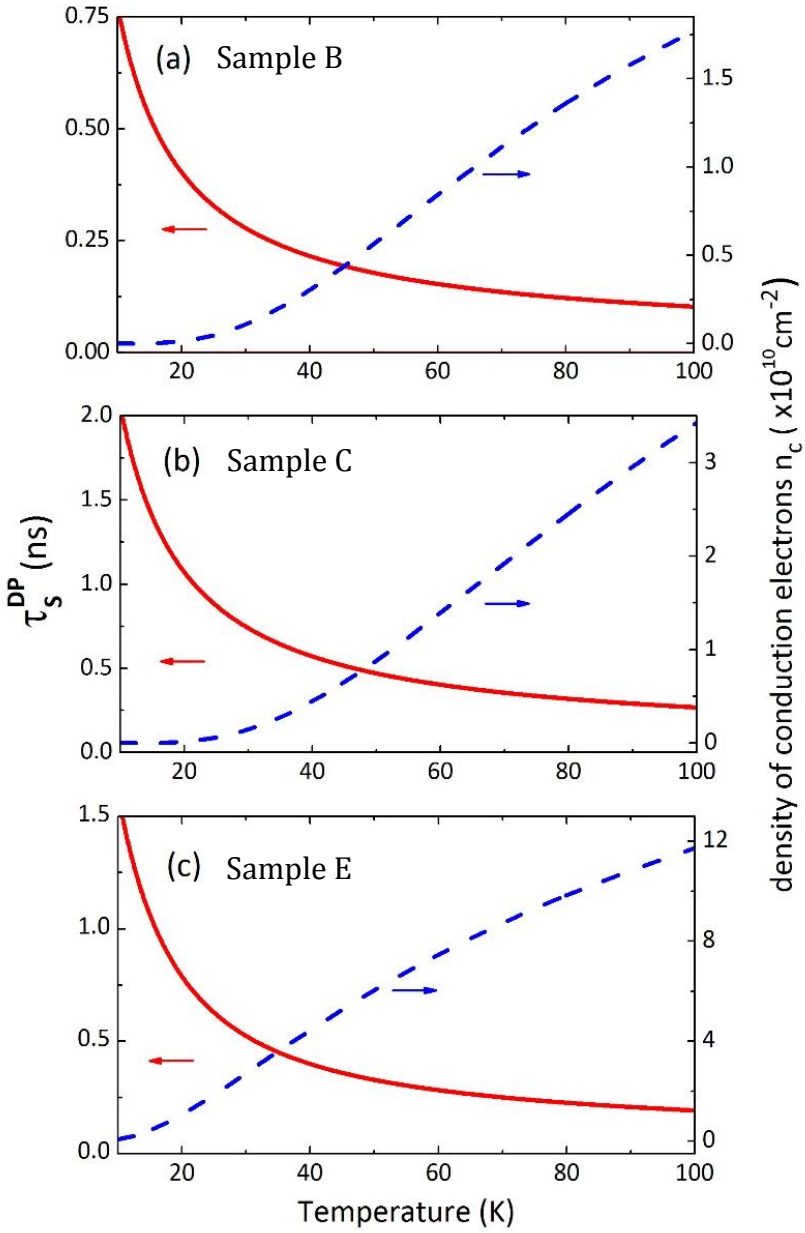

Figure 5.8 *Concentrations of conduction electrons (dashed lines, right axis), and spin relaxation times of the conduction electrons (continuous lines, left axis) versus temperature, in (a) sample B; (b) sample C; (c) sample E.*

5.4.2 Metallic regime, near the MIT

Under the Mott criterion [14], and following the measurements carried out in chapter 4, sample F is assumed to contain a doping concentration slightly beyond the MIT; conductance measurements could have confirmed this point, but our samples are not patterned for transport experiments. We found that the experimental data on this sample could *not* be fitted by considering only a population of conduction electrons and a dephasing time related to DP or/and EY mechanisms. For doping concentrations slightly above the MIT, it has been shown that there is a coexistence between localized electrons forming an impurity band, and itinerant electrons, leading to a filamentary electronic transport [4].

In order to explain the spin dephasing time observed in sample F, we have considered that at very low temperature a fraction f of the doping concentration n_{imp} is in the conduction band: $n_c(0) = f n_{imp}$. Thus, at any temperature the density of localized electrons is given by a refined version of Eq. (5.8):

$$n_l(T) = n_l(0)\frac{\sqrt{1+Q(T,n_l(0))}-1}{\sqrt{1+Q(T,n_l(0))}+1}, \tag{5.12}$$

with $n_l(0) = n_{imp}(1-f)$ the initial concentration of localized donors. The density of conduction electrons at any temperature is evaluated from the conservation rule $n_c(T) = n_{imp} - n_l(T)$. Figure 5.9(a) shows the theoretical fit of the measured spin dephasing time according to Eqs. (5.11) and (5.12), using Eq. (5.3) for the spin relaxation time of the conduction electrons. We have taken as free parameters the binding energy E_B of the donor-bound electron, the transport coefficient Ξ, the spin dephasing time τ_l^* of the localized electrons, and the fraction $f = n_c(0)/n_{imp}$ of conduction electrons at vanishing temperatures.

Scanning the values $\nu = 0, 1$ and 2 in Eq. (5.3), we identify that the type of scattering undergone by the conduction electrons in sample F is also the type-I of scattering ($\nu = 0$). The fitting parameters are found to be: $f = 0.1$, $E_B = 6$ meV, $\tau_l^* = 1.63$ ns and Ξ = 47 fs. The black diamond in Fig. 5.9(a) represents the spin dephasing time calculated from the T_2^{*-1} formula obtained in chapter 4, at 2 K, in the magnetic field B_0 = 0.56 T; this value agrees well with our experimental data.

In Fig. 5.9(b), the conduction spin relaxation time (left axis) is plotted as a function of the temperature, with E_B = 6 meV and $\Xi = 47$ fs; the density of conduction electrons is also plotted (right axis). As the temperature increases, due to the small binding energy, the density of conduction electrons increases at a faster rate in comparison with the samples in the insulating regime.

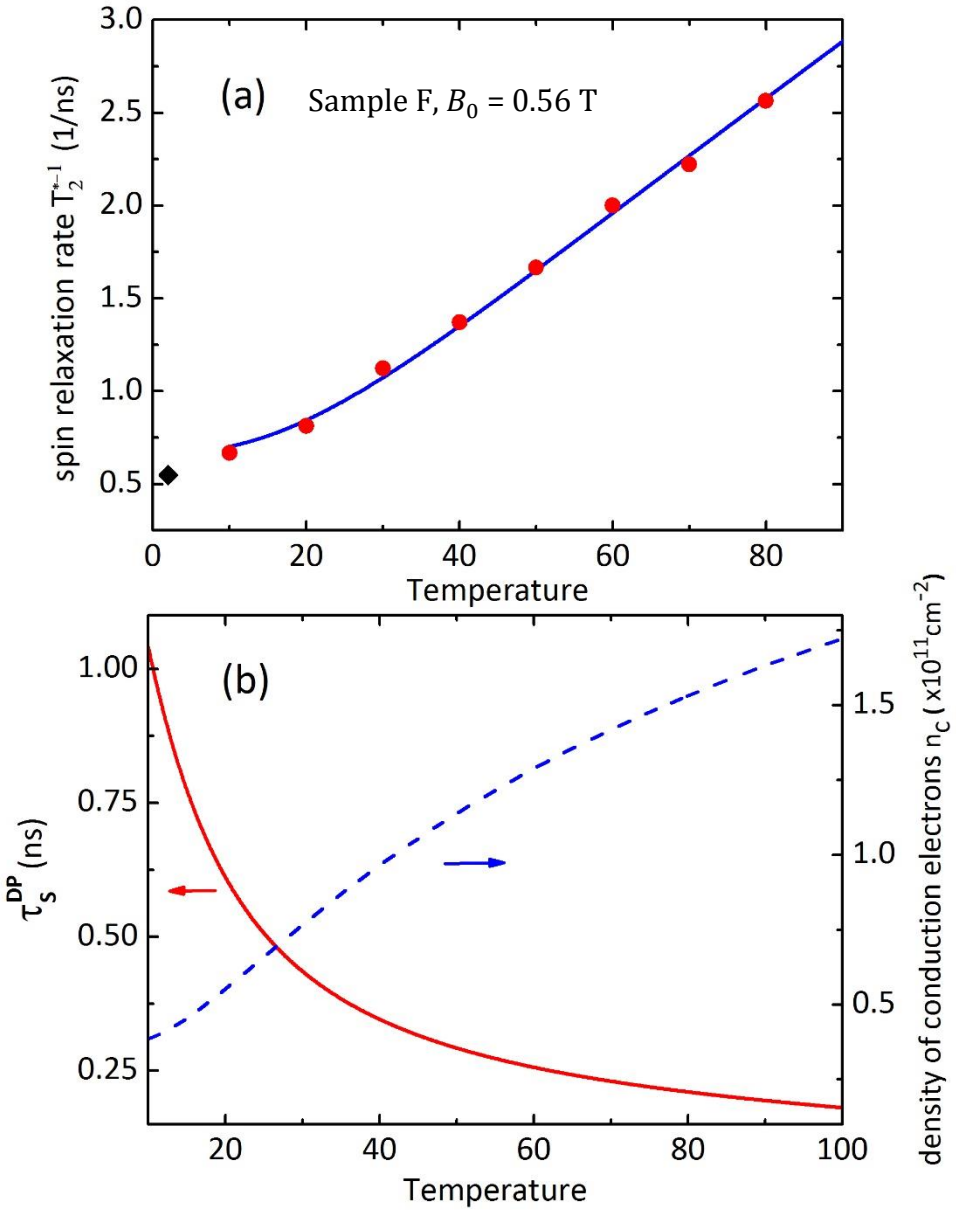

Figure 5.9 *(a) Measurements of the spin dephasing rates at different temperatures (red full disks) in sample F. The blue continuous line is a theoretical fit according to Eqs. (5.3), (5.11) and (5.12), for the type-I scattering ($\nu = 0$). The fitting parameters are given in Table 5.1. The black full diamond is a data point extracted from chapter 4. (b) Concentration of conduction electrons (dashed line, right axis), and spin relaxation time of the conduction electrons (continuous line, left axis) versus temperature, in sample F.*

For conduction electrons in materials with a large spin-orbit constant or narrow energy band gap, the EY mechanism of spin relaxation becomes dominant [13]. The spin-orbit constant of CdTe is three times larger than the one of GaAs, material for which it has been shown that EY mechanism is not effective as compared to the DP one [13]. Using $\tau_{tr} = \Xi$ (table 5.1) obtained here and expression (15) of Ref. [22], the DP relaxation rate is found more than 10 times larger than the EY one, in the range of temperatures studied and for all the samples, see Fig. 5.10. This justifies, *a posteriori*, our use of the DP mechanism to describe the spin relaxation of conduction electrons in our samples.

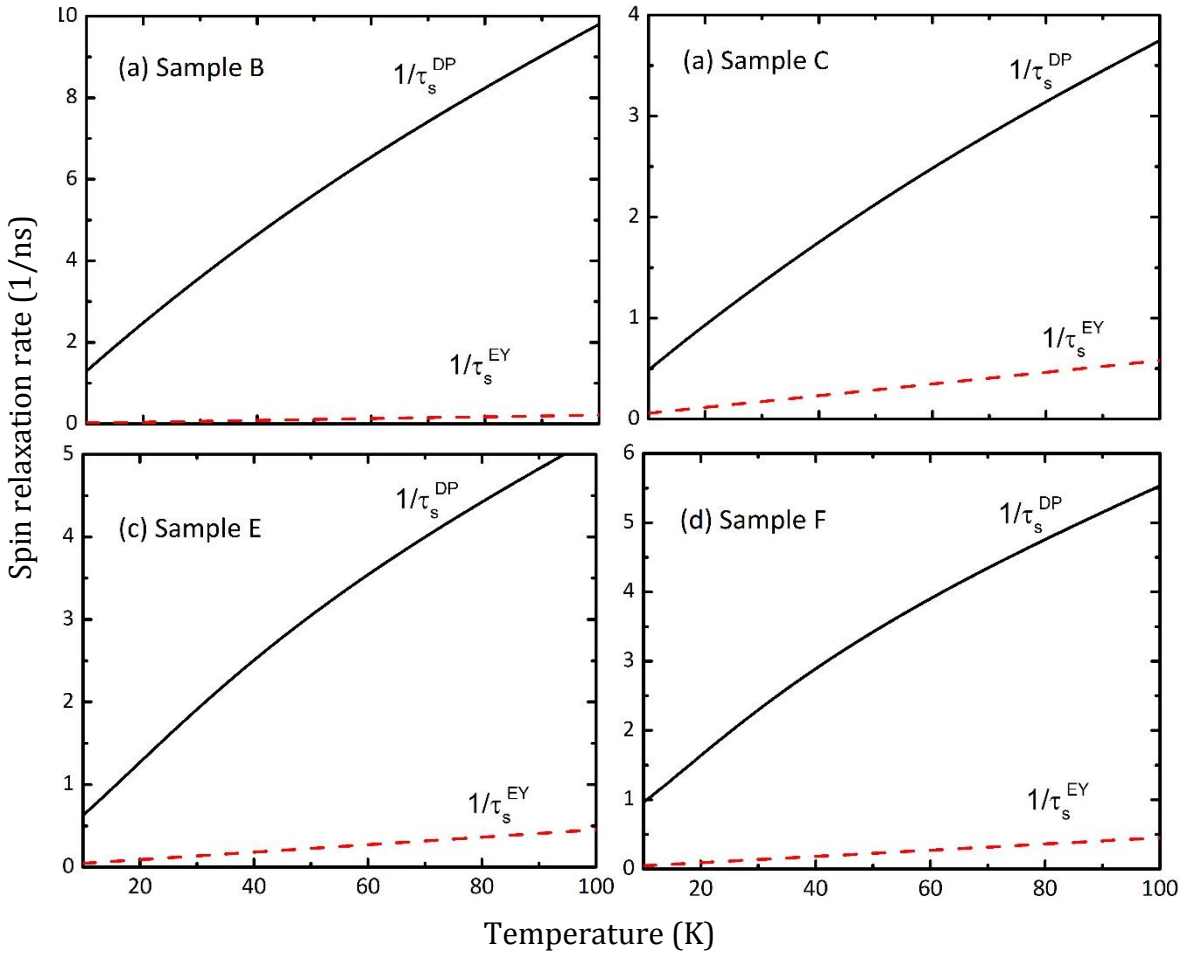

Figure 5.10 *Spin relaxation rate according to the DP mechanism, Eq. (5.3) (black-solid line), and to the EY mechanism, Eq. (5.6) (red-dashed line), for each of the samples in the insulating regime: (a) sample B, (b) sample C, (c) sample E, and in the metallic regime: (d) sample F.*

Sample	Doping concentration n_{imp} (cm^{-2})	Spin dephasing time τ_l^* (ns)	Binding energy E_B (meV)	Transport coefficient Ξ (fs)
B	3.2×10^{10}	1.40 ± 0.05	19 ± 1	97
C	9.7×10^{10}	2.65 ± 0.05	20 ± 1	36
E	2.9×10^{11}	0.95 ± 0.05	8 ± 1	47
F	3.6×10^{11}	1.63 ± 0.05	6 ± 1	47

Table 5.1

TABLE 5.1: *Extracted parameters from the fits of the experimental data for the spin relaxation time as function of the temperature, see Figs. 5.7 and 5.9 (a). For sample F, the values are obtained considering a concentration of conduction electrons* $n_c(0) = 0.1\ n_{imp}$ *at zero temperature.*

5.5 Conclusion

In summary, in this chapter we have shown a quantitative agreement between theory and experiment for the temperature dependence of the spin relaxation time of electrons bound to donors immersed in the center of a 8-nm CdTe QW, in the 10-80K temperature range, by considering that two types of spin systems coexist and interact by spin exchange: the electrons localized on donors, and the free electrons promoted to the conduction band.

We evidenced that the spin relaxation time for the localized electrons is imposed by the same mechanisms known at low temperature (hyperfine and anisotropic exchange interactions), while the spin relaxation time of the conduction electrons is governed by the DP mechanism. For the samples in the insulating regime, we have identified that the scatterings undergone by the conduction electrons are of type I [19]. Under the same framework, we have succeeded in explaining the observed behavior *versus* temperature of the spin relaxation time for the sample with a doping concentration slightly above the Mott transition, by considering that an initial concentration of delocalized electrons exists at low temperature. The scatterings of the conduction electrons in this sample is also of type I.

5.6 Bibliography of chapter 5

[1] B. N. Murdin, K. Litvinenko, J. Allam, C. R. Pidgeon, M. Bird, K. Morrison, T. Zhang, S. K. Clowes, W. R. Branford, J. Harris, and L. F. Cohen, Phys. Rev. B **72**, 085346 (2005).
[2] R. J. Elliott, Phys. Rev. 96, 266 (1954).
[3] M. Römer, H. Bernien, G. Muller, D Schuh, J. Hubner and M. Oestreich, Phys. Rev. B **81**, 075216 (2010).
[4] J. G. Lonnemann, E. P. Rugeramigabo, M. Oestreich and J. Hubner, Phys. Rev. B **96**, 045201 (2017).
[5] P. I. Tamborenea, D. Weinman and R. A. Jalabert, Phys. Rev. B **76**, 085209 (2017).
[6] G. A. Intronati, P. I. Tamborenea, D. Winmann and R. A. Jalabert, Phys. Rev. Lett. **108**, 016601 (2012).
[7] T. Matsubara and Y. Toyozawa, Prog. Theor. Phys. **26**, 739 (1961).
[8] T. Wellens and R. A. Jalabert, Phys. Rev. B **94**, 144209 (2016).
[9] W. O. Putikka and R. Joynt, Phys. Rev. B **70**, 113201 (2004).
[10] N. J. Harmon, W. O. Putikka, and R. Joynt, Phys. Rev. B **79**, 115204 (2009).
[11] S. Ghosh, V. Sih, W. H. Lau, Apply. Phys. Letters **86**, 232507 (2005).
[12] J. M. Kikkawa and D. D. Awschalom, Phys. Rev. Lett. **80**, 4313 (1998).
[13] N. J. Harmon, W. O. Putikka, and R. Joynt, Phys. Rev. B **81**, 085320 (2010).
[14] N. F. Mott, *Metal-Insulator Transitions* (Taylor and Francis, London, 1990).
[15] P. Grinberg, F. Bernardot, B. Eble, G. Karczewski, C. Testelin, and M. Chamarro, J. Appl. Phys. **119**, 123906 (2016).
[16] J. Tribollet, E. Aubry, G. Karczewski, B. Sermage, F. Bernardot, C. Testelin, and M. Chamarro, Phys. Rev. B **75**, 205304 (2007).
[17] K.V. Kavokin, Semicond. Sci. Technol. **23**, 114009 (2008).
[18] M. I. D'yakonov and V. I. Perel', Sov. Phys. JETP **33**, 1053 (1971); Sov. Phys. Solid State **13**, 3023 (1972).
[19] J. Kainz, U. Rössler, and R. Winkler, Phys. Rev. B **70**, 195322 (2004).
[20] G. Fishman and G. Lampel, Phys. Rev. B **16,** 820 (1977).
[21] I. Zutic, Rev. of Mod. Physics **76,** 351 (2004).
[22] A. Tackeuchi, T. Kuroda, S. Muto, Y. Nishikawa, and O. Wada, Jpn. J. Appl. Phys. **38**, 4680 (1999).
[24] N. W. Aschroft and D. Mermin, Solid State Physics (Brooks-Cole, Belmont, 1976).
[25] J. Tribollet, F. Bernardot, M. Menant, G. Karczewski, C. Testelin, and M. Chamarro, Phys. Rev. B **68**, 235316 (2003).
[26] K. A. Chao, F. A. Oliveira and N. Majlis, Sol. State. Commun. **21**, 845 (1977).
[27] A. T. Neal *et al*, Appl. Phys. Lett. **113**, 062101 (2018).
[28] G. M. Castellan and F. Seitz, *Semiconducting Materials* (Butterworths, London, 1951).
[29] I. V. Osinnykh, K. S. Zhuravlev, T. V. Malin, B. Y. Ber and D. Y. Kazantsev, Semiconductors **48**, 1134 (2014).
[30] G. Fonthal, L. Tirado-Mejia, J. I. Marin-Hurtado, H. Ariza-Calderon, and J. G. Mendoza-Alvarez, J. Phys. Chem. Solids **61**, 579 (2000).

Chapter 6

Longitudinal spin relaxation time of donor-bound electrons immersed in a CdTe QW

Content

6.1 Introduction

This chapter is devoted to the study of the longitudinal spin relaxation time in samples A, C, D and E of chapter 4. Up to this work, the only studies carried out in bulk zinc-blende semiconductors are those reported by Refs. [1-6] in GaAs, CdTe and InP for different doping concentrations in the insulating regime and at low temperature. In bulk wurzite materials, a recent study has been performed by Ref. [7] in high-purity bulk ZnO.

In general, two principal challenges have been addressed in Refs. [1-7]:
(a) the development of an experimental technique that allows to measure long spin relaxation times
(b) the understanding of the principal mechanisms that dominate the longitudinal spin relaxation in presence of a longitudinal magnetic field.

Both points have been successfully overcame for high-purity direct-band-gap semiconductors by Linpeng *et al*. in Ref. [2]. In their work they measured, by means of a TRPL technique, the longitudinal spin relaxation time of donor-bound electrons as a function of the magnetic field in GaAs, InP and CdTe. The principle of the experimental technique is presented in Fig. 6.1 (a): A resonant pump pulse excites repetitively the π transition to pump electrons from the $|\uparrow\rangle$ state to the $|\downarrow\rangle$ one. After this, the system freely evolves during a variable time τ_{wait} in which the electron population returns to thermal equilibrium and the $|\uparrow\rangle$ state is repopulated. Then, a pulse resonant at the π transition probes the $|\uparrow\rangle$ state and the PL from the σ transition is detected. The experiment is repeated with different time delays τ_{wait}. An example of the PL recorded for InP is presented in Fig. 6.1 (b).

The experimental results obtained by Ref. [2] are presented in Fig. 6.1 (c). For the 3 samples, the authors observed at high magnetic fields a B^{-x} dependence of T_1 ($3 < x < 4$). For GaAs at low magnetic fields, T_1 approaches a B^2 dependence. At low magnetic field, the behavior was explained as a result of the interaction of the donor-bound electron with the nuclear environment (hyperfine interaction) in a presence of a magnetic field, while at high magnetic fields, the spin-orbit interaction [2]. For higher doping concentrations, no formal theory has been developed by Refs. [3-6].

Refs. [3,5] have principally focused their work on point (a), by modifying the techniques described in chapter 2. In Ref. [3], by the inclusion of additional pump and probe pulses, an extended version of the TRPL technique was developed. This technique, that allows to measure times of the order of microsecond, uses 4 pulses (see Fig. 6.2): two pump pulses (σ^+ and σ^- polarized) that create the spin polarization in the sample and two probe pulses that detect the PL coming from each pump pulse. The available delay between each pair of pulses is up to 20 microseconds. The PL is collected with a double-grating spectrometer and measured with a two-channel photon counter: σ^+ and σ^- are separately recorded.

As already remarked, one of the main limitations imposed by the usual PFR technique, described in chapter 2, is the restricted time range that can be explored due to the finite length of mechanical delay lines. To overcome this restriction, in Ref. [5] they developed an extended PFR technique. The physical principle of this technique is the same as the

usual one, the novelty is that the pump-probe delay is controlled electronically. Figure 6.3 shows the experimental set-up developed by Ref. [5]: an electro-optic and an acousto-optic modulator are used to produce trains of pulses for the pump beam and single pulses for the probe beam; the delay between them is controlled electronically. With this technique, they measured the longitudinal spin relaxation time for donor-bound electrons in GaAs at different doping concentrations in the insulating regime. A scheme of this experimental technique is presented in Fig. 6.3

In this chapter, we have focused our efforts on point (a), developing an extended PFR technique according to the set-up proposed by Ref. [5]. With this technique, we measured the longitudinal spin relaxation time T_1 for donor-bound electrons immersed in the middle of a CdTe QW for different doping concentrations, in the microsecond regime with a 0.03 μs time resolution.

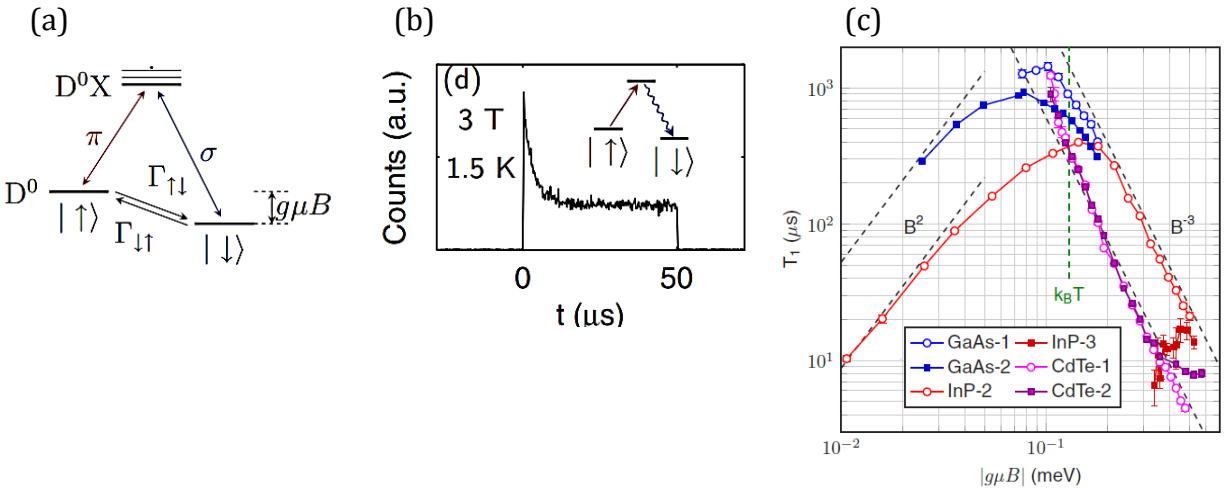

Figure 6.1 *Figure taken from [2]: (a) energy level diagram for the donor system, (b) PL recorded for bulk InP. The amplitude of the signal is proportional to the $|\uparrow\rangle$ population. (c) Longitudinal spin relaxation time T_1 for electrons bound to donors, in high-purity bulk GaAs, InP and CdTe, versus Zeeman energy $g\mu_B B$.*

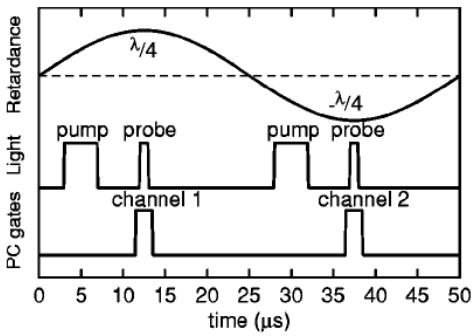

Figure 6.2 *Figure taken from [3]: principle of a TRPL technique with pump-probe pulses.*

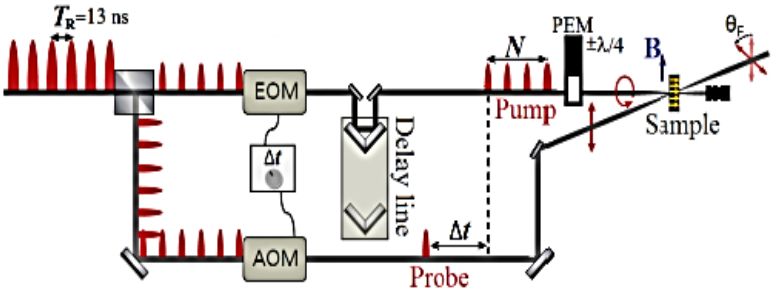

Figure 6.3 *Figure taken from [5]: scheme of the extended PFR experiment. The delay between the pump train and the probe pulse is generated electronically.*

6.2 Development of an extended PFR technique

In this section, we describe the extended PFR technique developed to measure spin relaxation times in the microsecond regime. A scheme of the experimental set-up is presented in Fig. 6.4.

The light source is a Ti: sapphire laser (*Coherent Mira*) optically pumped with a continuous laser *Verdi* (532 nm, 15 W), emitting 2-ps pulses with a repetition rate of 76 MHz (repetition period $T_R = 13.1\,ns$). The divergence of the laser is corrected by focusing the principal beam with a 2-mm focal lens on a pinhole of 50 micrometers of diameter and then collimated by a 40-mm focal lens.

The laser output is split into pump and probe beams using a beam splitter (70/30). In the pump path, an electro-optic modulator (EOM) selects trains of N pulses separated by T_R, with arbitrary long delay between the trains. The time width of each train $w_{pump} = NT_R$ can be chosen. The acousto-optic modulator (AOM) is used in the probe path for the same purpose. The time delay between a train produced by the EOM and one produced by the AOM is controlled electronically, allowing a large change of the delay between the pump trains and the probe ones.

In this experimental set-up, the EOM is controlled in such a way to produce linearly-polarized pump trains. The polarization direction is fixed by a polarizer set at the exit of the EOM; this direction is at 45° to the neutral axes of a photo-elastic modulator (PEM). The PEM is used to modulate the polarization of the pump beam between σ_+ and σ_- at a frequency of 50 kHz, to avoid nuclear spin polarization in the samples (see section 2.3.2).

In order to perform synchronous detection (see section 2.3.4), the intensity of the probe beam is modulated with an optical chopper, at $f_{probe} = 500$ Hz. The signal given by the optical bridge is then modulated at two frequencies $f_{pump} = 50$ kHz and $f_{probe} = 500$ Hz.

The limitation in time range of this technique is imposed by the modulation frequency of the PEM. Since its period of modulation is 20 microseconds, the maximum temporal window is then 3 microseconds (in order to average at least on 3 trains of the pump-beam over half a period of the PEM).
The minimum temporal window is 30 ns (being limited by the time width of the trains). Figure 6.5 shows the optical trains obtained when the EOM and the AOM are driven by 100 ns electronic gates: around N = 8 picosecond pulses are present in the trains; the delay between the probe and pump trains can be swept at will (within the 3μs window).

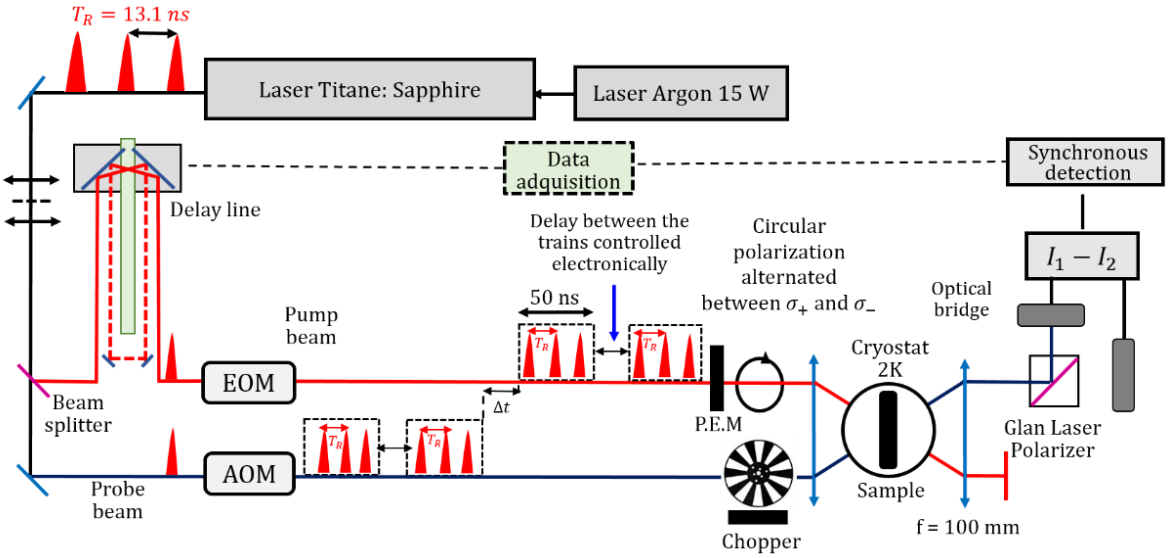

Figure. 6.4 *Scheme of the extended PFR technique. The time width of the trains, and the delay between the pump and probe trains are controlled electronically. The width for the trains shown in the figure is 50 ns (3 pulses). A magnetic field B is applied in Faraday geometry (not shown).*

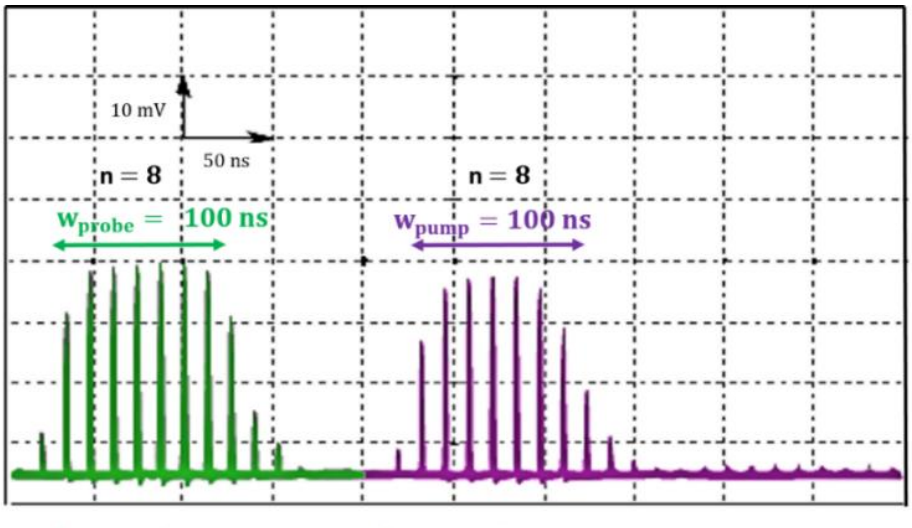

Figure 6.5 *Pump and probe 100-ns optical trains delayed by 100 ns. Each train contains around 8 pulses separated by the repetition period of the laser, 13.1 ns. (The time width of each pulse is limited by the bandwidth of the used photodiode)*

6.3 Experimental results.

In figure 6.6, we present the longitudinal electron spin relaxation measured for the samples A, C, D and E. As usual, the laser wavelength was set to the D^0X transition of each sample indicated by its PL spectrum performed at T = 10 K (see chapter 4, Fig. 4.2). Here we used a power of excitation of 3 mW for the pump beam and 60 microwatts for the probe beam. The widths of the trains, and the needed temporal window chosen for each sample, are indicated in the corresponding figure captions. One of the principal difficulties faced during the measuring process on the samples is the very low level of signal; especially for the heavily doped sample E, the signal was hardly detectable. In order to keep a detectable level of signal, the widths of the gates have been increased only when a longer temporal window was needed.

Figures 6.6 shows that the application of a longitudinal magnetic field slows down the spin dynamics in the studied samples. The signal in Fig. 6.6 can be described by a double exponential decay with a fast and a slow component. The fast component observed corresponds to the overlapping at t = 0 of the pump and probe trains. In Refs. [5,6] they identified a fast component, no related with this overlapping, due to the use of single probe pulses. For our samples, trains of probe pulses are needed to increase the level of the signal.

As it has been observed in bulk GaAs, CdTe and InP [2], residual doped samples show longer spin relaxation times: for sample A at a magnetic field of B = 0.08 T (Fig. 6.6 (a)) the measured time of $T_1 \sim 10\mu s$, reaches the maximum relaxation time than can be measured with our experimental set-up.

For the sample with an intermediate doping concentration, sample C, we observe a continuous increase of the spin relaxation time with the applied magnetic field. For samples D and E, there is first an increase and after a decrease of the relaxation time in the same range of magnetic fields. Figure 6.7 gathers the measured spin relaxation times, for the different samples, as function of the Zeeman splitting energy. As the concentration is increased, the maximum measured T_1 decreases.

Table 6.1 gathers the values of the magnetic field B_{max} at which the measured longitudinal spin relaxation time is maximum, for samples A, C, D and E.

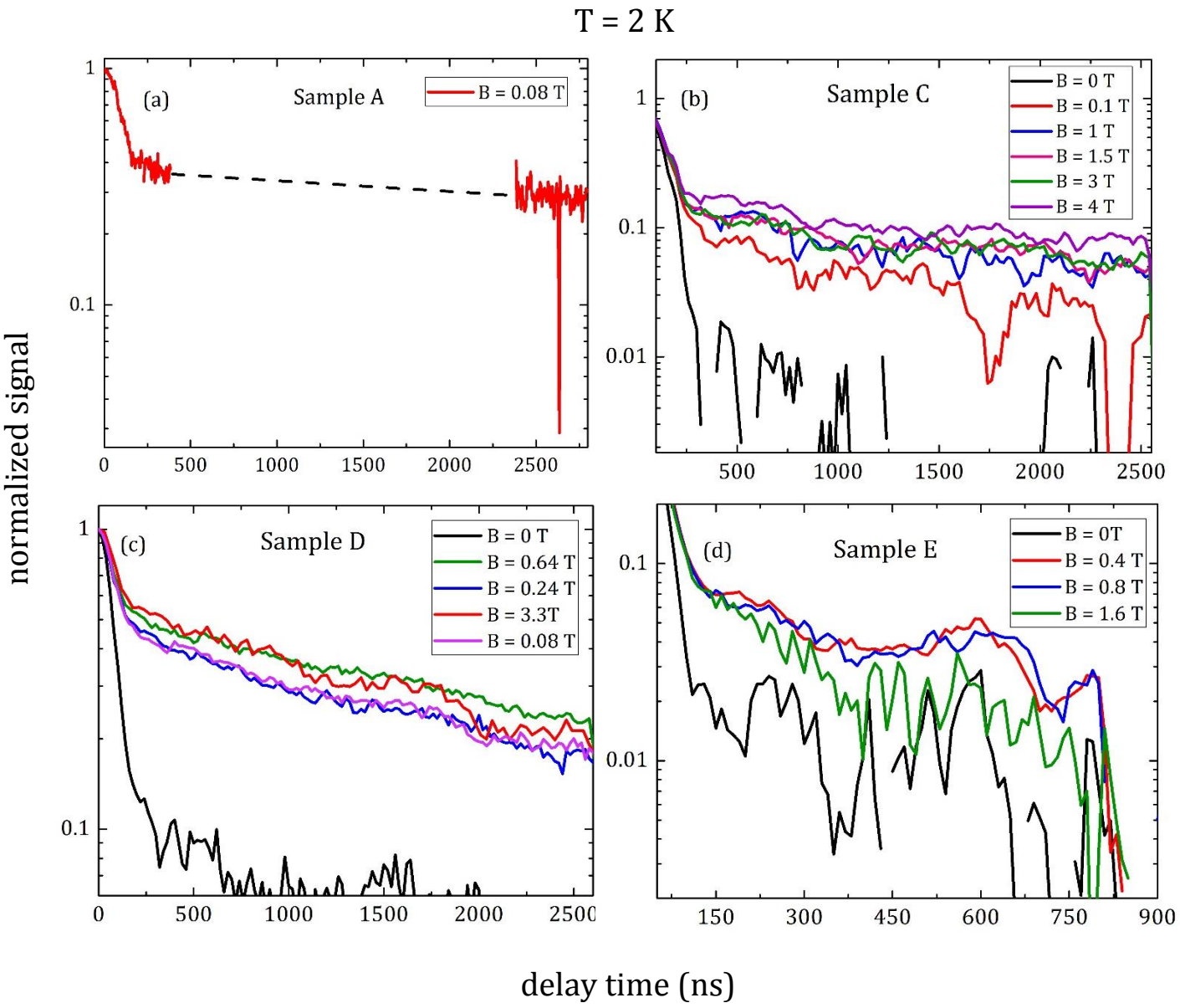

Figure 6.6 *Longitudinal spin signal versus time of the donor-bound electrons, in samples A, C, D, E in different applied magnetic fields. The width of the trains for the pump and probe beams ($w_{pump,probe}$) and the time windows are: (a) w_{pump}= 100 ns, w_{probe}= 50 ns, window = 1 μs ; (b) w_{pump}= w_{probe}= 150 ns, window = 3μs; (c) w_{pump}= w_{probe}= 100 ns, window = 3μs ; (d) w_{pump}= w_{probe}= 60 ns, window = 1μs.*

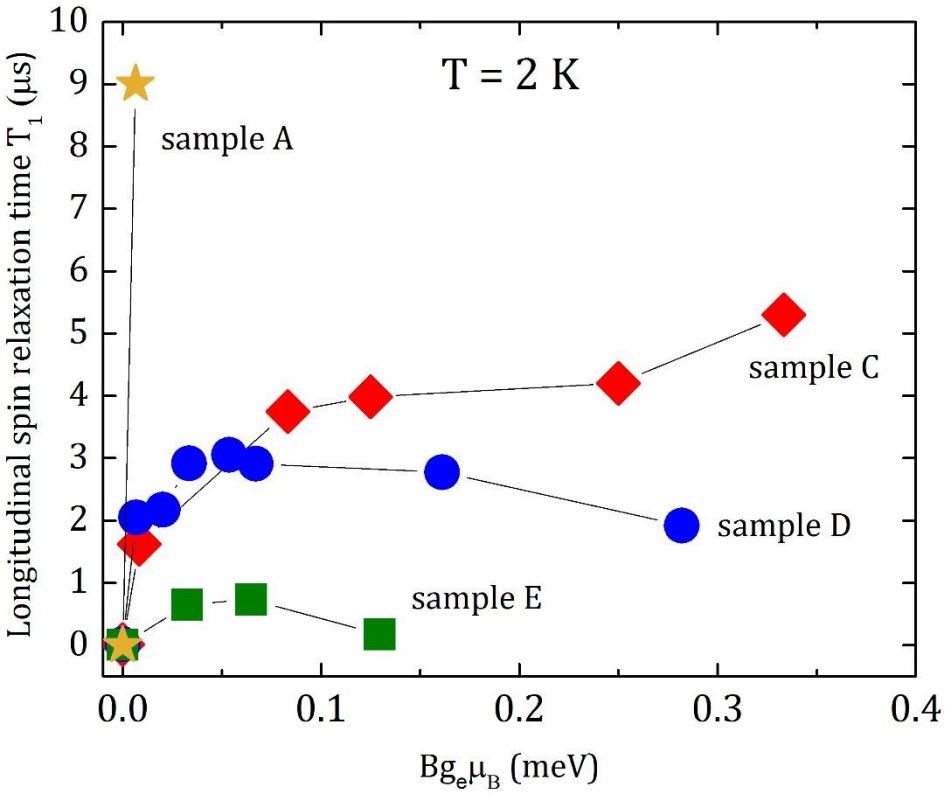

Figure 6.7 *Longitudinal spin relaxation time T_1 as a function of the Zeeman splitting energy, for samples A, C, D and E.*

Sample	Doping concentration (donors/cm^2)	Electron Landé factor $g_e^{\perp}$	B_{max} (T)	$T_{1,max}$ (μs)
A	1×10^9	1.39	0.08	~9
C	9.7×10^{10}	1.44	4.0	5.0
D	1.6×10^{11}	1.45	0.64	3.0
E	2.9×10^{11}	1.40	0.8	0.7

Table 6.1 *Magnetic field and maximum longitudinal spin relaxation time measured for samples A, C, D and E.*

6.4 Discussion of the results

In this section, we compare the results obtained for samples A, C, D and E with the available experimental data reported in bulk GaAs.

6.4.1 Comparison with bulk semiconductor results

In the insulating regime, at low temperature, the longest spin relaxation times have been measured in high-purity bulk semiconductors by Linpeng *et al*. [2]: 3×10^{13} cm^{-2} for GaAs, 2.3×10^{14} cm^{-3} for InP and 1×10^{14} cm^{-3} for CdTe (see Fig. 6.1 (c)).

Similarly we observe that sample A, with a residual doping concentration, exhibits the longest spin relaxation time $T_1 \sim 9\,\mu s$ at the energy $g_e \mu_B B = 0.006$ meV. This value is larger than $T_1 = 3\,\mu s$ reported in Ref. [6] for bulk GaAs with a residual doping concentration of $n_d = 5.5 \times 10^{14} cm^{-3}$, at the same Zeeman splitting energy (see Fig. 6.8 (a), B = 0.2 T). For bulk CdTe, there is no reported value in Ref. [2], at the same Zeeman energy.

For intermediate doping concentrations in bulk GaAs, the available experimental data are from Refs. [3,4,6]. The samples studied by Refs. [3,4] consisted in a $1\mu m$-thick GaAs layer in an AlGaAs heterostructure, containing a doping concentration of $n_d = 1 \times 10^{15}$ cm^{-3} and $n_d = 3 \times 10^{15}$ cm^{-3}. The results are shown in Fig. 6.8. The sample studied by Ref. [6] consisted in a $20\mu m$ thick GaAs layer, with a doping concentration of $n_d = 1 \times 10^{15}$ cm^{-3}. The results are presented in Fig. 6.9 (b).

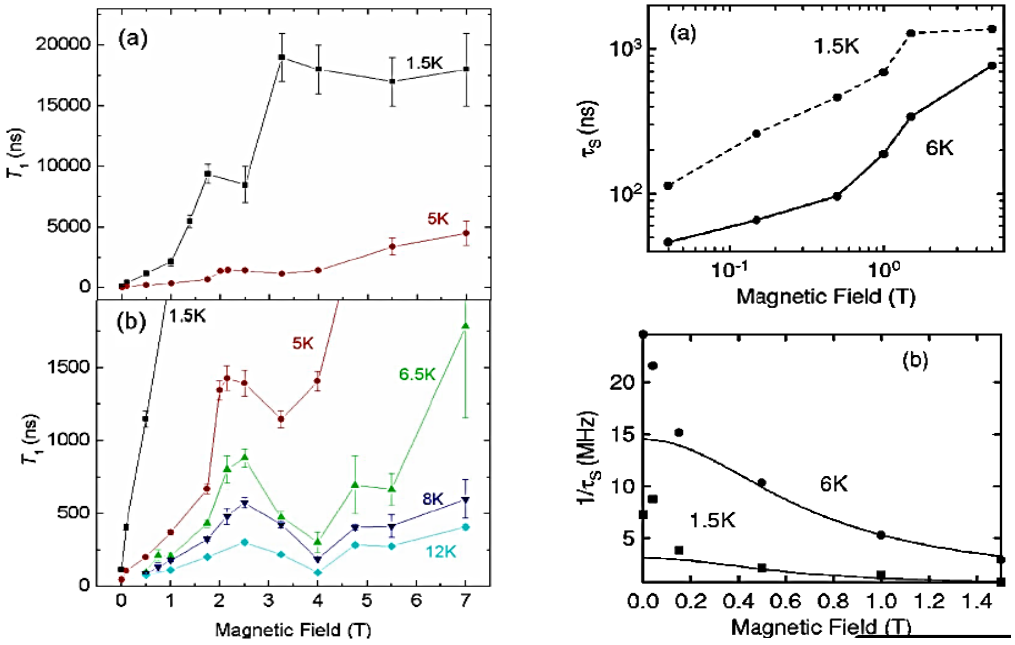

Figure 6.8 *Figures taken from [3,4]: T_1 relaxation time of electrons bound to donors in bulk GaAs, with a doping concentration of $n_d = 1 \times 10^{15}$ (left) and $n_d = 3 \times 10^{15} cm^{-3}$ (right), versus magnetic field [on the right, Fig. (b) is the relaxation rate].*

As can be seen in Fig. 6.8, the sample with a concentration of $n_d = 1 \times 10^{15}\text{cm}^{-3}$ (left column), shows a longitudinal spin relaxation time of $T_1 = 17\ \mu s$ at B = 6 T and T = 1.5 K. In Ref. [6], for the same concentration of donors (see Fig. 6.9 (b)) the spin relaxation time shows a maximum relaxation time $T_{1,max}$ = 1 μs at B_{max} = 1 T, and after a decrease to hundreds of nanoseconds at $B = 6$ T. Therefore, the spin relaxation times measured by V. V. Behlyk *et al*. [6] are shorter than the ones reported by Colton *et al*. [4]. The origin of this discrepancy is probably the different experimental conditions used in each case: in Ref. [4] the energy of excitation is fixed above the band gap, as has been already discussed in chapter 4, this produces faster-relaxing free carriers that shortens the spin relaxation time due to the interaction with localized electrons, while in Ref. [6] the excitation is done at the D^0X transition energy.

For the sample with a concentration of $n_d = 3 \times 10^{15}\text{cm}^{-3}$ (right column of Fig. 6.8), the maximum relaxation time measured is $T_{1,max} = 1.4\ \mu s$ at B_{max} = 5 T .

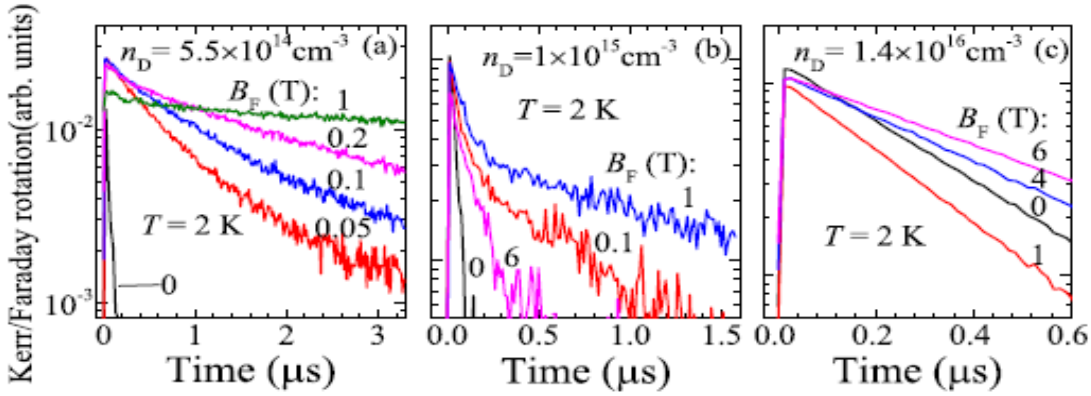

Figure 6.9 *Figures taken from [6]: T_1 spin relaxation time of electrons bound to donors in bulk GaAs with different doping concentrations (indicated on the figures), at different magnetic fields.*

The measured times reported by Refs. [2-6] are listed in Table 6.2. We remark that samples C and D, with an intermediate doping concentration, show a longer longitudinal spin relaxation time than samples studied in Ref. [4] and Ref. [6] (see tables 6.1 and 6.2)

For samples with a doping concentration next to the MIT (see Fig. 6.10), the available experimental data belongs to Ref. [5]. In this reference, the authors measured at low temperature, the longitudinal spin relaxation time T_1 in the range 0 -6T, for bulk GaAs. At low magnetic field they found a T_1 of the order of 260 ns, which increases up to $T_{1,max}$ = 450 ns at B_{max} = 6 T. Sample E with a doping concentration next to the MIT exhibits a longer $T_{1,max}$ (700 ns) than the one reported by Ref. [6].

Reference	n_d (donors/cm^3)	B_{max} (T)	$T_{1,max}$ (μs)
Linpeng *et al.* [2]	3×10^{13}	4	1400
V. V. Belykh *et al.* [6]	5.5×10^{14}	1	~10
Colton *et al.*, [3]	1×10^{15}	3	19
Colton *et al.*, [4]	3×10^{15}	6	1.4
V. V. Belykh *et al.* [6]	1×10^{15}	1	1
V. V. Belykh *et al.* [5]	1.4×10^{16}	6	0.45

Table 6.2 *Maximum longitudinal spin relaxation time reported for different doping concentrations in bulk GaAs in the insulating regime.*

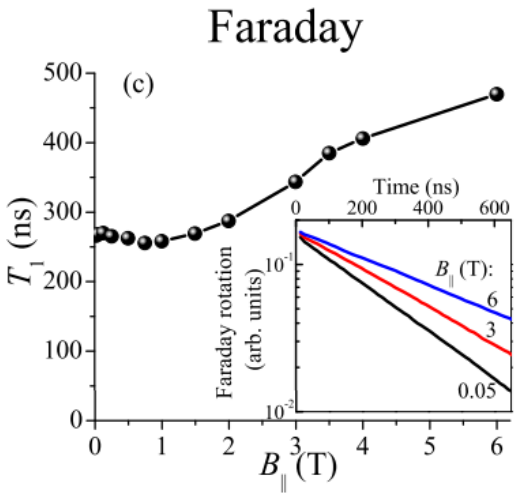

Figure 6.10 *Figure taken from [5]: T_1 spin relaxation time of electrons bound to donors in bulk GaAs with a doping concentration close to the MIT $n_d = 1.4 \times 10^{16} cm^{-3}$, at different magnetic fields.*

6.4.2 Magnetic field dependence of T_1.

Up to know, there is no unified model that explains the magnetic field dependence of T_1 at a given doping concentration and for any magnetic field, either in bulk or QWs.

In high-purity bulk semiconductors, the increase of the spin relaxation time at moderate magnetic fields has been explained by the suppression of the hyperfine interaction [2,9], while at high magnetic fields, the decrease of the spin relaxation time observed by Linpeng *et al*. [2] (see Fig. 6.1 (c)) is induced by the spin-orbit interaction and phonons following a B^{-x} law.

The role of the hyperfine interaction has particularly been discussed by Yao *et al*. [10], for the long time range. In this range, the spin relaxation time is induced by an inhomogeneous hyperfine coupling of the electron spin with the fluctuating nuclear spins. The fluctuation of the nuclear spin is induced by two different processes:

- the second-order hyperfine interaction which couples two nuclei via the same electron.
- the nuclear dipole interaction.

The first process is dominant at low magnetic field and it can be screened by a longitudinal magnetic field. The second process is less sensitive to B and could fix a maximum value of the spin relaxation time depending on the material and its intrinsic parameters.

In a semiconductor QW the magnetic field dependence of T_1 has been treated theoretically by Refs. [11,12] considering hopping diffusion. This model is based on the idea that the ensemble of localized electrons is grouped in small clusters, inside of which an electron is coupled with the rest of the donor-bound electrons by isotropic exchange. but it also may visit other clusters by hopping diffusion. In this references the spin relaxation time is calculated considering the hyperfine interaction and spin-orbit interaction (no dipole-dipole interaction is considered). We discard this model, since it is related to a hopping time which is still to be defined and determined in our system.

6.5 Conclusion

In this chapter we have measured the longitudinal spin relaxation measurements for donor-bound electrons in a CdTe semiconductor, by means of an extended PFR rotation technique. Our experiment brought the first results of this kind in a CdTe QW. For any doping concentration, we have observed an increase of the spin relaxation time when a magnetic field is applied. Particularly, the longest longitudinal relaxation time is for a residual doping concentration as it has been observed in previous references for other compounds. More theoretical studies are needed in order to understand the mechanisms that govern the longitudinal spin relaxation at any doping concentration.

6.6 Bibliography of chapter 6

[1] K. C. Fu, W. Yeo, S. Clark, C. Santori, C. Stanley, M. C. Holland, and Y. Yamamoto, Phys. Rev. B **74**, 121304(R) (2006).
[2] X. Linpeng, T. Karin, M. V. Durnev, R. Barbour, M. M. Glazov, E. Ya. Sherman, S. P. Watkins, S. Seto, and K. C. Fu, Phys. Rev. B **94**, 125401 (2016).
[3] J. S. Colton, T. A. Kennedy, A. S. Bracker, and D. Gammon, Phys. Rev. B **69**, 121307(R) (2004).
[4] J. S. Colton, M. E. Heeb, P. Schroeder, A. Stokes, L. R. Wienkes, and A. S. Bracker, Phys. Rev. B **75**, 205201 (2007).
[5] V. V. Belykh, E. Evers, D. R. Yakovlev, F. Fobbe, A. Greilich, and M. Bayer, Phys. Rev. B **94**, 241202(R) (2016).
[6] V. V. Belykh, K. V. Kavokin, D. R. Yakovlev, and M. Bayer, Phys. Rev. B **96**, 241201(R) (2017).
[7] X. Linpeng, M. L.K. Viitaniemi, A. Vishnuradhan, Y. Kozuka, C. Johnson, M. Kawasaki, and K.M. C. Fu, Phys. Rev. Applied **10**, 064061 (2018).
[8] Colton et al., Phys. Stat. Sol. (b) **233**, 445 (2002).
[9] M. M. Glazov, Phys. Rev. B **91**, 195301 (2015)
[10] W. Yao, R. B. Liu, and L. J. Sham, Phys. Rev. B **74**, 195301 (2006).
[11] I. S. Lyubinskiy, Pis'ma ZhETF **88**, 934 (2008).
[12] K.V. Kavokin, Semicond. Sci. Technol. **23**, 114009 (2008).

Conclusions and perspectives

This thesis has been devoted to study the spin relaxation time of donor-bound electrons immersed in a CdTe quantum well of thickness $L = 8$ nm, by means of a photo-induced Faraday and Kerr rotation techniques. We have experimentally studied three of the main variables that influences the spin relaxation time: doping concentration, temperature and longitudinal magnetic field.

One of the first principal results obtained in this work, is the theoretical determination of the exchange energy of two electrons-bound to donors placed in the middle of an infinite QW. The exchange energy determines the residence time of an electron-bound to a donor, which is fundamental to define the spin relaxation mechanisms in a doped semiconductor, in this sense its knowledge is of prime importance. The obtained expression is written in units of effective Hartree, and the distance between the donors is in units of effective Bohr radius, it can be then applied for any direct-band gap semiconductor QW of thickness L. In comparison with bulk systems, we have found that in the low doping regime, the electron exchange energy in a QW, J_{QW}, is smaller than in bulk: $J_{QW} < J_{3D}$, while for high doping concentrations the situation is reversed: $J_{QW} > J_{3D}$. Because we consider an infinite QW with a wave-function completely confined in the QW, our calculations do not describe systems for L < a_B^{*3D}. Indeed, the electron wave-function of thin QWs overflows the barrier material which does not represent an infinite barrier for electrons.

By using a photo-induced Faraday rotation technique, we have measured the spin relaxation time of donor-bound electrons for different doping concentrations at low temperature in the insulating regime. A non-monotonous behavior is observed and it is successfully explained by the interplay of two mechanisms, as in GaAs: hyperfine interaction and anisotropic exchange interaction, being the hyperfine interaction the dominant mechanism at low doping and the anisotropic exchange interaction at high doping concentration. From the fit of the experimental data we determined the CdTe

spin-orbit constant: α_{so} = 0.079, which is in good agreement with previous theoretical calculations.

According with the spin relaxation mechanisms identified here, we have predicted that the spin relaxation time in bulk is always longer than in a QW, nevertheless the reported experimental values by Sprinzl *et. al*. [1] in bulk CdTe, are very small compared with those predicted by the theory and also with our experimental values. We concluded that the experimental conditions used by Ref. [1]: femtosecond pulses tuned at the band gap energy and a concentration of photo-excited carriers comparable with the nominal one, are at the origin of the observed shortening of spin relaxation time.

The results of the experimental study of the spin relaxation time in the range 10-80K, by means of photo-induced Kerr rotation technique, were successfully explained by invoking spin exchange between electron spins localized on donors and the spin of electrons promoted to conduction states. For the whole range of the studied doping concentrations, we demonstrated that, while the spin of localized electrons undergoes the effect of both hyperfine and anisotropic exchange interactions, the D'yakonov-Perel' mechanism governs the spin relaxation of the conduction electrons. Moreover, we have identified that the scatterings undergone by the conduction electrons are of type I [2]. We also demonstrated that the contribution of the Elliot Yafet mechanism to the spin relaxation time can be neglected. In particular, for the sample with a doping concentration slightly beyond the Mott transition, we found that the experimental data on this sample could *not* be fitted by considering only a population of conduction electrons and a dephasing time related to DP or/and EY mechanisms. In order to explain the spin dephasing time we considered that at very low temperature a fraction *f* of the doping concentration n_{imp} it is already in the conduction band. A successful agreement between theory and experimental data was found.

Finally, we developed a new experimental set-up able to explore relaxation times in the microsecond regime. With this technique we have measured by first time the longitudinal spin relaxation time T_1 of donor-bound electrons immersed in the middle of a CdTe QW, for different doping concentrations as a function of a longitudinal magnetic field. From the observed experimental behavior, residual doped QW's appears as suitable candidates to obtain long spin relaxation times. The theory developed so far, shows that in high-purity-zinc-blende semiconductors the suppression of the hyperfine interaction is at the origin of the observed increased of T_1 at low magnetic fields, while at high magnetic fields the spin orbit interaction and phonons explain a decrease of the spin relaxation time with a B^{-x} dependence. More studies must be carried out in order to explain the non-monotonous behavior of the longitudinal spin relaxation time for higher doping concentrations.

In summary, this work presents a fundamental study of the three main variables that influence the spin relaxation time in a semiconductor CdTe QW: doping concentration, temperature and longitudinal spin relaxation time. From this study we conclude that residual doped CdTe QWs are suitable candidates for obtaining long longitudinal spin relaxation times. In addition, we propose a zinc-blende II-VI material: bulk ZnSe and a

wurtzite material: bulk ZnO as promising candidates for obtaining long spin relaxation times at low temperatures.

REFERENCES

[1] D. Sprinzl, P. Horodyská, N. Tesarová, E. Rozkotová, E. Belas, R. Grill, P. Malý, and P. Nemec, Phys. Rev. B **82**, 153201 (2010).
[2] J. Kainz, U. Rössler, and R. Winkler, Phys. Rev. B **70**, 195322 (2004).

Appendix A

Proof of $T_1 = T_2$ for a vanishing magnetic field

In this appendix, we argue that in absence of magnetic field, the longitudinal spin relaxation time T_1 is equal to the transversal relaxation time T_2.

Let's consider a two-level system of spin ½ under a vanishing magnetic field $\vec{B}_x \to 0$. The density matrix elements can be expressed in the x-basis as

$$\rho^x_{\uparrow\uparrow}(t) = \frac{1}{2} + ae^{-t/T_1} \tag{A.1}$$

$$\rho^x_{\downarrow\downarrow}(t) = \frac{1}{2} - ae^{-t/T_1} \tag{A.2}$$

$$\rho^x_{\uparrow\downarrow}(t) = \rho^x_{\uparrow\downarrow}(0)e^{-t/T_2} \tag{A.3}$$

with $|a| < \frac{1}{2}$. A factor $e^{i\omega t}$ with $\omega = g\mu_B B/\hbar$ should appear in equation (A.3), but since $B \to 0$ then $e^{i\omega t} \to 1$: the dynamics of the coherence $\rho^x_{\uparrow\downarrow}(t)$ is dominated by the decay with the characteristic time T_2. Both populations relax towards the value ½, with the characteristic time T_1.

If we write now these elements in the z-basis, using the change of basis:

$$|\uparrow x\rangle = \frac{1}{\sqrt{2}}(|\uparrow z\rangle + |\downarrow z\rangle) \tag{A.4}$$

$$|\downarrow x\rangle = \frac{1}{\sqrt{2}}(|\uparrow z\rangle - |\downarrow z\rangle), \tag{A.5}$$

we get

$$\rho^z_{\uparrow\uparrow}(t) = \frac{1}{2} + \mathcal{R}e\{\rho^x_{\uparrow\downarrow}(0)\}e^{-t/T_2} \tag{A.6}$$

$$\rho^z_{\downarrow\downarrow}(t) = \frac{1}{2} - \mathcal{R}e\{\rho^x_{\uparrow\downarrow}(0)\}e^{-t/T_2} \tag{A.7}$$

$$\rho^z_{\uparrow\downarrow}(t) = ae^{-t/T_1} + i\, Im\,\{\rho^x_{\uparrow\downarrow}(0)^*\}e^{-t/T_2}. \tag{A.8}$$

In the limit $\vec{B}_x \to 0$, the bases ($|\uparrow x\rangle, |\downarrow x\rangle$) and ($|\uparrow z\rangle, |\downarrow z\rangle$) play the same role, since there is no designated quantization axis. Then, the comparison of Eqs. (A.1) and (A.2) with Eqs. (A.6) and (A.7) shows that $T_2 = T_1$ for a vanishing magnetic field.

Appendix B

$1s$ and $2s$ hydrogenic states centred in an infinite quantum well

1. Method

A positive electric charge Ze (e: elementary charge) is at the origin of Cartesian coordinates xyz. The Hamiltonian H of an electron (charge $-e$) in the Coulomb potential of Ze is

$$H = -\frac{\Delta}{2} - \frac{Z}{r} , \tag{B. 1}$$

where Δ is the Laplacian operator and r is the distance of the electron to the origin. The distances are expressed in units of effective (bulk) Bohr radius a_B^{*3D}, and energies in units of effective hartree E_h^{*3D} (for definitions of a_B^{*3D} and E_h^{*3D}, see eq. (3.2) of chapter 3).

The $1s$ and $2s$ states in bulk ($r = \sqrt{x^2 + y^2 + z^2}$) or in $2D$ ($\rho = \sqrt{x^2 + y^2}$) are known [1]. They are presented in the following Table B.1.

		Wavefunction ϕ	Energy E
3D	1s	$\frac{1}{\sqrt{\pi}} Z^{3/2} \exp(-Zr)$	$-Z^2/2$
	2s	$\frac{1}{2\sqrt{2\pi}} Z^{3/2} \exp(-Zr/2)\,[1-Zr/2]$	$-Z^2/8$
2D	1s	$\frac{4}{\sqrt{2\pi}} Z \exp(-2Z\rho)$	$-2Z^2$
	2s	$\frac{4}{3\sqrt{6\pi}} Z \exp(-2Z\rho/3)\,[1-4Z\rho/3]$	$-2Z^2/9$

Table B.1 *Wavefunctions and energies for the 1s and 2s hydrogenic states in 3D and 2D.*

We seek the $1s$ and $2s$ states when the charge Ze is placed in the middle of a QW of thickness L, simply modeled by two infinite barriers located at $z = \pm L/2$; the confinement potential is supposed to be zero inside the QW ($|z| < L/2$). The $1s$ and $2s$ wavefunctions centred within this QW are taken in the following forms:

$$\phi_1(\rho, z) = A_1 \exp(-\alpha_1 r) \cos\left(\pi \frac{z}{L}\right), \tag{B. 2a}$$

$$\phi_2(\rho, z) = A_2 \exp(-\alpha_2 r)\,[1-\alpha_3 r] \cos\left(\pi \frac{z}{L}\right), \tag{B. 2b}$$

where $r = \sqrt{\rho^2 + z^2}$. The postulated $\cos(\pi z/L)$ envelope function is a single sinusoid arch, and ensures that the wavefunctions $\phi_j(\rho, z)$, $j = 1$ or 2, vanish at the boundaries of the QW. The dependences on r of both ϕ_j respect the ones which are met in the $2D$ ($L \to 0$) and $3D$ ($L \to \infty$) limits. In the following of this Appendix, the prefactors A_j are fixed by normalization; $\phi_1(\rho, z)$ and its energy E_1 are first determined by means of the variational method; afterwards, using the $2s$-$1s$ orthogonality and the variational method, $\phi_2(\rho, z)$ and its energy E_2 are obtained.

2. 1*s* state

The normalization condition of the $\phi_1(\rho, z)$ wavefunction: $\int_{|z|<\frac{L}{2}} 2\pi\rho\, d\rho\, dz \phi_1(\rho, z)^2 = 1$, gives:

$$A_1^2 = \frac{\alpha_1^3}{\pi\, N(\alpha_1 L)}, \tag{B. 3a}$$

$$\text{with} \quad N(X) = 1 - \frac{\pi^2}{X^2+\pi^2} + \frac{\pi^4/2}{[X^2+\pi^2]^2} - \frac{\pi^2}{4}\left(\frac{X+4}{X^2+\pi^2} - \frac{2\pi^2}{[X^2+\pi^2]^2}\right) e^{-X}. \tag{B. 3b}$$

Here, and in all the following calculations, we exploited the even parity of the integrand with respect to z. The integration over ρ is first performed with the change of variable $r = \sqrt{\rho^2 + z^2}$, z = cte (ρdρ = rdr), r varying from $r = z\ (> 0)$ to $r = +\infty$; the integration over z is then performed, from $z = 0$ to $z = L/2$.

The forms of the normalization factors of the $3D$ and $2D$ $1s$-wavefunctions can be retrieved from expressions (B.3): $A_1 \to \alpha_1^{3/2}/\sqrt{\pi}$ for $L \to \infty$, and $A_1\sqrt{L/2} \to \alpha_1\sqrt{2/\pi}$ for $L \to 0$.

The parameter α_1 is obtained by minimization of the mean energy $\tilde{E}_1 = \langle\phi_1|H|\phi_1\rangle$, which is the sum of a kinetic term (possessing, after calculation, a remarkably simple form):

$$\left\langle\phi_1\left|-\frac{\Delta}{2}\right|\phi_1\right\rangle = \frac{\alpha_1^2}{2} + \frac{\pi^2}{2L^2}\ , \tag{B. 4}$$

and a potential term due to the Coulomb interaction:

$$\left\langle\phi_1\left|-\frac{Z}{r}\right|\phi_1\right\rangle = -Z\,\alpha_1\,\frac{C(\alpha_1 L)}{N(\alpha_1 L)}\ , \tag{B. 5a}$$

$$\text{with} \quad C(X) = 1 - \frac{1}{2}\frac{\pi^2}{X^2+\pi^2}(1 + e^{-X})\,. \tag{B. 5b}$$

Defining $g(X) = XC(X)/N(X)$, which is a smooth function close to the identity [$g(X) \approx X$], the minimum of $\tilde{E}_1$ is found to be reached when α_1 is solution of the equation

$$\frac{\alpha_1 L}{g'(\alpha_1 L)} = Z\,L\,. \tag{B. 6}$$

After a numerical determination of the derivative $g'(X)$ of the function $g(X)$, the left-hand side of the above equation can be calculated for a value of the parameter $\alpha_1 L$. One then obtains the thickness L for which the starting parameter $\alpha_1 L$ corresponds to the minimum of $\tilde{E}_1$; finally, the associated α_1 value is calculated through $\alpha_1 = (\alpha_1 L)/L$, and the energy E_1 of ϕ_1 by substitution of this α_1 in the expression for $\tilde{E}_1$. The procedure can be repeated for any starting parameter $\alpha_1 L$, and then allows to get α_1 and E_1, and also A_1, as a function of the thickness L of the QW, as shown in Fig. B1 for $Z = 1$ and $Z = 2$. One can remark that parameter $\alpha_1(Z = 1)$ for thickness L coincides with $\alpha_1(Z)/Z$ for ZL. The prefactor A_1 goes to $\sqrt{Z^3/\pi}$ ($3D$ limit) for $L \gg 1$, and behaves as $4Z/\sqrt{\pi L}$ for very small L [see Figs B1(a) and (b)]. The parameter α_1 goes to Z ($3D$ limit) for $L \gg 1$, and to $2Z$ ($2D$ limit) for vanishing L [see Figs B1(c) and (d)]. For decreasing values of L, the extension of the ϕ_1 wavefunction first inflates slightly in the xy plane (α_1 becoming a little smaller than Z), and secondly globally shrinks for smaller values of L. The energy E_1, when considered by reference to the confinement energy $E_{conf.} = \pi^2/2L^2$, increases monotonically with L from $-2Z^2$ ($2D$ value) to $-Z^2/2$ ($3D$ value) [see Figs B1(e) and (f)].

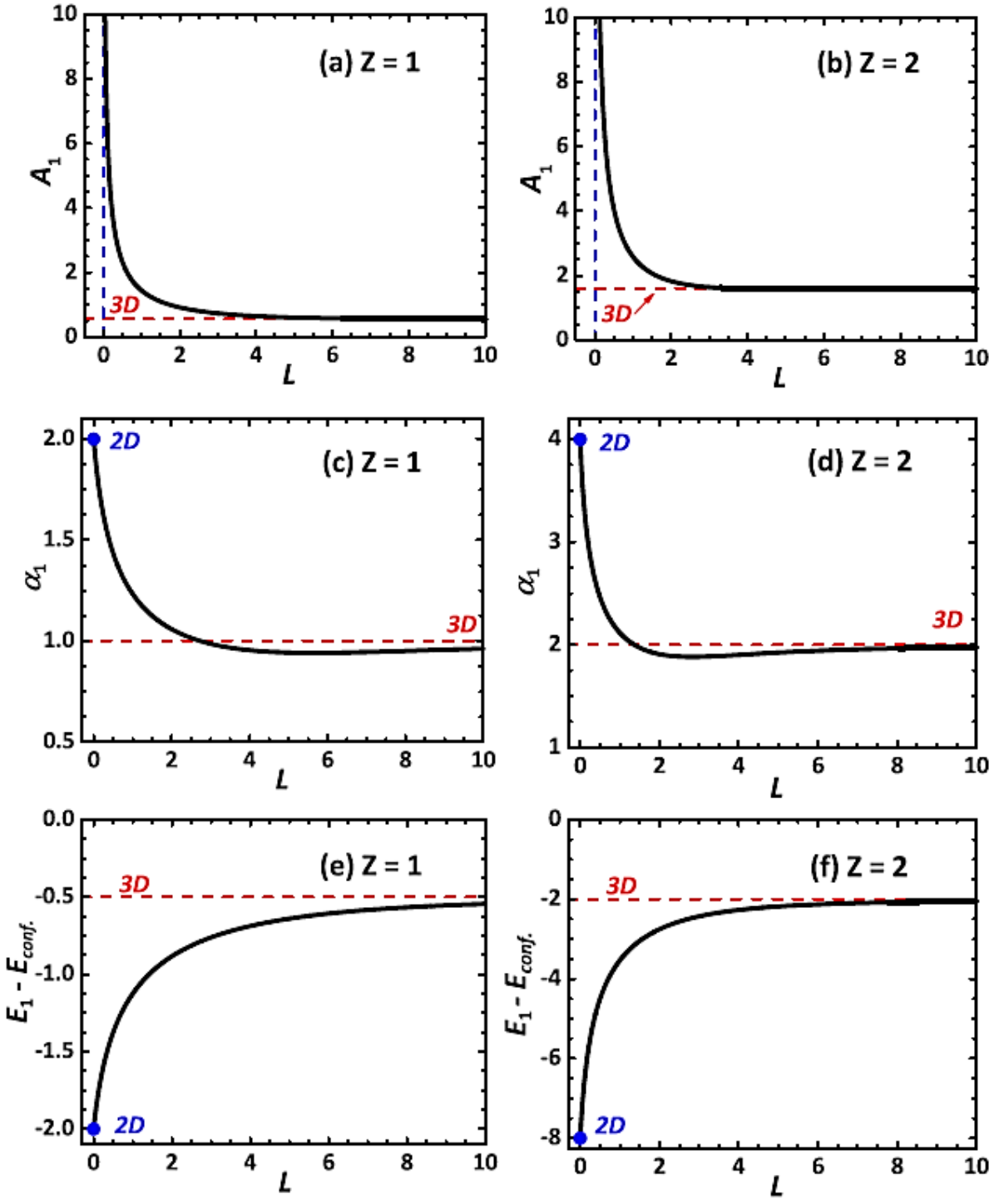

Figure B1. *Parameters A_1 and α_1 of the ϕ_1 wavefunction, and its energy E_1, as a function of the thickness L of the QW (thick continuous curves); the red thin dashed lines correspond to the 3D case. (a), (b): A_1 vs L for $Z = 1$, $Z = 2$. (c), (d): α_1 vs L for $Z = 1$, $Z = 2$. (e), (f): $E_1 - E_{conf.}$ vs L for $Z = 1$, $Z = 2$, where $E_{conf.} = \pi^2/2L^2$.*

3. 2*s* state

The orthogonality condition between the $\phi_1(\rho,z)$ and $\phi_2(\rho,z)$ wavefunctions:

$\int_{|z|<L/2} 2\pi\ \rho d\rho dz \Phi_1\Phi_2 = 0$, implies the following relationship between α_1, α_2 and α_3:

$$\alpha_3 \ = \ \beta\ \frac{N(\beta L)}{N(\beta L)+M(\beta L)}, \tag{B. 7a}$$

with $\beta = \frac{\alpha_1+\alpha_2}{2}$ and

$$M(X) = \frac{1}{2} - \frac{3\pi^2/2}{X^2+\pi^2} + \frac{9\pi^4/4}{[X^2+\pi^2]^2} - \frac{\pi^6}{[X^2+\pi^2]^3} - \frac{\pi^2}{4}\left(\frac{1}{2} + \frac{3X+6-\pi^2/2}{X^2+\pi^2} - \pi^2\frac{2X+9}{[X^2+\pi^2]^2} + \frac{4\pi^4}{[X^2+\pi^2]^3}\right)e^{-X}. \tag{B. 7b}$$

The relationships between α_1, α_2 and α_3 in $3D$ and in $2D$ can be retrieved as limiting cases of the above expressions: $\alpha_3 \to (\alpha_1+\alpha_2)/3$ when $L \to \infty$ and $\alpha_3 \to (\alpha_1+\alpha_2)/2$ when $L \to 0$.

The normalization condition of the $\phi_2(\rho,z)$ wavefunction gives

$$A_2^2 \ = \ \frac{\alpha_2^3}{\pi}\left\{N(\alpha_2 L)\left[1 - 2\ \frac{\alpha_3}{\alpha_2} + \frac{3}{2}\frac{\alpha_3^2}{\alpha_2^2}\right] + M(\alpha_2 L)\left[-2\ \frac{\alpha_3}{\alpha_2} + \frac{3}{2}\frac{\alpha_3^2}{\alpha_2^2}\right] + \frac{1}{8}Q(\alpha_2 L)\frac{\alpha_3^2}{\alpha_2^2}\right\}^{-1}, \tag{B. 8a}$$

with $Q(X) \ = \ 3 + 3X^4\frac{X^4-6\pi^2X^2+\pi^4}{[X^2+\pi^2]^4}$

$$-\frac{\pi^2}{2}\left(\frac{X^3}{X^2+\pi^2} + 3X^2\frac{3X^2+\pi^2}{[X^2+\pi^2]^2} + 6X\frac{6X^4+3\pi^2X^2+\pi^4}{[X^2+\pi^2]^3} + 6\frac{10X^6+5\pi^2X^4+4\pi^4X^2+\pi^6}{[X^2+\pi^2]^4}\right)e^{-X}. \tag{B. 8b}$$

The energy E_2 is obtained as the minimum of the mean energy $\tilde{E}_2 = \langle\phi_2|H|\phi_2\rangle$, which only depends on α_2 (α_1 is known, α_3 is a function of α_1 and α_2). $\tilde{E}_2$ is the sum of a kinetic term:

$$\left\langle\phi_2\left|-\frac{\Delta}{2}\right|\phi_2\right\rangle \ = \ \frac{1}{4}\left(\frac{\pi A_2^2}{\alpha_2^3}\right)\left\{\frac{\pi^2}{L^2}\left[Q_1(\alpha_2 L) - \frac{\alpha_3}{\alpha_2}Q_2(\alpha_2 L) + \frac{\alpha_3^2}{4\alpha_2^2}Q_3(\alpha_2 L)\right] + 2\alpha_2^2 C(\alpha_2 L) + \alpha_3^2\left[\ N(\alpha_2 L) + 2M(\alpha_2 L)\ \right] + 2\alpha_2\alpha_3[C(\alpha_2 L) - 2N(\alpha_2 L)]\right\}, \tag{B. 9a}$$

with

$$Q_1(X) \ = \ 1 - \left(1 + \frac{X}{2}\right)e^{-X} \tag{B. 9b}$$

$$Q_2(X) \ = \ 3 - \left(3 + 2X + \frac{1}{2}X^2\right)e^{-X} \tag{B. 9c}$$

$$Q_3(X) \ = \ 12 - \left(12 + 9X + 3X^2 + \frac{1}{2}X^3\right)e^{-X}, \tag{B. 9d}$$

and a potential term due to the Coulomb interaction:

$$\left\langle \phi_2 \left| -\frac{Z}{r} \right| \phi_2 \right\rangle = -Z\,\frac{\pi A_2^2}{\alpha_2^2}\left\{ C(\alpha_2 L) + N(\alpha_2 L)\left[-2\frac{\alpha_3}{\alpha_2}+\frac{\alpha_3^2}{\alpha_2^2}\right] + M(\alpha_2 L)\frac{\alpha_3^2}{\alpha_2^2}\right\}. \qquad \text{(B. 10)}$$

Finding the parameter α_2 [and consequently α_3, with Eq. (B.7a)] which minimizes $\tilde{E}_2$ (at given L) requires a long numerical procedure, which is in contrast with the much easier work needed for the minimization of $\tilde{E}_1$. Figure B2 shows $\tilde{E}_2$ vs α_2 for $L = 1.5$ and Z = 2; the minimum parameters indicated in the figure give one point in Figs. B3 (b), (d) and (f). Figure B3 shows A_2, α_2, α_3 and E_2 concerning the ϕ_2 wavefunction, for different values of the thickness L, with $Z = 1$ and $Z = 2$: A_2 and α_2 behave with L just as A_1 and α_1 do; α_3 monotonically decreases with L; however, E_2, considered by reference to the confinement energy $E_{conf.} = \pi^2/2L^2$, goes with L from $-2Z^2/9$ ($2D$ value) to $-Z^2/8$ ($3D$ value) but *non*-monotonically [see Figs B3(e) and (f)].

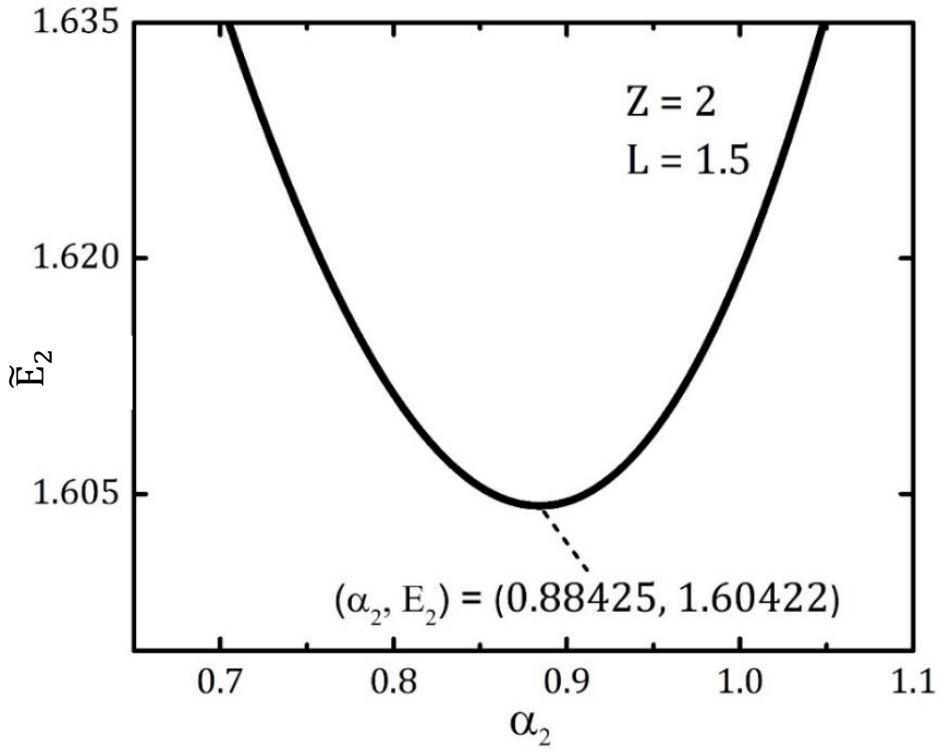

Figure B2. *Mean energy $\tilde{E}_2$ (eqs. B.9 and B.10) as a function of the parameter α_2, for $L = 1.5$ and $Z = 2$. The α_2 step on the horizontal axis is 10^{-5}. The energy E_2 and the parameter α_2 concerning the wave-function ϕ_2 are found as the minimum parameters of the curve.*

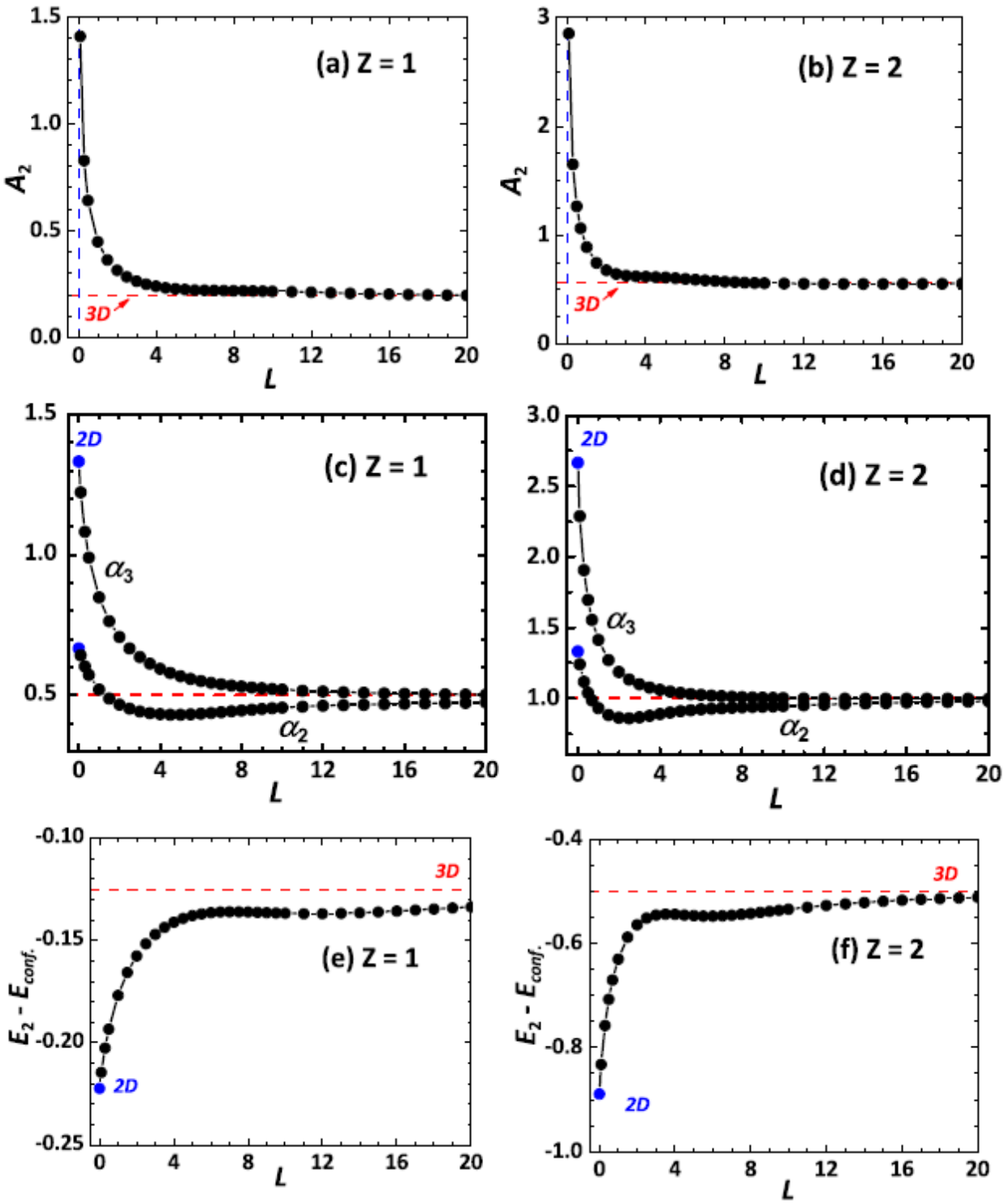

Figure B3. *Parameters A_2, α_2 and α_3 of the ϕ_2 wavefunction, and its energy E_2, as a function of the thickness L of the QW (circular dots; continuous curves: guides for the eyes); the red thin dashed lines correspond to the 3D case. (a), (b): A_2 vs L for $Z = 1$, $Z = 2$. (c), (d): α_2 and α_3 vs L for $Z = 1$, $Z = 2$. (e), (f): $E_2 - E_{conf.}$ vs L for $Z = 1$, $Z = 2$ ($E_{conf.} = \pi^2/2L^2$).*

Appendix C

Exchange energy of a "helium atom" centred in an infinite quantum well

1. Exact results in $3D$

The non-relativistic energies of the (singlet) $(1s)^2$ ground state and of the first-excited triplet $1s2s$ state of the helium atom in $3D$ are known with an excellent precision: in Ref. [2] they are calculated with twenty significant digits. We only write here the first of them:

$$E_S^{exact} = -2.9037\,, \quad E_A^{exact} = -2.1752\,, \tag{C. 1a}$$

in units of effective hartree (see eq. (3.2), chapter 3). The subscript S, or A, recalls that the orbital part of the state is symmetric, or antisymmetric, under permutation of both electrons of the atom. The exchange energy $2J_0 = E_A - E_S$ is then exactly, in $3D$:

$$2J_0^{exact} = 0.7285\,. \tag{C. 1b}$$

2. Exact results in $2D$

In $2D$, the non-relativistic energies of the $(1s)^2$ ground state and the first-excited triplet $1s2s$ state of the helium atom are also known with a very good accuracy: in Ref.[3] they are calculated with thirteen significant digits. We write here the first of them:

$$E_S^{exact} = -11.900\,, \quad E_A^{exact} = -8.296\,, \tag{C. 2a}$$

in units of effective hartree. The exchange energy is then exactly, in $2D$:

$$2J_0^{exact} = 3.604\,. \qquad \text{(C. 2b)}$$

3. Calculation of $2J_0$ in an infinite quantum well

The Hamiltonian describing both electrons in a helium atom writes

$$\widehat{H} \;=\; -\frac{\Delta_1}{2} - \frac{\Delta_2}{2} - \frac{Z}{r_1} - \frac{Z}{r_2} + \frac{1}{r_{12}}\;, \qquad \text{(C. 3)}$$

where Δ_j is the Laplacian operator acting on electron j ($j = 1$ or 2) and r_j is the distance of electron j to the origin of the coordinates, where the $Z = 2$ nucleus is located; $r_{12} = |\vec{r}_2 - \vec{r}_1|$ is the distance between the electrons.

a. Ground energy

The ground energy E_S of the "helium atom" centred in a QW with infinite barriers is determined here by the variational method. The ground-state wavefunction $\Psi_S(\vec{r}_1, \vec{r}_2)$ of the pair of electrons 1 and 2 is taken as the product of two one-electron $1s$-wavefunctions: $\Psi_S(\vec{r}_1, \vec{r}_2) = \phi_1(\vec{r}_1)\phi_1(\vec{r}_2)$; the mean energy $\tilde{E}_S = \langle\Psi_S|\widehat{H}|\Psi_S\rangle$ is studied as a function of the parameter α_1, which now can vary (see section 1 of Appendix B for the definitions of ϕ_1 and α_1), and its minimum is taken for the value of E_S. $\tilde{E}_S$ is the sum of a kinetic term:

$$\left\langle\Psi_S\right|-\frac{\Delta_1}{2}-\frac{\Delta_2}{2}\left|\Psi_S\right\rangle \;=\; \alpha_1^2 \;+\; \frac{\pi^2}{L^2}\;, \qquad \text{(C. 4a)}$$

a potential term due to the Coulomb interaction of the electrons with the $Z = 2$ nucleus:

$$\left\langle\Psi_S\right|-\frac{2}{r_1}-\frac{2}{r_2}\left|\Psi_S\right\rangle \;=\; -\,4\,\alpha_1\,\frac{C(\alpha_1 L)}{N(\alpha_1 L)} \qquad \text{(C. 4b)}$$

[$N(X)$ and $C(X)$: see Appendix B], and a Coulomb electron-electron term:

$$\left\langle\Psi_S\right|\frac{1}{r_{12}}\left|\Psi_S\right\rangle \;=\; 32\pi\int_0^\infty\int_0^\infty \frac{\rho_q\,d\rho_q\,dz_q}{\rho_q^{\,2}+z_q^{\,2}}\left[\int_0^{\frac{L}{2}} dz\cos(z_q z)\int_0^\infty d\rho\;\rho\,J_0(\rho_q\rho)\;\phi_1(\rho,z)^2\right]^2, \qquad \text{(C. 4c)}$$

expressed using the fact that $1/r$ is the inverse Fourier transform of $4\pi/q^2$ [$J_0(x)$ is the Bessel function of first kind and of zeroth order]. This integral is calculated numerically. Figure C1 shows an example of calculation of E_S, for a QW of thickness L = 1.5. The mean energy $\tilde{E}_S = \langle\Psi_S|\widehat{H}|\Psi_S\rangle$ is plotted as a function of the parameter α_1. For this particular value of L, the ground energy is found to be $E_S = min\;\tilde{E}_S \approx -0.198$, corresponding to the value $\alpha_1^{min} \approx 1.701$. As expected, α_1^{min} is slightly smaller than the $\alpha_1 \approx 2.0$ parameter of

the ϕ_1 wavefunction for a single electron (see Fig. B1(d)), as a result of the screening of the +2e nucleus charge by the other electron.

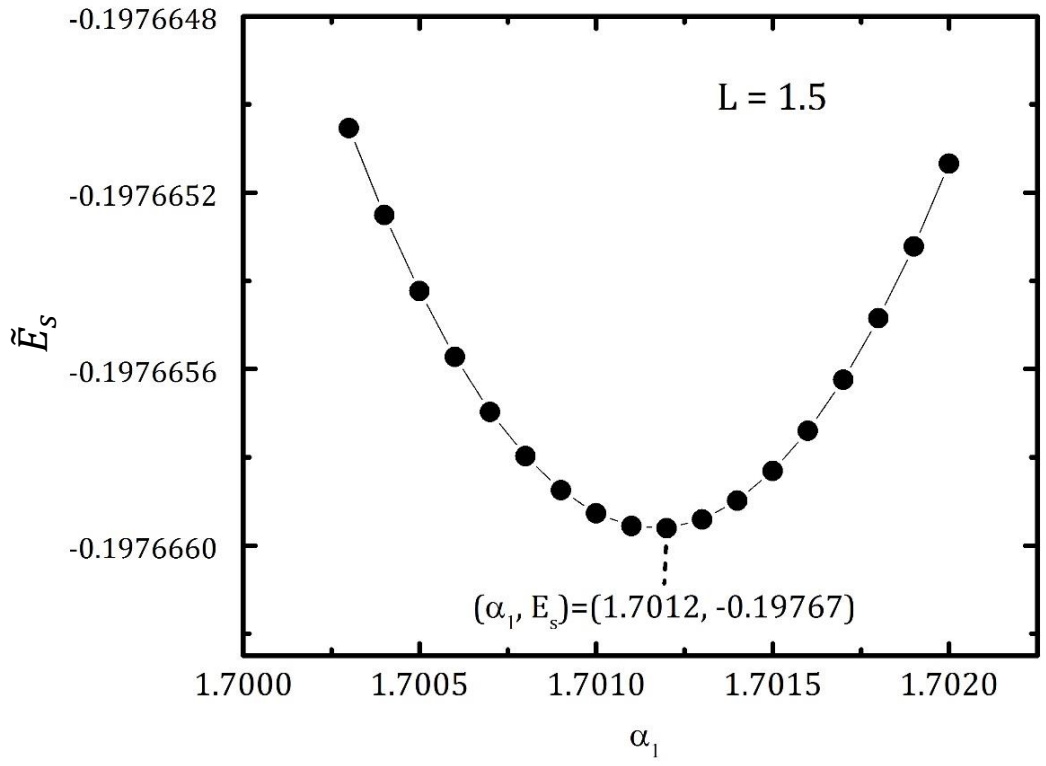

***Figure C1**: $\tilde{E}_S$ vs α_1 as a function of the parameter α_1 for $L = 1.5$ (dots: calculated points). The energy E_S and the parameter α_1 are found as the minimum of the curve. This procedure has been done for each E_S value plotted in Fig. C2.*

b. First-excited state

The first-excited energy E_A of the "helium atom" centred in a QW with infinite barriers is determined perturbatively here: the electron-electron interaction $1/r_{12}$ is treated as a small correction to the state $\Psi_A(\vec{r}_1,\vec{r}_2) = [\phi_1(\vec{r}_1)\phi_2(\vec{r}_2) - \phi_2(\vec{r}_1)\phi_1(\vec{r}_2)]/\sqrt{2}$ of energy $E_1 + E_2$ (ϕ_1, ϕ_2, E_1 and E_2 are given in Appendix B). The energy E_A is of the form $E_A = E_1 + E_2 + \Delta E$, the corrective term being $\Delta E = \langle\Psi_A|1/r_{12}|\Psi_A\rangle$; ΔE is the sum of a direct term:

$$\int\int d^3r_1\, d^3r_2\, \frac{\phi_1(\vec{r}_1)^2\phi_2(\vec{r}_2)^2}{r_{12}}$$
$$= 32\pi \int_0^\infty \int_0^\infty \frac{\rho_q d\rho_q dz_q}{\rho_q^2 + z_q^2} \left[\int_0^{\frac{L}{2}} dz \cos(z_q z) \int_0^\infty d\rho\, \rho\, J_0(\rho_q\rho)\, \phi_1(\vec{r})^2\right] \times \ldots$$
$$\ldots \left[\int_0^{\frac{L}{2}} dz \cos(z_q z) \int_0^\infty d\rho\, \rho\, J_0(\rho_q\rho)\, \phi_2(\vec{r})^2\right], \quad \text{(C. 5a)}$$

and an exchange term:

$$\int\int d^3r_1\, d^3r_2\, \frac{\phi_1(\vec{r}_1)\phi_2(\vec{r}_2)\phi_2(\vec{r}_1)\phi_1(\vec{r}_2)}{r_{12}}$$
$$= 32\pi \int_0^\infty \int_0^\infty \frac{\rho_q d\rho_q dz_q}{\rho_q^2 + z_q^2} \left[\int_0^{\frac{L}{2}} dz \cos(z_q z) \int_0^\infty d\rho\, \rho\, J_0(\rho_q\rho)\, \phi_1(\vec{r})\, \phi_2(\vec{r})\right]^2. \quad \text{(C. 5b)}$$

In $3D$ and in $2D$, calculating E_S by the variational method and E_A perturbatively gives satisfactory values (for our purpose) of the exchange energy $2J_0 = E_A - E_S$: we so obtain $2J_0 = -2.124 + 2.848 = 0.724$ in $3D$, and $-7.948 + 11.635 = 3.687$ in $2D$, which are 0.6 % smaller, and 2 % larger, than the exact values, respectively. We are then confident that our calculated exchange energies $2J_0$ of a "helium atom" centred in infinite QWs of different thicknesses, possess an uncertainty of the 1-% order.

Figure C2 shows our calculated values of the ground energy E_S and first-excited energy E_A, as a function of the thickness L of the QW; the exact values in $2D$ ($L \to 0$) and in $3D$ ($L \to \infty$) are also indicated. E_S and E_A monotonically increase with the thickness L, and their difference, which is $2J_0$, monotonically decreases (see Fig. 3.3 of chapter 3).

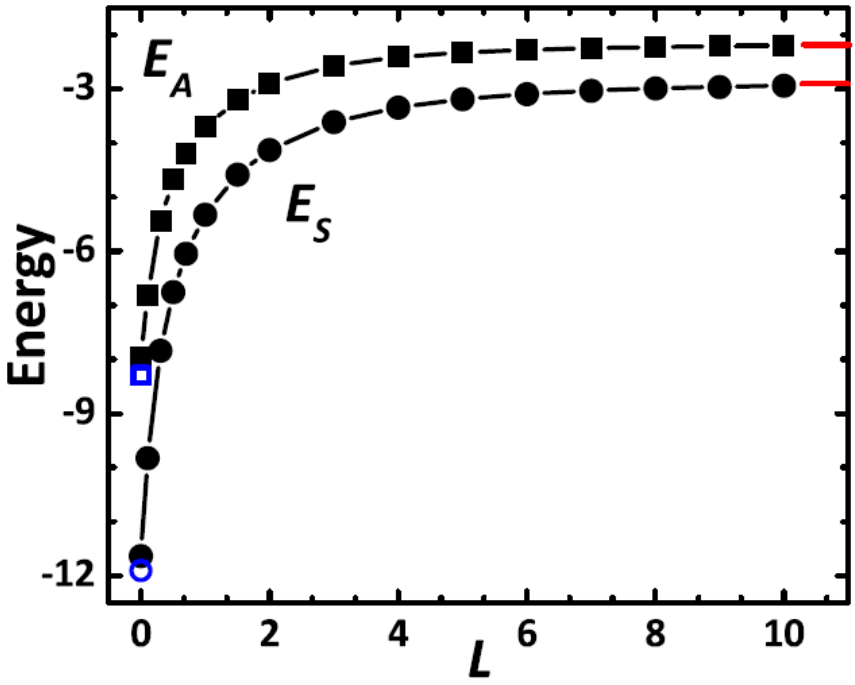

Figure C2. *Ground energy E_S (full disks) and first-excited energy E_A (full squares) of a "helium atom", as a function of the thickness L of the infinite QW; the continuous curves are guides for the eyes. The empty circle and empty square, at $L = 0$, are the exact values in $2D$. The exact values in $3D$ are indicated by two horizontal red segments, on the right of the graph.*

Appendix D

New interpolated formulas for the 3D and 2D exchange energies

Section 3.4 of chapter 3 described the procedure of Ref. [4] to build an interpolated expression of the exchange energy $2J(R)$ in $3D$ and $2D$. In Eq. (3.27), in which A is the only remaining free parameter, it is possible, alternatively, to impose that, for $R \gg 1$, the interpolated $2J(R)$ be in coincidence with the standard asymptotic form $2J(R \gg 1) = CR^{\beta} e^{-\omega R}$. We then obtain the following expression for A:

$$A = (C/2J_0)^{1/\beta}/\mathrm{e}\,. \qquad \text{(D. 1)}$$

So we can propose new interpolated formulas for the exchange energy $2J(R)$ in $3D$ and $2D$, using values of $2J_0$ which are, nowadays, known with very good accuracy (see Appendix C, eqs. (C.1 b), (C.2 b)):

$$2J_{3D}(R) = 0.729\,(1 + 0.259R^2)^{\frac{5}{4}} \times \cdots \exp[-0.003R - 1.271R \arctan(0.509R)]; \qquad \text{(D. 2a)}$$

$$2J_{2D}(R) = 3.604\,(1 + 1.549R^2)^{\frac{7}{8}} \times \cdots \exp[-0.579R - 2.178R \arctan(1.245R)]. \qquad \text{(D. 2b)}$$

These expressions give $2J(R)$ values close to the corresponding ones of Ref. [4] for R of the order of unity, and are more satisfactory, by construction, for large values of R.

Figure D1 shows the exchange energies $2J_{3D}$ (R) given by Ref. [4] (dashed line) and by Eq. (D.2a) (continuous line); for R of the order of unity, the curves only differ by several percent, this difference approaching 10 % for R ≥ 4 (not shown). Figure D2 illustrates

the 2D case: $2J_{2D}$ (R) given by Ref. [4] is larger than the one by Eq. (D.2b), the difference being 10 % for R = 1 and approaching 14 % when R ≥ 2 (not shown). The Eqs. (D.2) are in agreement with the asymptotic forms (3.22) and (3.23) of chapter 3.

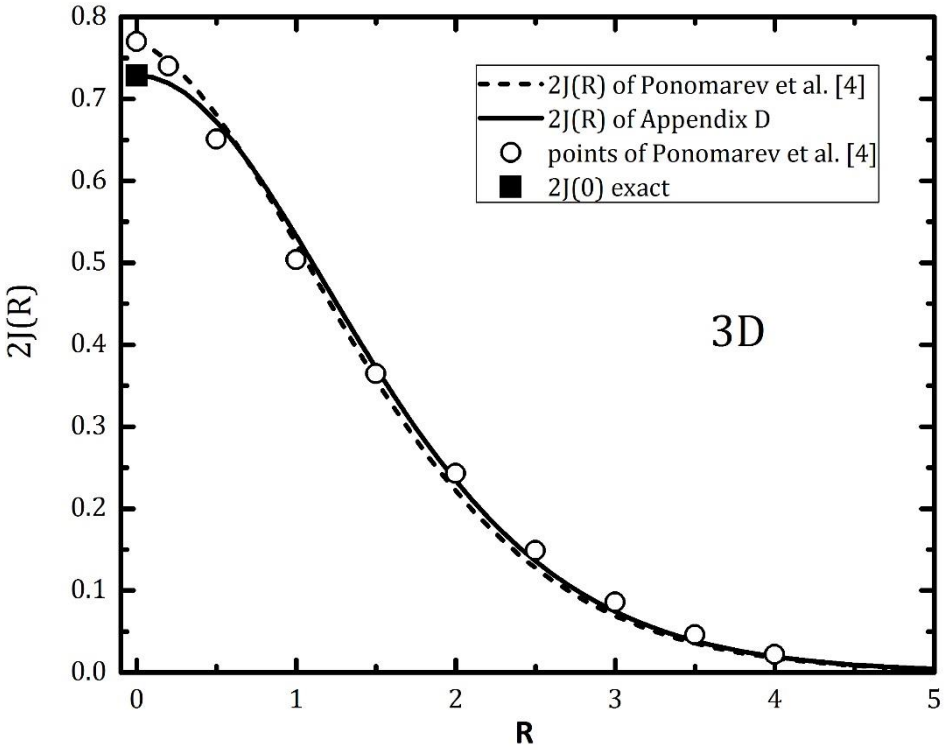

Figure D1. *Dashed line: exchange energy $2J_{3D}(R)$ according to Ref. [4]; continuous line: $2J_{3D}(R)$ according to Eq. (D.2a). Empty disks: numerical values cited in Ref. [4]; black square: exact value of the exchange energy $2J_{3D}(0)$ of the helium atom.*

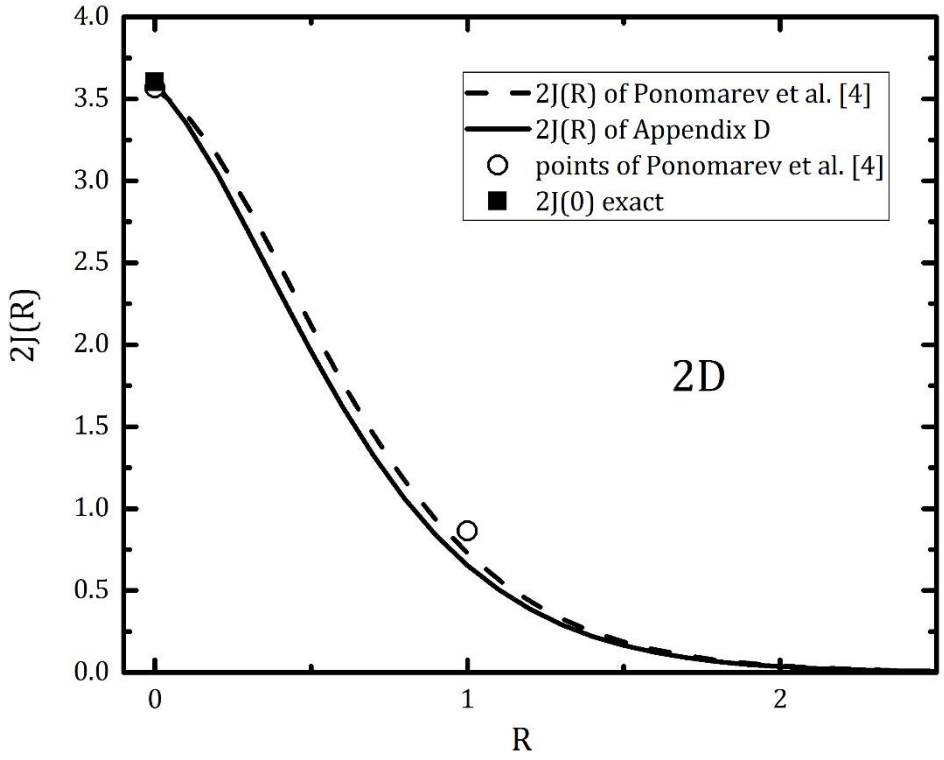

Figure D2. *Dashed line: exchange energy $2J_{2D}(R)$ according to Ref. [4]; continuous line: $2J_{2D}$ (R) according to Eq. (D.2b). Empty disks: numerical values calculated in Ref. [4]; black square: exact value of the exchange energy $2J_{2D}(0)$ of the 2D helium atom.*

References for appendices A-D

[1] X. L. Yang et al., Phys. Rev. A **43**, 1186 (1991).
[2] D. T. Aznabayev, A. K. Bekbaev, I. S. Ishmukhamedov, and V. I. Korobov, Phys. Part. Nucl. Lett. **12**, 689 (2015).
[3] L. Hilico, B. Grémaud, T. Jonckheere, N. Billy, and D. Delande, Phys. Rev. A **66**, 022101 (2002).
[4] I. V. Ponomarev, V. V. Flambaum, and A. L. Efros, Phys. Rev. B **60**, 5485 (1999).